Monitoring Microwave Ablation Treatments for Liver Tumors Using Ultrasound Elastography

By

Wenjun Yang

A dissertation submitted in partial fulfillment of the requirements for the degree of

Doctor of Philosophy

(Medical Physics)

At the

UNIVERSITY OF WISCONSIN-MADISON

2017

Date of final oral examination: 06/02/2017

The dissertation is approved by the Final Oral Committee:

Tomy Varghese, Professor, Medical Physics

Timothy Hall, Professor, Medical Physics

Christopher Brace, Associate Professor, Radiology & BME

Bryan Bednarz, Associate Professor, Medical Physics

Timothy Ziemlewicz, Assistant Professor, Radiolog

Abstract

Monitoring Microwave Ablation Treatments for Liver Tumors Using Ultrasound Elastography

Wenjun Yang

Under the supervision of Professor Tomy Varghese

At the University of Wisconsin-Madison

Liver cancer is the sixth most common and the third leading cause of cancer related deaths world-wide. New cases and mortality in the U.S. have doubled during the past two decades, increasing at a rate of 3.4% per year from 2007 to 2011. Existing treatment methods for liver cancer include partial hepatectomy, embolization with chemotherapy, liver transplant, and percutaneous ablation. Percutaneous ablation is increasingly being adopted as an effective treatment method for liver cancer by thermal necrosis of cancerous tissue, with the advantage of promising treatment outcomes, and minimally invasive procedures.

Previously percutaneous ablation was performed using radiofrequency ablation (RFA), which uses a local circuit loop to generate a thermal dose. To improve the heating rate and volume treated with RFA, microwave ablation (MWA) was introduced which heated local tissue by agitating water molecules using microwave energy. The key factor to yield a promising treatment outcome with MWA is to effectively monitor the ablation margin of the treated region. The guidance imaging modality for MWA, namely ultrasound B-mode imaging is not sufficient to delineate the ablated region after the MWA procedure.

Thus, computed tomography (CT) is adopted as the current gold standard to determine the ablation margin by comparing the pre- and post- treatment images. However, CT scans prolong the treatment time and expose the patients to ionizing radiation. In this dissertation, an ultrasound elastography technique, which is referred to as electrode displacement elastography (EDE), is applied for monitoring clinical MWA procedures. By comparison with B-mode imaging and commercial acoustic radiation force impulse imaging (ARFI), EDE is potentially an alternative imaging modality to provide effective real-time feedback of the ablated margin, which might improve treatment outcomes with MWA.

In addition, our previously introduced three-dimensional (3D) reconstruction algorithm, Sheaf of Ultrasound Planes Reconstruction (SOUPR) was applied for a phantom study to depict the ablation inclusion as a 3D volume instead of a single 2D ultrasound plane. An image fusion technique is also developed to register EDE and CT to determine the ablation margin on EDE with comparison to the current gold standard.

Acknowledgement

I would like to extend my sincere thanks to my advisor, Dr. Tomy Varghese, for his advice on my professional career and his passion towards our research project. His emphasis on time management enabled me to achieve my academic goals in a timely manner. Furthermore, I would like to thank his trust for giving me the opportunity to continue my research in medical physics, for letting me join his group by the end of my first year of Ph.D. study.

I appreciate the great support from each clinician involved in my clinical research. I want to thank the physicians who conducted the ablation procedures, Dr. Fred Lee, Dr. Louis Hinshaw, Dr. Timothy Ziemlewicz, Dr. Meghan Lubner, and Dr. Shane Wells. Their dedication, commitment, and encouragement were exemplary for my future career in medical physics. I also want to thank Ms. Marci Alexander and Mr. Kelly Wergin for coordinating the schedule and patient consent forms. I also thank Ms. Lisa Sampson for her help on the ablation system. I would also like to thank every sonographer for their steady hands to obtain data for each patient. I would not be able to complete my study without their great help.

I also want to thank my other committee members, Dr. Timothy Hall, Dr. Chris Brace, Dr. Bryan Bednarz, Dr. Timothy Ziemlewicz, and Dr. James Zagzebski, for their support on the compression apparatus, ablation system, image fusion techniques, and direction on my clinical study. Their critical comments, insightful suggestions helped a lot since the very beginning of my projects. My projects will be extended in the future thanks to their great input.

I also want to thank the previous and current members in my group, Dr. Nicholas Rubert, Dr. Atul Ingle, Dr. Chi Ma, Dr. Xiao Wang, Dr. Eenas Omari, Dr. Kayvan Samimi, Nirvedh Meshram, Catherine Steffel, Rashid Mukaddim, Robert Pohlman, and Michael Turney. They have contributed a lot to my research and working with them will be a highlight in my memory.

I appreciate the help from Mr. Jim White and Mr. Gary Frank on the technical aspects with the ablation system and compression apparatus. Addressing these details was actually the most time-consuming part of my scientific research. Jim's education on the Certus system was crucial for my *ex-vivo* experiments and Gary's help on the metal markers, transducer holders, and the Bose Mechanical Testing system meant a lot for all my projects.

I also want to thank every professor, student and staff in the Medical Physics department. I learned a lot from their lectures, and daily contact. The multi-cultural environment will be beneficial for my whole life, since I can understand myself deeper only by experiencing the variety of cultures from all over the world

I want to thank my parents, Xinchun Yang and Kejing Xu. Their unconditional love and support kept me encouraged and looking forward. My Ph.D. degree is also a gift for them.

I would like to give my special thanks to my wife, Yan Zhang. We have witnessed every step of each other's lives over the past twelve years. Even if I have achieved something, you know it is for you.

Contents

List of Figures

List of Tables

Chapter 1: Introduction

1.1 Motivation

Hepatocellular carcinoma (HCC) is the 6th most common cancer and 3rd leading cause of cancer related mortality worldwide [1]. Surgical resection of liver tissue is the standard procedure for the cure of HCC although there are critical constraints for its wide-spread use. The following criteria have to be met for successful surgical resection: (1) the cancer is limited to a single liver lobe; (2) liver function is well preserved; and (3) the patient neither has abnormal bilirubin nor portal hypertension [1]. However, cirrhosis commonly occurs with HCC, and only up to 5% of cirrhotic patients with HCC fit the constraints described above for liver resection [1]. Therefore, as few as 9% of patients with HCC are suitable candidates for surgical resection [2]. With the development of minimally invasive treatments such as percutaneous radiofrequency ablation (RFA) and microwave ablation (MWA), thermal ablation has been adopted as the primary treatment option for HCC, especially for early stage interventions (tumor sizes < 3 cm) [3, 4]. Existing clinical studies have shown that treatment outcomes with ablation procedures are superior or at least equivalent to surgical resection or ethanol injection for these early stage HCC tumors [1-6].

MWA, introduced as an ablation technique initially in Japan [7], has now been increasingly applied worldwide [2, 5, 6, 8-10]. Instead of generating the thermal dose by incorporating the patient as part of a closed loop circuit as in RFA, MWA emits microwave energy to agitate water molecules causing coagulation necrosis with a local impact. Thus,

MWA delivers consistently higher intra-tumor temperatures, with reduced impact from blood flow in large vessels, enables faster ablation times, and provides an improved convection profile [2, 3, 9]. Multiple probes can be applied simultaneously to create larger tumor ablation volumes [11]. MWA therefore has several advantages over RFA including increased power, increased volume of direct heating, ablation consistency in different tissue types, and no requirement for ground pads [12-14]. With these technological advantages, MWA has been increasingly cited as the more commonly utilized percutaneous ablation method [13, 14]. Some investigators have reported that MWA does not show an obvious improvement over RFA in treatment outcomes [5, 8, 9], however these studies utilized previous generation microwave technology. When evaluating current generation technology, MWA has shown a significantly lower rate of local tumor progression than RFA [15]. The modality limitation might also be compensated by other treatment methods such as trans-arterial chemoembolization (TACE) to limit the blood supply from the hepatic artery to reduce the heat sink effect of large vessels [2, 6]. One recent study has shown that MWA could lead to satisfactory outcome even for tumor sizes greater than 3 cm which was previously considered to be the maximum suitable size for thermal ablation procedures [16].

Ultrasound elastography has been considered as an alternative for ablation monitoring since the stiffness contrast between an ablated region and surrounding tissue is high [17-27], and is not significantly impacted by the presence of gas bubbles [28]. Conventional, quasi-static ultrasound elastography is dependent on either an externally applied compression [29] or internal physiological deformations [19, 30, 31] to produce displacements for estimating local tissue strain. The need for an external compressor would

restrict the use of ultrasound elastography because it is cumbersome and generally cannot produce tissue displacements at sufficient depth. Acoustic radiation force [22, 26, 32-35], could be more suited for this task, but ARFI is limited by the small tissue displacements that can be generated (around 0.01 mm), and a relatively shallow imaging depth of around 8 cm. Beyond this depth the acoustic radiation force generated is too small to deform tissue due to attenuation of the signal [36, 37]. The resulting data are also very sensitive to physiological motion such as cardiac pulsation and respiratory artifacts.

The key factor for successful percutaneous ablation treatment is the presence of an adequate ablation margin around the tumor being treated. Various studies suggest that the margin should be between 0.5 – 1.0 cm extending into the tumor free region [12, 19, 24]. Thus, an effective thermal ablation margin monitoring method is crucial to guarantee a successful clinical outcome. Conventional ultrasound B-mode imaging is usually used to guide the placement of the ablation needle. However, due to the similar echogenicity between the ablated region and surrounding tissue, B-mode imaging is not ideal for monitoring ablation extent [4, 5, 31]. Currently the clinically acceptable method to monitor the ablation margin is computed tomography (CT) with contrast. After the estimated thermal dose is delivered, a CT scan is performed on the ablated region to confirm the ablation volume. A cessation of the ablation procedure would occur since the CT scan is not done in real time and the treatment room has to be cleared to avoid ionizing radiation exposure to physicians and other clinical staff.

We previously introduced a novel quasi-static ultrasound elastography technique, referred to as electrode displacement elastography (EDE) [18, 25, 38], which was designed specifically for percutaneous ablation monitoring [18, 23, 39]. The mechanical stimulus

for EDE is applied by perturbation of the ablation needle controlled by the physician performing the procedure. Due to the significant modulus contrast between the ablated region and the surrounding healthy tissue, there is a “saturated halo” around the ablation zone on the strain image. Previous studies on phantom and *in-vivo* porcine models have shown that the ablation zone on EDE matches ablation pathology well in terms of target area and dimensions [25, 38]. Because of the small range of displacement introduced by the needle (around 1 mm), the ablation procedure would also not be adversely affected. In addition to EDE, an approach that vibrates the ablation needle to generate and image shear waves termed electrode vibration elastography has also been developed in our laboratory [40-43].

In this dissertation, EDE was applied to monitor clinical MWA on patients diagnosed with HCC and liver metastases. Loops of radio frequency (RF) ultrasound data were recorded during the perturbation of the ablation antenna performed by a physician. Strain images were generated by tracking the local displacements computed using a two-dimensional displacement tracking algorithm (reference). Ablation zones obtained were compared on EDE and conventional ultrasound B mode images in terms of ablation region size, area, contrast and contrast to noise ratio (CNR). Ablation sizes were then compared to pre-treatment imaging modality either CT or magnetic resonance imaging (MRI) for comparison of ablation region dimensions.

1.2 Organization of the dissertation

In chapter 2 following this introductory chapter, a more detailed literature review is provided describing liver cancer, available treatment methods, development of

percutaneous treatment technology, ultrasound elastography approaches for monitoring ablations, possible approaches for three-dimensional reconstruction or the ablation volume and methods for image fusion described in the literature.

A pilot study describing the clinical application of EDE for monitoring MWA procedures is discussed in chapter 3. In this study, we evaluated EDE on 44 patients diagnosed with hepatocellular carcinoma that were treated using microwave ablation. The ablated region was identified on EDE images for 40 of the 44 patients. Ablation areas with EDE were 13.38 ± 4.99 cm^2, when compared to 7.61 ± 3.21 cm^2 on B-mode imaging. Contrast and contrast to noise ratio obtained with EDE was 232% and 98%, respectively, significantly higher than values measured from B mode images ($p < 0.001$). This study demonstrates that EDE is feasible in HCC patients and provided improved visualization of the ablation zone when compared to B-mode ultrasound.

In chapter 4, a comparison of EDE with a commercially implemented acoustic radiation force impulse imaging (ARFI) method is performed on patients with both HCC and metastatic tumors. Forty-nine patients recruited to this study were monitored with EDE and ARFI using a Siemens Acuson S2000 system after an MWA procedure. Based on visualization results from two observers, the ablated region on ARFI images was recognizable on twenty patients averaging from the two observers in conjunction with B-mode imaging, while delineable ablation boundaries could be generated on 4 patients averaging from the two observers. With EDE, the ablated region was delineable on forty patients averaging from the two observers, with less imaging depth dependence. Study of tissue mimicking phantoms demonstrated that the ablation region dimensions measured on EDE and ARFI images were within 8%, while the image contrast and contrast to noise ratio

with EDE was 2 – 3 times higher than that obtained with ARFI. This study showed that EDE provided improved monitoring results for minimally invasive MWA in clinical procedures for liver cancer and metastases.

A three-dimensional (3D) reconstruction algorithm, which was previously developed in our laboratory and referred to as Sheaf of Ultrasound Planes Reconstruction (SOUPR), was applied on tissue mimicking (TM) phantoms and compared to 3D reconstructions obtained with wobbler transducer in chapter 5. Reconstruction using SOUPR was formulated as an optimization problem with constraints on data consistency with 2D strain images and data smoothness of the volume data. Reconstructed ablation inclusion dimensions, volume, and elastographic signal, and contrast to noise ratios (SNRe and CNRe) were compared with conventional 3D ultrasound strain imaging based on interpolating a series of quasi-parallel 2D strain images with a wobbler transducer. Volume estimates of the phantom inclusion were in a similar range for both acquisition approaches. SNRe and CNRe obtained with SOUPR was significantly higher on the order of 250% and 166% respectively. The mean error of the inclusion dimension reconstructed with a wobbler transducer was on the order of 10.4%, 3.5% and 19.0% along the X, Y and Z axes, respectively, while the error with SOUPR was on the order of 2.6%, 2.8% and 9.6%. A qualitative comparison of SOUPR and wobbler reconstruction was also performed using a thermally ablated region created in *ex-vivo* bovine liver tissue. We have demonstrated using experimental evaluations with a TM phantom that the reconstruction results obtained with SOUPR were superior when compared with a conventional wobbler transducer in terms of inclusion shape preservation and detectability.

In chapter 6, an image fusion technique is explored to register EDE and CT images using the ablation antenna as a landmark. The most challenging aspect for comparison of the ablation margin with EDE and CT images is that the EDE imaging plane is not necessarily coincident with CT series of axial plane acquisitions. For monitoring and guidance purposes, the imaging plane with ultrasound B-mode and EDE are selected to encompass the entire ablation antenna, which are usually between axial and sagittal CT scan planes. However, the CT planes are located as sequential axial planes. Within each plane, the ablation antenna will show a partial intersection with the particular plane. A virtual slicing algorithm was applied on the 3D CT volume, to extract the corresponding CT slice containing the entire needle. Post-ablation EDE and CT images were then registered using the MWA treatment antenna as the land mark.

Chapter 7 concludes with a description of the contributions of this dissertation and discusses the future direction of our research on improving the monitoring ability of EDE for MWA procedures.

1.3 References

1. Lencioni, R. and L. Crocetti, *Radiofrequency ablation of liver cancer.* Tech Vasc Interv Radiol, 2007. **10**(1): p. 38-46.
2. Liang, P. and Y. Wang, *Microwave ablation of hepatocellular carcinoma.* Oncology, 2007. **72 Suppl 1**: p. 124-31.
3. Lencioni, R. and L. Crocetti, *Local-regional treatment of hepatocellular carcinoma.* Radiology, 2012. **262**(1): p. 43-58.
4. Shiina, S., et al., *Radiofrequency ablation for hepatocellular carcinoma: 10-year outcome and prognostic factors.* Am J Gastroenterol, 2012. **107**(4): p. 569-77; quiz 578.

5. Lu, M.D., et al., *Percutaneous microwave and radiofrequency ablation for hepatocellular carcinoma: a retrospective comparative study.* J Gastroenterol, 2005. **40**(11): p. 1054-60.

6. Maluccio, M. and A. Covey, *Recent progress in understanding, diagnosing, and treating hepatocellular carcinoma.* CA Cancer J Clin, 2012. **62**(6): p. 394-9.

7. Murakami, R., et al., *Treatment of hepatocellular carcinoma: value of percutaneous microwave coagulation.* AJR Am J Roentgenol, 1995. **164**(5): p. 1159-64.

8. Shibata, T., et al., *Small hepatocellular carcinoma: comparison of radio-frequency ablation and percutaneous microwave coagulation therapy.* Radiology, 2002. **223**(2): p. 331-7.

9. Qian, G.J., et al., *Efficacy of microwave versus radiofrequency ablation for treatment of small hepatocellular carcinoma: experimental and clinical studies.* Eur Radiol, 2012. **22**(9): p. 1983-90.

10. Swan, R.Z., et al., *Operative microwave ablation for hepatocellular carcinoma: complications, recurrence, and long-term outcomes.* J Gastrointest Surg, 2013. **17**(4): p. 719-29.

11. Harari, C.M., et al., *Microwave Ablation: Comparison of Simultaneous and Sequential Activation of Multiple Antennas in Liver Model Systems.* Radiology, 2016. **278**(1): p. 95-103.

12. Lubner, M.G., et al., *Microwave ablation of hepatic malignancy.* Semin Intervent Radiol, 2013. **30**(1): p. 56-66.

13. Wells, S.A., et al., *Liver Ablation: Best Practice.* Radiol Clin North Am, 2015. **53**(5): p. 933-71.

14. Ziemlewicz, T.J., et al., *Hepatic Tumor Ablation.* Surg Clin North Am, 2016. **96**(2): p. 315-39.

15. Potretzke, T.A., et al., *Microwave versus radiofrequency ablation treatment for hepatocellular carcinoma: A comparison of efficacy at a single center.* Journal of Vascular and Interventional Radiology, 2016. **27**(5): p. 631-638.

16. Ziemlewicz, T.J., et al., *Percutaneous microwave ablation of hepatocellular carcinoma with a gas-cooled system: initial clinical results with 107 tumors.* J Vasc Interv Radiol, 2015. **26**(1): p. 62-8.

17. Righetti, R., et al., *Elastographic characterization of HIFU-induced lesions in canine livers.* Ultrasound Med Biol, 1999. **25**(7): p. 1099-113.

18. Varghese, T., J.A. Zagzebski, and F.T. Lee, Jr., *Elastographic imaging of thermal lesions in the liver in vivo following radiofrequency ablation: preliminary results.* Ultrasound Med Biol, 2002. **28**(11-12): p. 1467-73.

19. Varghese, T., et al., *Ultrasonic imaging of myocardial strain using cardiac elastography.* Ultrason Imaging, 2003. **25**(1): p. 1-16.

20. Bharat, S., et al., *Monitoring stiffness changes in lesions after radiofrequency ablation at different temperatures and durations of ablation.* Ultrasound Med Biol, 2005. **31**(3): p. 415-22.

21. Bharat, S., et al., *Three-dimensional electrode displacement elastography using the Siemens C7F2 fourSight four-dimensional ultrasound transducer.* Ultrasound Med Biol, 2008. **34**(8): p. 1307-16.

22. Fahey, B.J., et al., *In vivo guidance and assessment of liver radio-frequency ablation with acoustic radiation force elastography.* Ultrasound Med Biol, 2008. **34**(10): p. 1590-603.

23. Kolokythas, O., et al., *Ultrasound-based elastography: a novel approach to assess radio frequency ablation of liver masses performed with expandable ablation probes: a feasibility study.* J Ultrasound Med, 2008. **27**(6): p. 935-46.

24. Zhang, M., et al., *Real-time sonoelastography of hepatic thermal lesions in a swine model.* Med Phys, 2008. **35**(9): p. 4132-41.

25. Rubert, N., et al., *Electrode displacement strain imaging of thermally-ablated liver tissue in an in vivo animal model.* Med Phys, 2010. **37**(3): p. 1075-82.

26. Mariani, A., et al., *Real time shear waves elastography monitoring of thermal ablation: in vivo evaluation in pig livers.* J Surg Res, 2014. **188**(1): p. 37-43.

27. Zhou, Z., et al., *A survey of ultrasound elastography approaches to percutaneous ablation monitoring.* Proc Inst Mech Eng H, 2014. **228**(10): p. 1069-82.

28. Varghese, T., et al., *Impact of gas bubbles generated during interstitial ablation on elastographic depiction of in vitro thermal lesions.* J Ultrasound Med, 2004. **23**(4): p. 535-44; quiz 545-6.

29. Ophir, J., et al., *Elastography: a quantitative method for imaging the elasticity of biological tissues.* Ultrasonic imaging, 1991. **13**(2): p. 111-134.

30. Varghese, T. and H. Shi, *Elastographic imaging of thermal lesions in liver in-vivo using diaphragmatic stimuli.* Ultrason Imaging, 2004. **26**(1): p. 18-28.

31. Shi, H. and T. Varghese, *Two-dimensional multi-level strain estimation for discontinuous tissue.* Physics in medicine and biology, 2007. **52**(2): p. 389.

32. Sarvazyan, A.P., et al., *Shear wave elasticity imaging: a new ultrasonic technology of medical diagnostics.* Ultrasound Med Biol, 1998. **24**(9): p. 1419-35.

33. Nightingale, K.R., et al., *On the feasibility of remote palpation using acoustic radiation force.* J Acoust Soc Am, 2001. **110**(1): p. 625-34.

34. Hoyt, K., B. Castaneda, and K.J. Parker, *Two-dimensional sonoelastographic shear velocity imaging.* Ultrasound Med Biol, 2008. **34**(2): p. 276-88.

35. Bing, K.F., et al., *Combined ultrasonic thermal ablation with interleaved ARFI image monitoring using a single diagnostic curvilinear array: a feasibility study.* Ultrason Imaging, 2011. **33**(4): p. 217-32.

36. Zhao, H., et al., *Bias observed in time-of-flight shear wave speed measurements using radiation force of a focused ultrasound beam.* Ultrasound in medicine & biology, 2011. **37**(11): p. 1884-1892.

37. Deng, Y., et al., *Analyzing the Impact of Increasing Mechanical Index and Energy Deposition on Shear Wave Speed Reconstruction in Human Liver.* Ultrasound in medicine & biology, 2015.

38. Bharat, S., et al., *Radio-frequency ablation electrode displacement elastography: a phantom study.* Med Phys, 2008. **35**(6): p. 2432-42.

39. Varghese, T., *Quasi-Static Ultrasound Elastography.* Ultrasound Clin, 2009. **4**(3): p. 323-338.

40. Bharat, S. and T. Varghese, *Radiofrequency electrode vibration-induced shear wave imaging for tissue modulus estimation: A simulation study.* The Journal of the Acoustical Society of America, 2010. **128**(4): p. 1582-1585.

41. DeWall, R.J. and T. Varghese, *Improving thermal ablation delineation with electrode vibration elastography using a bidirectional wave propagation assumption.* IEEE Trans Ultrason Ferroelectr Freq Control, 2012. **59**(1): p. 168-73.

42. Dewall, R.J., T. Varghese, and C.L. Brace, *Visualizing ex vivo radiofrequency and microwave ablation zones using electrode vibration elastography.* Med Phys, 2012. **39**(11): p. 6692-700.

43. Ingle, A. and T. Varghese, *Three-dimensional sheaf of ultrasound planes reconstruction (SOUPR) of ablated volumes.* IEEE Trans Med Imaging, 2014. **33**(8): p. 1677-88.

Chapter 2: Literature Review

2.1 Human physiology of liver

The liver of humans is a vital organ with a dark red-brown appearance. Four lobes of different size and shape comprise the entire liver, with a normal weight of 1.44 – 1.66 Kg [1], and a width of around 15 cm [1] in humans. Liver is both the heaviest internal organ and the largest gland, locating in the right upper quadrant of abdominal cavity, resting below the diaphragm, to the right of the stomach and above the gallbladder [2]. The physiological functions of liver include detoxification of various metabolites, protein synthesis, production of bile for digestion, metabolism, regulation of glycogen storage, decomposition of red blood cells and hormone production [3].

The functional units of liver are liver cells, or hepatocytes. Carbohydrate, protein amino acid, and lipid metabolism mainly occurs in the liver [3]. A unique physiological characteristic of the liver is the dual blood supply system, from hepatic portal vein and hepatic arteries. Approximately 75% of the liver's blood supply is delivered by the hepatic portal vein, carrying venous blood drained from the spleen, gastrointestinal tract, and its associated organs. The hepatic arteries supply arterial blood to the liver, accounting for the remaining quarter of its blood flow. Oxygenated blood is provided for the liver's oxygen demand by the hepatic portal vein, and the hepatic arteries, with approximately 50% from each source [4].

2.2 Liver cancer

Primary and metastatic tumors comprise the two types of liver neoplasms. Primary liver cancer, which is also named as primary hepatic cancer, is the tumor that originates from liver cells or other structures within the liver. Approximately 75% of the primary liver cancers are hepatocellular carcinoma (HCC) [5], which originates from liver cells, or hepatocytes [3]. Hepatoblastoma [6] is another primary liver cancer formed by liver cells, specifically, immature liver cells. It is a rare cancer that occurs mainly in children. Cancer originating from the bile duct, which is named as cholangiocarcinoma, accounts for around 6% of primary liver cancers [6]. The remaining approximately 20% of primary liver cancer includes mesenchyme [6], which is formed by a type of connective tissue, leiomyosarcoma and rhabdomyosarcoma [6], which are formed by muscle tissue in liver, and other less common liver cancers include carcinosarcomas, teratomas, yolk sac tumors, carcinoid tumors and lymphomas [6].

Metastatic tumors in liver are secondary tumors spread from the primary tumors in other organs to the liver, and these are more prevalent than primary liver tumors [7]. The most frequent original site of liver metastasis is the gastrointestinal tract, including pancreatic cancer, stomach cancer, colon cancer and carcinoid tumors. Breast cancer, ovarian cancer, lung cancer, renal cancer, and prostate cancer also contribute to liver metastasis [7].

Viral infection including hepatitis C virus (HCV) and hepatitis B virus (HBV) accounts for 80% of HCC worldwide [8-10]. Massive inflammation, fibrosis and eventual cirrhosis that occur within the liver by viral infections are the main cause of HCC. Aflatoxin

exposure also contributes to the development of HCC. Aflatoxins are produced by the fungi Aspergillus flavus. Food contamination with aflatoxins is the major infection method that increases the chance for HCC development. Mutation of an anti-cancer gene, P53 [11, 12], caused by aflatoxins, is the mechanism for developing HCC. Over three times higher risk for liver cancer is observed for a patient who have concurrent HBV infection and aflatoxin exposure than for the patient with HBV infection and without aflatoxin exposure [12]. Other contributing factors to liver cancer include alcohol-induced cirrhosis [13], obesity [12], diabetes [12], smoking [12], etc.

Primary liver cancer is the sixth most common and the second leading cause of cancer related deaths world-wide [7]. New cases and deaths in the U.S. have doubled during the past two decades, increasing 3.4% per year on an average from 2007 to 2011. About 33,190 new liver cancer cases were diagnosed in 2014 in the U.S.A, with the 5 year survival rate (2004-2010) of 16.6% [14]. More than 80% of total primary liver cancer cases occur in sub-Saharan Africa and in East-Asia due to hepatitis B viral infections [15, 16]. The prevalence of HCC is approximately 75% in males and 25% in females [14].

2.3 Treatment for liver cancer

Surgical resection of liver tissue is the standard procedure for the cure of HCC although there are critical constraints on its wide-spread use. The following have to be met for successful surgical resection; (1) the cancer must be limited to a single liver lobe, (2) liver function must be well preserved and (3) the patient neither has abnormal bilirubin nor portal hypertension [17]. However, cirrhosis commonly occurs with HCC [18-23] and only up to 5% of cirrhotic patients with HCC fit the constraints described above for liver

resection [17]. The total number of patients with HCC who are suitable candidates for resection are as low as 9% [24]. Blood vessel embolization is a chemotherapy procedure used to limit the blood supply to the tumor. Trans catheter arterial chemoembolization (TACE) and ethanol injection are the most commonly used methods, which are usually combined with other treatment methods. Liver transplant is considered for patients with multiple tumors or serious liver dysfunction. However, liver transplant is limited by the Milan criteria [25], and by the limited availability.

Radiation therapy for liver cancer is limited. Firstly, the tolerance of liver to radiation is relatively low, and the induced liver diseases include sinusoids and necrosis in liver [26]. Secondly, the image contrast with liver cancers is relatively low in CT images. Contrast agents are usually used for image contrast enhancement based on the unique two blood supply system of the liver. The normal liver cells receive blood supply mainly from portal vein, while the tumor cells receive blood supply from arterial system. Contrast is injected at a specific point of the cardiac cycle such that the contrast agent is only visible in the arterial blood supplied to the tumor [27]. However, the contrast agent can be only injected at specific times and active breath holds [28] have to be taken. Thus, target motion control for liver cancer is limited [29, 30]. For other types of cancer such as lung cancer, the image contrast is much improved due to the huge density difference between air and tissue, four-dimensional CT imaging has been applied to control the target motion for radiation therapy [28].

With the development of minimally invasive treatments such as percutaneous radiofrequency ablation (RFA) and microwave ablation (MWA) technologies, thermal ablation has been adopted as the primary treatment option for HCC especially for very

early (tumor size < 2 cm) and early stage (single tumors with tumor size < 3 cm) [31, 32]. Existing clinical studies have shown that treatment outcomes with ablation procedures are superior or at least equivalent to surgical resection or ethanol injection as the previous standard of care [17, 24, 31-34] for these early stage HCC tumors.

A major limitation with RFA is the variability in thermal dose within the ablation volume and incomplete thermal dose adjacent to large vessels due to the heat sink effect caused by circulating blood [31]. It limits the application of RFA to large tumors and ones near large vessels with a decrease up to 50% in terms of complete tumor necrosis [31]. On the other hand, MWA introduced as an ablation technique initially in Japan [35], has now been increasingly applied worldwide [24, 33, 34, 36-38]. Instead of generating the thermal dose by incorporating the patient as part of a closed loop circuit as in RFA, MWA emits microwave energy to agitate water molecules causing coagulation necrosis with a local impact. Thus, MWA delivers consistently higher intratumoral temperatures, with reduced impact from blood flow in larger vessels, faster ablation times and an improved convection profile [24, 31, 36]. Without the interference from the closed loop circuit, multiple probes can be applied simultaneously to create larger tumor ablation volumes. MWA can be performed with multiple antennas simultaneously to cover larger treated volumes, with additional benefits such as an improved heating rate while avoiding the risk of skin burns caused by the grounding pad used in RFA [24, 36, 39-42]. With these technological advantages, MWA has been increasingly adopted as the most commonly utilized percutaneous ablation method [41, 43] although the comparison between RFA and MWA do not show an obvious improved treatment outcome with MWA [33, 36, 38]. One possible reason is that RFA was compensated by other treatment methods such as TACE to limit

the blood supply from the hepatic artery to reduce the heat sink effect of large vessels [24, 34]. One recent study has shown that MWA could lead to satisfactory outcome even for tumor sizes greater than 3 cm which was considered to be the maximum suitable size for thermal ablation procedures [43].

2.4 Physical model of the elasticity of liver

Both diffuse and focal hepatic disease such as fibrosis or hepatocellular carcinoma (HCC), respectively exhibit increased local tissue stiffness [18-23]. For the diagnosis of liver fibrosis, a liver stiffness threshold below 6 kPa is considered to be normal, while the value between 8 and 12.5 kPa is considered as the threshold for advanced fibrosis (F3) and cirrhosis (F4), respectively [23]. Liver stiffness was reported to be even higher among patients with HCC. In Jung's study [22], the average liver stiffness of 57 patients with HCC was 16.1 kPa which was significantly higher than the threshold of fibrosis. The elasticity of liver tissue increases with an even larger amount after thermal ablation. In a previous study in our group [44], the elasticity and temperature of *ex-vivo* canine liver was found to be non-monotonically positively correlated. An EnduraTEC ELF 3200, a dynamic mechanical testing system was used to measure the elasticity of *ex-vivo* tissue with a loading frequency of 0.1 Hz. The Young's modulus increased from 5.0 kPa to 25.0 kPa when temperature increased from 60° C to 90° C, with a dip in the stiffness value at 80° C. Yeh et al. [45], reported on the Young's modulus of 19 fresh liver samples and 1 hepatic tumor sample obtained following surgery were measured with a stepper motor and electronic balance system. Histologic examination and grade of liver fibrosis was scored for each specimen. Significant correlation between the fibrosis score and the elastic modulus was found, with a quadratic trend. In the DeWall et al. study [46], 16 human

hepatic primary and secondary tumors and their corresponding background tissue obtained following surgical resection was tested using a dynamic compression method. It was found that F4-graded fibrotic liver tissue was three times stiffer than F0-graded liver tissue, while steatotic liver tissue was slightly stiffer than normal tissue in loading frequency ranges over 1-30 Hz. For the HCC cases, the modulus contrast of tumor to background tissue was about 1:1, due to the liver fibrosis present with HCC. Conversely, metastatic tumors were significantly stiffer than the surrounding background, with the modulus contrast of tumor to background of around 10:1, since liver fibrosis does not always occur with metastatic tumors. In another study published by DeWall et al. [47], viscoelastic properties of different regions of RFA regions were measured using dynamic indentation. For 11 RFA samples, the storage modulus of the outer transition zone was 3.1 ± 1.0 kPa, with a contrast of 1.6 ± 0.4 to that obtained with normal tissue. At the condensation boundary within the ablation zone, where water condensed after being driven out of the dehydrated ablation core, the modulus was 36.2 ± 9.1 kPa, with a contrast of 18.3 ± 5.5 to normal tissue. Zhang et al. reported [48], on the modulus of liver tissue with nonalcoholic fatty liver disease measured using a dynamic mechanical analysis system (ElectroForce 3200 Series, Bose Corp., Eden Prairie, MN, U.S.). Fifty-seven rats with fatty liver disease and 12 rats with normal liver were assessed. It was found that the storage modulus increased significantly from liver without steatosis (S0) to livers with moderate or severe (S2 to S4) steatosis. However, no significant differences were observed among the steatosis grades.

To study the elasticity of liver, a linear elastic solid model [49, 50] is often used to simply the complexity, while the non-linear elasticity and hybrid model have been introduced in Schwartz [51] and Bao's study [52].

$$v = \frac{3K-2\mu}{2(3K+\mu)} \quad (2.1)$$

where K is the bulk modulus, μ is the shear modulus of the elastic solid, v is the Poisson's ratio. The bulk modulus denotes the volume deformation rate under a compression pressure applied to the entire surface of the solid, for instance, the pressure of liquid with the solid emerging.

$$K = -V\frac{dP}{dV} \quad (2.2)$$

where K is the bulk modulus, P is the pressure, V is the volume, and $\frac{\mathrm{d}P}{\mathrm{d}V}$ denotes the derivative of pressure with respect to volume.

The Young's modulus, which denotes the stiffness materials, has the following relationship with the shear modulus in a homogeneous and isotropic material:

$$E = \frac{F/A}{\Delta L/L} = 2\mu(1+v) \quad (2.3)$$

where E is the Young's modulus, μ is the shear modulus, and v is the Poisson's ratio. For incompressible material, $v \approx 1/2$. Thus, the Young's modulus of liver tissue is usually expressed as $E = 3\mu$.

The shear modulus denotes the stiffness in response to a pressure applied along transverse direction. The elasticity of liver in the above studies utilizes the Young's modulus of liver, which can be converted to or from the shear modulus.

$$\mu = \frac{F/A}{\Delta x/L} \quad (2.4)$$

where F is the force applied along the transverse direction of the surface, A is the area on which the force acts, Δx is the transverse displacement, and L is the initial length along the axial direction.

An approximate relationship between the bulk modulus and density [53-56]of liver is established:

$$c = \sqrt{\frac{K}{\rho}} \quad (2.5)$$

where K is the bulk modulus, and ρ denotes the density of liver. Ultrasound speed is denoted by c. With a typical speed of sound of 1540 m/s and a density of liver that is 10^3 kg/m^3, the bulk modulus of liver is approximately 3.27×10^9 Pa, which is much higher than the typical shear modulus that is 2×10^3 Pa [23]. Thus, the Poisson's ratio in Equation (2.1) is close to 1/2, given $K >> \mu$. As a result, liver could be modelled as an incompressible [57-59] solid with a linear elasticity under small compression along certain direction.

2.5 Medical elastography

Elastography is the medical imaging analog to palpation. The Young's modulus is usually determined by measuring both the strain and stress that the tissue experiences in response to an external compression. Since the strain of local tissue is related to the Young's modulus, strain imaging is often used as a surrogate without a quantitative estimation of the Young's modulus. The strain within local tissue is distributed over a 3D

space. However, since most elastographic imaging techniques are constrained to a 2D slice; we therefore use the simplified definition of strain within the 2D imaging plane as the spatial gradient of the local displacement of tissue:

$$e_{xy} = \frac{1}{2}\left(\frac{\partial d_y}{\partial x} + \frac{\partial d_x}{\partial y}\right) \quad (2.6)$$

where d_y and d_x represent the axial and lateral displacements, respectively. The *x* and *y* denote the lateral and axial direction of a Cartesian coordinate system. In ultrasound elastography generally only the axial strain component is used, since the estimation performed along this direction can be performed with a higher spatial resolution. This is due to the fact that the sampling of the ultrasound echo signals along the beam propagation (axial) direction is significantly higher than that along the lateral direction.

$$e_y = \frac{\partial d_y}{\partial y} \quad (2.7)$$

where d_y and y are the axial displacement and axial direction of the Cartesian coordinate system, respectively. For medical elastography with image contrast based on the strain of local tissue, the equation could be rephrased as:

$$e_{ij} = \frac{\partial u_j}{\partial y_i} \quad (2.8)$$

where u_j is the displacement in jth column, and y_i is the ith row component of the axial Cartesian coordinate system [60].

Magnetic resonance imaging (MRI) and ultrasound (US) have both been used as the clinical medical imaging modality for elastography. MRI elastography, also referred as MRE, usually utilizes an external activator [61, 62] to generate a sinusoidal shear wave propagating into the patient body. A phase encoding sequence is used to track the wave front. Thus, the wavelength or the wave speed can be measured and the local elasticity property can be expressed as a function of those parameters. Taking advantage of the imaging depth and relatively high signal to noise ratio (SNR), MRE can be applied to regions where US does not easily penetrate such as the brain [63]. US elastography on the other hand is more flexible than MRE since it can be operated in a free-hand mode and does not require MRI compatible apparatus. Moreover, the ultrasound signal is reflected by the micro structures in tissue such as liver cells and the axial resolution of ultrasound is much higher than MRI. Due to the high axial resolution of ultrasound imaging in the sub-millimeter range, ultrasound radiofrequency data is ideal for displacement tracking. Ophir's group [64] was the first to generate axial strain images using a quasi-static compression for US elastography. Due to the relatively uniform compression applied to the region of interest (ROI), the high SNR in the strain image was the advantage for this class of US elastography methods. Ultrasound elastography has been applied for breast [65], renal [66], prostate [67], and liver ablation monitoring [68]. In addition to quasi-static excitations, a continuous sinusoidal excitation was also tracked with external excitation in sonoelastography [69].

Shear wave elastography [70] and acoustic radiation force impulse imaging (ARFI) [71] are examples of dynamic US elastography approaches. Dynamic elastography is based on the local displacement caused by an ultrasound push beam with either a higher intensity

or longer duration than that used in the diagnostic range. In Sarvazyan's study [70], the elasticity of local tissue is calculated by the velocity of the shear wave induced by the pushing beam. In Nightingale's study [71], ARFI was applied also with a push beam, while the stiffness of local tissue is calculated by the small axial displacement induced by the push beam. The tracking beam for shear wave imaging and ARFI is applied with a high frame rate to provide high temporal resolution. The higher stiffness region experiences less displacement than surrounding tissue. ARFI excitation has also been used to generate shear waves that are tracked to obtain shear modulus images [72]. Supersonic shear wave imaging was introduced by Bercoff et al. [73]. Sequentially focused locations were moved along the beam direction to generate a planar wavefront to generate shear waves from within the region of excitation (ROE). Shear wave tracking with a high frame rate was performed after the excitation was applied. Vibroacoustography, another approach [74] utilizes a low difference frequency (kHz) radiation force induced by two confocal high frequency (MHz) ultrasonic beams. The amplitude of the response of local tissue was then used to generate the stiffness map.

The independence from external compression apparatus makes these dynamic US elastography approaches more flexible and easy to use even for clinical applications with hard to compress regions such as through the rib cage and other remote organs [75]. However, since the mechanical perturbation amplitude for shear wave imaging and ARFI is relatively weak, the resulting SNR in the stiffness map may be compromised. Thermal effects caused by the higher intensity or longer duration push pulses on the tissue surface may cause considerable transducer heating [76].

2.6 Displacement tracking algorithms of ultrasound elastography

Since elastography is based on analyzing the local tissue's response to a mechanical perturbation, an algorithm to track the local displacement of a group of pixels representing a small ROI in local tissue is necessary. The displacement map is generated based on the similarity between the pre- and post-compression ultrasound radiofrequency data. In Ophir's study [64], a one dimensional cross-correlation algorithm was applied to track the displacement of the local tissue similarity along each A-line, with an assumption of uniform and uni-directional compression along the axial direction. To overcome the uni-directional constraint, two-dimensional (2D) sum-squared difference, sum-absolute difference, and block-based cross-correlation were also utilized. With the advantage of high sensitivity to small displacements 2D normalized cross-correlation tracking method although more computationally intensive than other 2D methods is the focus of this dissertation. The local displacement with local two-dimensional blocks or kernels is determined by the largest cross-correlation within a certain search range. Large errors might occur when using an exhaustive search, due to signal decorrelation [77]. Moreover, the signal decorrelation is related to the deformation applied to the tissue. Thus, the magnitude of the applied deformation should be limited to reduce displacement tracking errors [78].

Displacement tracking errors can be reduced using continuity constraints on the displacement map [79-81]. These continuity constraints are usually related to the physical model of an elastic solid to guarantee that the displacement map fits physical constraints. Specific optimization cost functions [82, 83] have also been applied to constrain the continuity of the displacement map, with increased computing complexity. We introduced

a multi-level tracking algorithm in our lab in 2007 [84]. The tracking strategy of the multi-level algorithm is to initially start tracking with a coarse resolution as the initial guess to the next-stage with a finer spatial resolution. Both envelope and ultrasound raw RF data can be combined in the multi-level algorithm with envelope data used for the coarse tracking and RF data for the finer resolution [85].

The displacement map calculated with cross-correlation based methods is limited by the sample resolution. To improve the tracking results with sub-sample resolution, a maximum subsample displacement could be calculated with multiple neighbors to fit a curve to further localize the maxima [86-90]. Parabolic and cosine function, frequency domain zero-padding, sinc interpolation, and iterative reconstructive filtering for sub-sample precision estimates were introduced in these studies. To balance the fitting results and computational efficiency, a parabolic fitting curve [86] is used in this dissertation.

With the sub-sample resolution enhanced displacement map, the axial strain image is generated by taking a spatial gradient of the displacement map. However, since the differentiation operation is sensitive to noise, strain noise patterns are generated with this gradient calculation. The spatial gradient can be approximated as the slope of a linear least-squared fit to the local displacement estimates to reduce the differentiation noise artifacts [91]. In addition to the displacement-gradient strain calculation, power spectrum based algorithms were also utilized [92-94]. In these studies, the local strain is estimated by the shift of the centroid of the power spectrum of the pre- and post- compression ultrasound raw RF data. In this dissertation, a 15-point linear least-square fit was used to generate the strain image from the displacement map.

2.7 Elastography for monitoring thermal ablation

An adequate ablation margin around the tumor region is a key factor for the success of percutaneous ablation treatment [17, 31, 34]. Various studies suggest that the margin should be between 0.5 – 1.0 cm extending into the tumor free region [17, 31, 34]. Thus, an effective thermal ablation margin monitoring method is crucial to guarantee a successful clinical outcome. Ultrasound, as a cost efficient and portable imaging modality, is often used to guide the insertion of the MWA antenna into the tumor [40-42]. It has not been utilized for monitoring thermal ablation therapies due to its unreliability in delineating ablated region [95]. Immediately following ablation therapy, a hyperechoic area due to out-gassing of the water vapor due to temperature elevation is observed. However, this hyperechoic region due to gas bubbles resolves within about 30 minutes after the procedure. The ablated region then appears variably as hyperechoic, hypoechoic or isoechoic in comparison with the surrounding liver [95]. The ablated tumor region can be visualized in some instances on conventional ultrasound B-mode images, however, a delineable ablation zone boundary is not always achievable, particularly on the distal side of the ablation zone due to the steam cloud created on B-mode images and the similar echogenicity between ablated region and surrounding liver tissue after the ablation procedure [68, 96-98]. The echogenicity in B mode images, which is related to the bulk modulus of tissue, lies in a similar range between the ablated and surrounding tissue [70].

Currently the most common method to monitor the ablation margin is computed tomography (CT). After the estimated thermal dose is delivered, a CT scan is performed on the ablated region to confirm the ablation volume. A complete cessation of the ablation

procedure would have to occur since the CT scan is generally not done in real time and the treatment room has to be cleared to avoid ionization radiation to physicians.

Shear modulus, which denotes the local stiffness of tissue, varies significantly between the ablated region and surrounding normal tissue [70]. Thermal ablation causes tissue protein denaturation, inducing an increase in the shear modulus or stiffness in the ablated region [99, 100]. These changes appear as regions that incur less strain upon deformation than surrounding untreated tissue [68, 99-101]. With strain and modulus imaging, ablated regions exhibit high contrast with respect to the normal, untreated background liver tissue. Since strain and modulus imaging can be performed during [84] or immediately after the ablation procedure [97, 102], complete monitoring of ablation - from guidance to preliminary follow-up is possible using ultrasound.

Ultrasound elastography has been considered as an alternative for ablation monitoring since the tissue stiffness contrast between the ablated region and surrounding tissue could be used as the contrast mechanism [68, 96, 97, 99, 103-109]. However, conventional quasi-static ultrasound elastography is dependent on either an externally applied compression [64] or internal physiological deformations [110, 111] to capture the local tissue strain contrast caused by the differing modulus contrast among these regions. These external mechanical apparatuses may also restrict use of ultrasound elastography during the ablation procedure. On the other hand, methods that use acoustic radiation force [70, 71, 104, 112-114], which appear to be suited for this task, are limited by the smaller tissue displacements generated (around 0.01 mm), and the relatively shallow imaging depth of around 8 cm, beyond which the acoustic radiation force generated is too small to deform

tissue due to attenuation of the signal [115, 116]. The resulting data are also very sensitive to physiological motion such as cardiac pulsation and respiratory artifacts.

Moreover, for monitoring MWA of liver tumor, acoustic radiation force based methods are limited by image quality and increased imaging depths required [117]. In several *ex-vivo* [71, 112, 118] and *in-vivo* [106, 119, 120] animal studies, the imaging depth of ARFI was usually within 5 cm, while the common depths of liver tumor in our study range in 5 – 15 cm. For depths greater than 8 cm, the push beam intensity is significantly attenuated even in normal liver tissue with low acoustic attenuation coefficient, resulting in an inadequate tissue perturbation and a low signal to noise ratio (SNR). In addition, cirrhotic livers and gas bubbles generated during the ablation procedure further decrease the penetration of push beams and thus compromise the image quality obtained with ARFI [104, 121].

2.8 Three-dimensional reconstruction of ultrasound images

Due to the 2D nature of imaging obtained with most ultrasound transducers, almost all of current ultrasound elastography utilizes 2D imaging planes. The lack of out of plane tissue stiffness information limits information on tumor volumes and reduces ablation region monitoring to a single slice intersecting the 3D treated volume. This could result in an inaccurate estimate of the tumor size or thermal dose delivered because the tumor or ablated region might not have a similar shape on other intersecting imaging planes.

To obtain the entire 3D distribution of tissue stiffness, 3D elastography has attracted attention including its application with free hand 1D transducer scanning [122, 123] or 2D matrix array transducer [124, 125] based acquisitions. 3D reconstruction using free hand

1D transducer scanning is based on transducer position tracking and 3D coordinate interpolation [122, 123]. When a 1D transducer is placed on the surface of a patient, laser/optical/acoustic tracking systems are used to record the relative position of the transducer. After a series of scans, corresponding 2D elastograms and their position information is input into the 3D coordinate system and an interpolated 3D elastogram can be generated. The advantage of this type of 3D elastography is the flexible positioning of the transducer and use of current technology. Nevertheless, position tracking always introduces errors and it is relatively difficult to record the tilt angle of each imaging plane and thus the final interpolation results might be biased by the imprecise 2D imaging plane coordinates.

An alternative 3D ultrasound elastography approach is based on using a mechanical driven 'wobbler' transducer [124, 126]. A wobbler transducer is an encapsulated 1D transducer, whose translational movement can be controlled by a mechanical driver. Thus, it provides more accurate imaging plane position than free hand 1D transducer acquisitions. 3D elastographic imaging with wobbler transducers can be categorized into two types: first the target 3D volume image is interpolated from the discrete 2D imaging planes, and a volume before and after the tissue deformation recorded and the local displacement and strain values could be calculated based on the volumetric data acquired. However, the computational complexity of volume based algorithms is relatively steep and thus the local tissue displacement search range is usually confined to a narrow range [126]. The second approach is based on the interpolation of 2D strain images obtained at each mechanical position of the transducer in a step and shoot imaging mode [124, 125]. A sector 3D image with a fixed angle separating each imaging plane is obtained. A series of quasi-parallel 2D

strain images is obtained at each stepped position of the wobbler transducer are then interpolated into a 3D volume based on their position. The reconstruction algorithm is similar to that of the free hand 2D transducer based acquisition, except that the imaging planes for elastography are better controlled.

In spite of the relative accurate position information obtained with a wobbler transducer, the intersection area between the imaging plane and a spherical target is reduced when the wobbler transducer moves toward the boundary of the target. The tumor or ablation region is generally ellipsoidal in shape. These quasi-parallel 2D imaging planes intersect with the ellipsoidal targets enclosing only a small region near the target boundaries. Thus, the effective information reduces as the imaging planes move from center to edge of the target. The lack of effective strain information on these imaging planes towards the edges and the resulting interpolation might lead to distortion of the target shape and inaccurate estimation of the target volume. In order to overcome the mismatch of the imaging planes and the ellipsoid target shape, we introduced a rotational acquisition method for 3D US elastography in a previous study, which is referred to as Sheaf of Ultrasound Planes Reconstruction (SOUPR) [127]. Instead of linearly translating the 2D transducer along the target surface, the acquisition planes are positioned rotationally with a specific angular increment. The sheaf of imaging planes is rotated along the central axis of the spherical or ellipsoid target. Thus, the intersection area of each rotational imaging slice with SOUPR is larger than that of the Wobbler transducer when scanning towards the boundary of the spherical target.

2.9 Image fusion of ultrasound and CT

The current clinical standard for confirming the ablation region extent is via a post-ablation CT scan. Iodine-based CT contrast [128] is often used to improve the image contrast, due to the similar Hounsfield unit between tumor and surrounding tissue [129]. The coverage of the dark region and the pre-treatment tumor area is checked for all the imaging slices. The drawback of CT monitoring scan is two-fold: it increases the ionizing radiation dose to patient and potentially clinical staff, and a cessation of the treatment would occur since CT scanning does not provide real time feedback, which increases the treatment time and the complexity of the treatment protocol.

As an alternative imaging modality, EDE has demonstrated its effectiveness for monitoring thermal ablation in animal models and human subjects. Since the image contrast with EDE is from the Young's modulus difference between the ablated region and surrounding tissue, the target ablation region size on EDE does not necessarily equal to that on CT which is caused by the density difference. Thus, a direct comparison of the monitoring results on EDE and CT will provide additional new information with different image contrast sources. Studies on which source of image contrast is more reliable to delineate the ablation size would be of interest. However, due to the freedom of positioning the ultrasound transducer, the physical geometry of the imaging plane is difficult to define for ultrasound B-mode and thereby EDE imaging. Thus, a robust image fusion algorithm is necessary to extract the corresponding imaging slice from the 3D CT images to align with that from the 2D ultrasound and EDE imaging plane.

Image fusion with ultrasound and CT can be categorized into two groups: transducer sensor based image virtual slicing and critical anatomy registration based registration. In Huang's study [130], a tracking sensor is attached on the transducer to record the position in the 3D CT coordinate system. An ECG gating method is used to register the ultrasound image of beating heart with the corresponding CT volume at the corresponding time on the cardiac cycle. The position sensor was introduced as an optical tracking system [131], with monitor installed on wall or ceiling. More recent tracking systems are based on mobile GPS sensors, with improved precision and more efficient volume reconstructions. In Hakime's study [132], liver metastases were scanned with ultrasound and CT registered imaging, with two tiny detachable position sensors. In Kim's study [133], the GPS sensor based ultrasound is further fused with MRI.

The next group of image fusion techniques is based on image registration with a landmark or critical anatomy locations. The image registration could be combined with location sensor based image fusion methods. In Hakime's study [132], CT and ultrasound images are registered with the landmark of large arteries. In Kim's study [133], liver surface and vessels were registered to fuse MRI and ultrasound. In Lee's study [134], the gallbladder surface is used as the critical landmark to overlap the imaging modalities, with a non-rigid registration method. In Wein's study [135], multiple organ edges are segmented to be registered instead of using one single critical organ. In this dissertation, we registered ultrasound and CT using the ablation needle as a landmark, along with characteristic anatomy points as markers. Thus, an in-house virtual slicing algorithm was developed to track the ablation needle position in the CT volume, and then image fusion was applied to align the ablation needle in both ultrasound and CT images.

2.10 References

1. Kumar, V., et al., *Robbins and Cotran pathologic basis of disease*. 2014: Elsevier Health Sciences.

2. Tortora, G.J. and M.T. Nielsen, *Principles of human anatomy*. Vol. 257. 1999: Wiley.

3. Kiernan, F., *The anatomy and physiology of the liver.* Philosophical transactions of the Royal Society of London, 1833. **123**: p. 711-770.

4. Walker, W.A., *Pediatric gastrointestinal disease: pathophysiology, diagnosis, management*. Vol. 1. 2004: PMPH-USA.

5. Ryder, S.D., *Guidelines for the diagnosis and treatment of hepatocellular carcinoma (HCC) in adults.* Gut, 2003. **52**(suppl 3): p. iii1-iii8.

6. Ahmed, I. and D.N. Lobo, *Malignant tumours of the liver.* Surgery (Oxford), 2009. **27**(1): p. 30-37.

7. Stewart, B. and C.P. Wild, *World cancer report 2014.* Health, 2017.

8. Arzumanyan, A., H.M. Reis, and M.A. Feitelson, *Pathogenic mechanisms in HBV-and HCV-associated hepatocellular carcinoma.* Nature Reviews Cancer, 2013. **13**(2): p. 123-135.

9. Liver, E.A.F.T.S.O.T., *EASL clinical practice guidelines: Management of chronic hepatitis B virus infection.* Journal of hepatology, 2012. **57**(1): p. 167-185.

10. Bosch, F.X., et al., *Primary liver cancer: worldwide incidence and trends.* Gastroenterology, 2004. **127**(5): p. S5-S16.

11. Kensler, T.W., et al., *Aflatoxin: a 50-year odyssey of mechanistic and translational toxicology.* Toxicological Sciences, 2011. **120**(suppl 1): p. S28-S48.

12. Chuang, S.-C., C. La Vecchia, and P. Boffetta, *Liver cancer: descriptive epidemiology and risk factors other than HBV and HCV infection.* Cancer letters, 2009. **286**(1): p. 9-14.

13. Fattovich, G., et al., *Hepatocellular carcinoma in cirrhosis: incidence and risk factors.* Gastroenterology, 2004. **127**(5): p. S35-S50.

14. Sheets, S.S.F., *Liver and Intrahepatic Bile Duct Cancer.* Surveillance, Epidemiology, and End Results (SEER) Program, 2015.

15. Jemal, A., et al., *Global cancer statistics.* CA: a cancer journal for clinicians, 2011. **61**(2): p. 69-90.

16. El–Serag, H.B. and K.L. Rudolph, *Hepatocellular carcinoma: epidemiology and molecular carcinogenesis.* Gastroenterology, 2007. **132**(7): p. 2557-2576.

17. Lencioni, R. and L. Crocetti, *Radiofrequency ablation of liver cancer.* Tech Vasc Interv Radiol, 2007. **10**(1): p. 38-46.

18. Ziol, M., et al., *Noninvasive assessment of liver fibrosis by measurement of stiffness in patients with chronic hepatitis C.* Hepatology, 2005. **41**(1): p. 48-54.

19. Chan, H.L., et al., *Alanine aminotransferase-based algorithms of liver stiffness measurement by transient elastography (Fibroscan) for liver fibrosis in chronic hepatitis B.* J Viral Hepat, 2009. **16**(1): p. 36-44.

20. Foucher, J., et al., *Prevalence and factors associated with failure of liver stiffness measurement using FibroScan in a prospective study of 2114 examinations.* Eur J Gastroenterol Hepatol, 2006. **18**(4): p. 411-2.

21. Vergniol, J., et al., *Noninvasive tests for fibrosis and liver stiffness predict 5-year outcomes of patients with chronic hepatitis C.* Gastroenterology, 2011. **140**(7): p. 1970-9, 1979 e1-3.

22. Jung, K.S., et al., *Risk assessment of hepatitis B virus-related hepatocellular carcinoma development using liver stiffness measurement (FibroScan).* Hepatology, 2011. **53**(3): p. 885-94.

23. Mueller, S. and L. Sandrin, *Liver stiffness: a novel parameter for the diagnosis of liver disease.* Hepat Med, 2010. **2**: p. 49-67.

24. Liang, P. and Y. Wang, *Microwave ablation of hepatocellular carcinoma.* Oncology, 2007. **72 Suppl 1**: p. 124-31.

25. Duffy, J.P., et al., *Liver transplantation criteria for hepatocellular carcinoma should be expanded: a 22-year experience with 467 patients at UCLA.* Annals of surgery, 2007. **246**(3): p. 502-511.

26. Cheng, J.C.-H., et al., *Radiation-induced liver disease after three-dimensional conformal radiotherapy for patients with hepatocellular carcinoma: dosimetric analysis and implication.* International Journal of Radiation Oncology* Biology* Physics, 2002. **54**(1): p. 156-162.

27. Baron, R.L., et al., *Hepatocellular carcinoma: evaluation with biphasic, contrast-enhanced, helical CT.* Radiology, 1996. **199**(2): p. 505-511.

28. Cheung, P.C., et al., *Reproducibility of lung tumor position and reduction of lung mass within the planning target volume using active breathing control (ABC).* International Journal of Radiation Oncology* Biology* Physics, 2003. **57**(5): p. 1437-1442.

29. Rusthoven, K.E., et al., *Multi-institutional phase I/II trial of stereotactic body radiation therapy for liver metastases.* Journal of Clinical Oncology, 2009. **27**(10): p. 1572-1578.

30. Widmann, G., et al., *Respiratory motion control for stereotactic and robotic liver interventions.* The International Journal of Medical Robotics and Computer Assisted Surgery, 2010. **6**(3): p. 343-349.

31. Lencioni, R. and L. Crocetti, *Local-regional treatment of hepatocellular carcinoma.* Radiology, 2012. **262**(1): p. 43-58.

32. Shiina, S., et al., *Radiofrequency ablation for hepatocellular carcinoma: 10-year outcome and prognostic factors.* Am J Gastroenterol, 2012. **107**(4): p. 569-77; quiz 578.

33. Lu, M.D., et al., *Percutaneous microwave and radiofrequency ablation for hepatocellular carcinoma: a retrospective comparative study.* J Gastroenterol, 2005. **40**(11): p. 1054-60.

34. Maluccio, M. and A. Covey, *Recent progress in understanding, diagnosing, and treating hepatocellular carcinoma.* CA Cancer J Clin, 2012. **62**(6): p. 394-9.

35. Murakami, R., et al., *Treatment of hepatocellular carcinoma: value of percutaneous microwave coagulation.* AJR Am J Roentgenol, 1995. **164**(5): p. 1159-64.

36. Qian, G.J., et al., *Efficacy of microwave versus radiofrequency ablation for treatment of small hepatocellular carcinoma: experimental and clinical studies.* Eur Radiol, 2012. **22**(9): p. 1983-90.

37. Swan, R.Z., et al., *Operative microwave ablation for hepatocellular carcinoma: complications, recurrence, and long-term outcomes.* J Gastrointest Surg, 2013. **17**(4): p. 719-29.

38. Shibata, T., et al., *Small hepatocellular carcinoma: comparison of radio-frequency ablation and percutaneous microwave coagulation therapy.* Radiology, 2002. **223**(2): p. 331-7.

39. Harari, C.M., et al., *Microwave Ablation: Comparison of Simultaneous and Sequential Activation of Multiple Antennas in Liver Model Systems.* Radiology, 2016. **278**(1): p. 95-103.

40. Lubner, M.G., et al., *Microwave ablation of hepatic malignancy.* Semin Intervent Radiol, 2013. **30**(1): p. 56-66.

41. Wells, S.A., et al., *Liver Ablation: Best Practice.* Radiol Clin North Am, 2015. **53**(5): p. 933-71.

42. Ziemlewicz, T.J., et al., *Hepatic Tumor Ablation.* Surg Clin North Am, 2016. **96**(2): p. 315-39.

43. Ziemlewicz, T.J., et al., *Percutaneous microwave ablation of hepatocellular carcinoma with a gas-cooled system: initial clinical results with 107 tumors.* J Vasc Interv Radiol, 2015. **26**(1): p. 62-8.

44. Bharat, S., et al., *Monitoring stiffness changes in lesions after radiofrequency ablation at different temperatures and durations of ablation.* Ultrasound in medicine & biology, 2005. **31**(3): p. 415-422.

45. Yeh, W.-C., et al., *Elastic modulus measurements of human liver and correlation with pathology.* Ultrasound in medicine & biology, 2002. **28**(4): p. 467-474.

46. DeWall, R.J., et al., *Characterizing the compression-dependent viscoelastic properties of human hepatic pathologies using dynamic compression testing.* Physics in medicine and biology, 2012. **57**(8): p. 2273.

47. DeWall, R.J., T. Varghese, and C.L. Brace, *Quantifying local stiffness variations in radiofrequency ablations with dynamic indentation.* IEEE Transactions on Biomedical Engineering, 2012. **59**(3): p. 728-735.

48. Zhang, X., et al., *Dynamic mechanical analysis to assess viscoelasticity of liver tissue in a rat model of nonalcoholic fatty liver disease.* Medical Engineering & Physics, 2017. **44**: p. 79-86.

49. Sarvazyan, A., *Low-frequency acoustic characteristics of biological tissues.* Mechanics of Composite Materials, 1975. **11**(4): p. 594-597.

50. Parker, K., et al., *Tissue response to mechanical vibrations for "sonoelasticity imaging".* Ultrasound in medicine & biology, 1990. **16**(3): p. 241-246.

51. Schwartz, J.-M., et al., *Modelling liver tissue properties using a non-linear visco-elastic model for surgery simulation.* Medical Image Analysis, 2005. **9**(2): p. 103-112.

52. Bao, Y., et al., *A new hybrid viscoelastic soft tissue model based on meshless method for haptic surgical simulation.* The open biomedical engineering journal, 2013. **7**: p. 116.

53. Jiang, J., T.J. Hall, and A.M. Sommer, *A novel image formation method for ultrasonic strain imaging.* Ultrasound in medicine & biology, 2007. **33**(4): p. 643-652.

54. Kallel, F. and M. Bertrand, *Tissue elasticity reconstruction using linear perturbation method.* IEEE Transactions on Medical Imaging, 1996. **15**(3): p. 299-313.

55. Sumi, C., A. Suzuki, and K. Nakayama, *Estimation of shear modulus distribution in soft tissue from strain distribution.* IEEE Transactions on Biomedical Engineering, 1995. **42**(2): p. 193-202.

56. Doyley, M., P. Meaney, and J. Bamber, *Evaluation of an iterative reconstruction method for quantitative elastography.* Physics in medicine and biology, 2000. **45**(6): p. 1521.

57. Lubinski, M.A., et al., *Lateral displacement estimation using tissue incompressibility.* IEEE Transactions on Ultrasonics, Ferroelectrics, and Frequency Control, 1996. **43**(2): p. 247-256.

58. Albocher, U., et al., *Adjoint-weighted equation for inverse problems of incompressible plane-stress elasticity.* Computer Methods in Applied Mechanics and Engineering, 2009. **198**(30): p. 2412-2420.

59. Barbone, P.E. and J.C. Bamber, *Quantitative elasticity imaging: what can and cannot be inferred from strain images.* Physics in medicine and biology, 2002. **47**(12): p. 2147.

60. Ophir, J., et al., *Elastography: a quantitative method for imaging the elasticity of biological tissues.* Ultrasonic imaging, 1991. **13**(2): p. 111-134.

61. Muthupillai, R., et al., *Magnetic resonance elastography by direct visualization of propagating acoustic strain waves.* Science, 1995. **269**(5232): p. 1854-7.

62. Huwart, L., et al., *Liver fibrosis: non-invasive assessment with MR elastography.* NMR Biomed, 2006. **19**(2): p. 173-9.

63. Kruse, S.A., et al., *Magnetic resonance elastography of the brain.* Neuroimage, 2008. **39**(1): p. 231-7.

64. Ophir, J., et al., *Elastography: a quantitative method for imaging the elasticity of biological tissues.* Ultrason Imaging, 1991. **13**(2): p. 111-34.

65. Garra, B.S., et al., *Elastography of breast lesions: initial clinical results.* Radiology, 1997. **202**(1): p. 79-86.

66. Emelianov, S., et al., *Elasticity imaging for early detection of renal pathology.* Ultrasound in medicine & biology, 1995. **21**(7): p. 871-883.

67. Kallel, F., et al., *Elastographic imaging of the normal canine prostate in vitro.* Ultrason Imaging, 1999. **21**(3): p. 201-15.

68. Varghese, T., J.A. Zagzebski, and F.T. Lee, Jr., *Elastographic imaging of thermal lesions in the liver in vivo following radiofrequency ablation: preliminary results.* Ultrasound Med Biol, 2002. **28**(11-12): p. 1467-73.

69. Gao, L., et al., *Sonoelasticity imaging: theory and experimental verification.* The Journal of the Acoustical Society of America, 1995. **97**(6): p. 3875-3886.

70. Sarvazyan, A.P., et al., *Shear wave elasticity imaging: a new ultrasonic technology of medical diagnostics.* Ultrasound Med Biol, 1998. **24**(9): p. 1419-35.

71. Nightingale, K.R., et al., *On the feasibility of remote palpation using acoustic radiation force.* J Acoust Soc Am, 2001. **110**(1): p. 625-34.

72. Nightingale, K., *Acoustic radiation force impulse (ARFI) imaging: a review.* Current medical imaging reviews, 2011. **7**(4): p. 328-339.

73. Bercoff, J., M. Tanter, and M. Fink, *Supersonic shear imaging: a new technique for soft tissue elasticity mapping.* IEEE transactions on ultrasonics, ferroelectrics, and frequency control, 2004. **51**(4): p. 396-409.

74. Konofagou, E., J. Thierman, and K. Hynynen. *Ultrasound surgery monitoring using vibroacoustography-a simulation study*. in *Ultrasonics Symposium, 2000 IEEE*. 2000. IEEE.

75. Catheline, S., F. Wu, and M. Fink, *A solution to diffraction biases in sonoelasticity: the acoustic impulse technique.* J Acoust Soc Am, 1999. **105**(5): p. 2941-50.

76. Palmeri, M.L. and K.R. Nightingale, *On the thermal effects associated with radiation force imaging of soft tissue.* IEEE Trans Ultrason Ferroelectr Freq Control, 2004. **51**(5): p. 551-65.

77. Varghese, T. and J. Ophir, *Characterization of elastographic noise using the envelope of echo signals.* Ultrasound in medicine & biology, 1998. **24**(4): p. 543-555.

78. Varghese, T. and J. Ophir, *A theoretical framework for performance characterization of elastography: The strain filter.* IEEE Transactions on Ultrasonics, Ferroelectrics, and Frequency Control, 1997. **44**(1): p. 164-172.

79. Chen, L., et al., *A quality-guided displacement tracking algorithm for ultrasonic elasticity imaging.* Medical image analysis, 2009. **13**(2): p. 286-296.

80. Zhu, Y. and T.J. Hall, *A modified block matching method for real-time freehand strain imaging.* Ultrasonic imaging, 2002. **24**(3): p. 161-176.

81. Pesavento, A., et al., *A time-efficient and accurate strain estimation concept for ultrasonic elastography using iterative phase zero estimation.* IEEE transactions on ultrasonics, ferroelectrics, and frequency control, 1999. **46**(5): p. 1057-1067.

82. Jiang, J. and T.J. Hall, *A generalized speckle tracking algorithm for ultrasonic strain imaging using dynamic programming.* Ultrasound in medicine & biology, 2009. **35**(11): p. 1863-1879.

83. Rivaz, H., et al., *Ultrasound elastography: a dynamic programming approach.* IEEE transactions on medical imaging, 2008. **27**(10): p. 1373-1377.

84. Shi, H. and T. Varghese, *Two-dimensional multi-level strain estimation for discontinuous tissue.* Physics in medicine and biology, 2007. **52**(2): p. 389.

85. Chen, H., H. Shi, and T. Varghese, *Improvement of elastographic displacement estimation using a two-step cross-correlation method.* Ultrasound in medicine & biology, 2007. **33**(1): p. 48-56.

86. Cespedes, I., et al., *Methods for estimation of subsample time delays of digitized echo signals.* Ultrasonic imaging, 1995. **17**(2): p. 142-171.

87. McCormick, M.M. and T. Varghese, *An approach to unbiased subsample interpolation for motion tracking.* Ultrasonic imaging, 2013. **35**(2): p. 76-89.

88. Basarab, A., H. Liebgott, and P. Delachartre, *Analytic estimation of subsample spatial shift using the phases of multidimensional analytic signals.* IEEE Transactions on Image Processing, 2009. **18**(2): p. 440-447.

89. Viola, F. and W.F. Walker, *A spline-based algorithm for continuous time-delay estimation using sampled data.* IEEE transactions on ultrasonics, ferroelectrics, and frequency control, 2005. **52**(1): p. 80-93.

90. Viola, F., et al., *Multi-dimensional spline-based estimator (muse) for motion estimation: algorithm development and initial results.* Annals of biomedical engineering, 2008. **36**(12): p. 1942-1960.

91. Kallel, F. and J. Ophir, *A least-squares strain estimator for elastography.* Ultrasonic imaging, 1997. **19**(3): p. 195-208.

92. Varghese, T., et al., *Direct strain estimation in elastography using spectral cross-correlation.* Ultrasound in medicine & biology, 2000. **26**(9): p. 1525-1537.

93. Konofagou, E., et al., *Power spectral strain estimators in elastography.* Ultrasound in medicine & biology, 1999. **25**(7): p. 1115-1129.

94. Talhami, H., L. Wilson, and M. Neale, *Spectral tissue strain: A new technique for imaging tissue strain using intravascular ultrasound.* Ultrasound in medicine & biology, 1994. **20**(8): p. 759-772.

95. Solbiati, L., et al., *Percutaneous US-guided radio-frequency tissue ablation of liver metastases: treatment and follow-up in 16 patients.* Radiology, 1997. **202**(1): p. 195-203.

96. Bharat, S., et al., *Radio-frequency ablation electrode displacement elastography: a phantom study.* Med Phys, 2008. **35**(6): p. 2432-42.

97. Rubert, N., et al., *Electrode displacement strain imaging of thermally-ablated liver tissue in an in vivo animal model.* Med Phys, 2010. **37**(3): p. 1075-82.

98. Yang, W., et al., *Post-procedure Evaluation of Microwave Ablations of Hepatocellular Carcinomas Using Electrode Displacement Elastography.* Ultrasound in Medicine & Biology, 2016.

99. Varghese, T., et al., *Elastographic measurement of the area and volume of thermal lesions resulting from radiofrequency ablation: pathologic correlation.* AJR Am J Roentgenol, 2003. **181**(3): p. 701-7.

100. Varghese, T., et al., *Impact of gas bubbles generated during interstitial ablation on elastographic depiction of in vitro thermal lesions.* J Ultrasound Med, 2004. **23**(4): p. 535-44; quiz 545-6.

101. Varghese, T.Z.J., Techavipoo U, Chen Q,, *Elastographic Imaging of in-vivo soft tissue*, 2002: US. .

102. Jiang, J., et al., *Ultrasound-based relative elastic modulus imaging for visualizing thermal ablation zones in a porcine model.* Phys Med Biol, 2010. **55**(8): p. 2281-306.

103. Bharat, S., et al., *Monitoring stiffness changes in lesions after radiofrequency ablation at different temperatures and durations of ablation.* Ultrasound Med Biol, 2005. **31**(3): p. 415-22.

104. Fahey, B.J., et al., *In vivo guidance and assessment of liver radio-frequency ablation with acoustic radiation force elastography.* Ultrasound Med Biol, 2008. **34**(10): p. 1590-603.

105. Kolokythas, O., et al., *Ultrasound-based elastography: a novel approach to assess radio frequency ablation of liver masses performed with expandable ablation probes: a feasibility study.* J Ultrasound Med, 2008. **27**(6): p. 935-46.

106. Mariani, A., et al., *Real time shear waves elastography monitoring of thermal ablation: in vivo evaluation in pig livers.* J Surg Res, 2014. **188**(1): p. 37-43.

107. Righetti, R., et al., *Elastographic characterization of HIFU-induced lesions in canine livers.* Ultrasound Med Biol, 1999. **25**(7): p. 1099-113.

108. Zhang, M., et al., *Real-time sonoelastography of hepatic thermal lesions in a swine model.* Med Phys, 2008. **35**(9): p. 4132-41.

109. Zhou, Z., et al., *A survey of ultrasound elastography approaches to percutaneous ablation monitoring.* Proc Inst Mech Eng H, 2014. **228**(10): p. 1069-82.

110. Varghese, T., et al., *Ultrasonic imaging of myocardial strain using cardiac elastography.* Ultrason Imaging, 2003. **25**(1): p. 1-16.

111. Shi, H. and T. Varghese, *Two-dimensional multi-level strain estimation for discontinuous tissue.* Phys Med Biol, 2007. **52**(2): p. 389-401.

112. Bing, K.F., et al., *Combined ultrasonic thermal ablation with interleaved ARFI image monitoring using a single diagnostic curvilinear array: a feasibility study.* Ultrason Imaging, 2011. **33**(4): p. 217-32.

113. Arnal, B., M. Pernot, and M. Tanter, *Monitoring of thermal therapy based on shear modulus changes: I. shear wave thermometry.* IEEE Trans Ultrason Ferroelectr Freq Control, 2011. **58**(2): p. 369-78.

114. Hoyt, K., B. Castaneda, and K.J. Parker, *Two-dimensional sonoelastographic shear velocity imaging.* Ultrasound Med Biol, 2008. **34**(2): p. 276-88.

115. Deng, Y., et al., *Analyzing the Impact of Increasing Mechanical Index and Energy Deposition on Shear Wave Speed Reconstruction in Human Liver.* Ultrasound in medicine & biology, 2015.

116. Zhao, H., et al., *Bias observed in time-of-flight shear wave speed measurements using radiation force of a focused ultrasound beam.* Ultrasound in medicine & biology, 2011. **37**(11): p. 1884-1892.

117. Correa-Gallego, C., et al., *Intraoperative ultrasound and tissue elastography measurements do not predict the size of hepatic microwave ablations.* Academic radiology, 2014. **21**(1): p. 72-78.

118. Shahmirzadi, D., et al., *Ex Vivo characterization of canine liver tissue viscoelasticity after high-intensity focused ultrasound ablation.* Ultrasound in medicine & biology, 2014. **40**(2): p. 341-350.

119. Zhang, M., et al., *Real-time sonoelastography of hepatic thermal lesions in a swine model.* Medical physics, 2008. **35**(9): p. 4132-4141.

120. Subramanian, S., et al., *In vivo thermal ablation monitoring using ultrasound echo decorrelation imaging.* Ultrasound in medicine & biology, 2014. **40**(1): p. 102-114.

121. Lizzi, F.L., et al., *Radiation-force technique to monitor lesions during ultrasonic therapy.* Ultrasound Med Biol, 2003. **29**(11): p. 1593-605.

122. Lindop, J.E., et al., *3D elastography using freehand ultrasound.* Ultrasound Med Biol, 2006. **32**(4): p. 529-45.

123. Gee, A., et al., *Processing and visualizing three-dimensional ultrasound data.* Br J Radiol, 2004. **77 Spec No 2**: p. S186-93.

124. Treece, G.M., et al., *Freehand ultrasound elastography with a 3-D probe.* Ultrasound Med Biol, 2008. **34**(3): p. 463-74.

125. Bharat, S., et al., *Three-dimensional electrode displacement elastography using the Siemens C7F2 fourSight four-dimensional ultrasound transducer.* Ultrasound Med Biol, 2008. **34**(8): p. 1307-16.

126. Rivaz, H., et al., *Ultrasound elastography: a dynamic programming approach.* IEEE Trans Med Imaging, 2008. **27**(10): p. 1373-7.

127. Ingle, A. and T. Varghese, *Three-dimensional sheaf of ultrasound planes reconstruction (SOUPR) of ablated volumes.* IEEE Trans Med Imaging, 2014. **33**(8): p. 1677-88.

128. Lusic, H. and M.W. Grinstaff, *X-ray-computed tomography contrast agents.* Chemical reviews, 2012. **113**(3): p. 1641-1666.

129. Berber, E., et al., *Use of CT Hounsfield unit density to identify ablated tumor after laparoscopic radiofrequency ablation of hepatic tumorsrid="" id="" Presented at the annual meeting of the Society of American Gastrointestinal Endoscopic Surgeons (SAGES), Atlanta, Georgia, USA, 29 March–1 April 2000.* Surgical endoscopy, 2000. **14**(9): p. 799-804.

130. Huang, X., et al., *Dynamic 2D ultrasound and 3D CT image registration of the beating heart.* IEEE transactions on medical imaging, 2009. **28**(8): p. 1179-1189.

131. Kaspersen, J., et al., *Three-dimensional ultrasound-based navigation combined with preoperative CT during abdominal interventions: a feasibility study.* Cardiovascular and interventional radiology, 2003. **26**(4): p. 347-356.

132. Hakime, A., et al., *Clinical evaluation of spatial accuracy of a fusion imaging technique combining previously acquired computed tomography and real-time ultrasound for imaging of liver metastases.* Cardiovascular and interventional radiology, 2011. **34**(2): p. 338-344.

133. Kim, A.Y., et al., *Automatic Registration between Real-Time Ultrasonography and Pre-Procedural Magnetic Resonance Images: A Prospective Comparison between Two Registration Methods by Liver Surface and Vessel and by Liver Surface Only.* Ultrasound in medicine & biology, 2016. **42**(7): p. 1627-1636.

134. Lee, D., et al., *Non-rigid registration between 3D ultrasound and CT images of the liver based on intensity and gradient information.* Physics in medicine and biology, 2010. **56**(1): p. 117.

135. Wein, W., et al., *Automatic CT-ultrasound registration for diagnostic imaging and image-guided intervention.* Medical image analysis, 2008. **12**(5): p. 577-585.

Chapter 3 Clinical application of EDE for monitoring MWA

3.1 Introduction

We previously introduced a novel, quasi-static ultrasound elastography technique, referred to as electrode displacement elastography (EDE) [1-3], designed specifically for monitoring percutaneous ablation procedures. Here the local tissue deformation for elastography is induced by manual perturbation of the ablation antenna [1]. In this chapter[1], we investigated the feasibility of EDE in a clinical study done on 44 patients diagnosed with HCC and treated with MWA. The delineation of the ablated region on EDE images is compared with ablated region contours taken from conventional B mode images. Comparisons between the two modalities are made of the estimated ablation zone areas and of the detectability using contrast and contrast to noise ratio (CNR) features.

[1]This chapter is adapted from **Yang W**, Ziemlewicz TJ, Varghese T, Alexander ML, Rubert N, Ingle AN, Lubner MG, Hinshaw JL, Wells SA, Lee FT Jr, Zagzebski JA. Post-procedure evaluation of microwave ablations of hepatocellular carcinomas using electrode displacement elastography. Ultrasound Med Biol. 2016. pii: S0301-5629(16)30174-0. doi: 10.1016/j.ultrasmedbio.2016.07.015. PubMed PMID: 27592561

3.2 Materials and Methods

3.2.1 Patients and MWA system

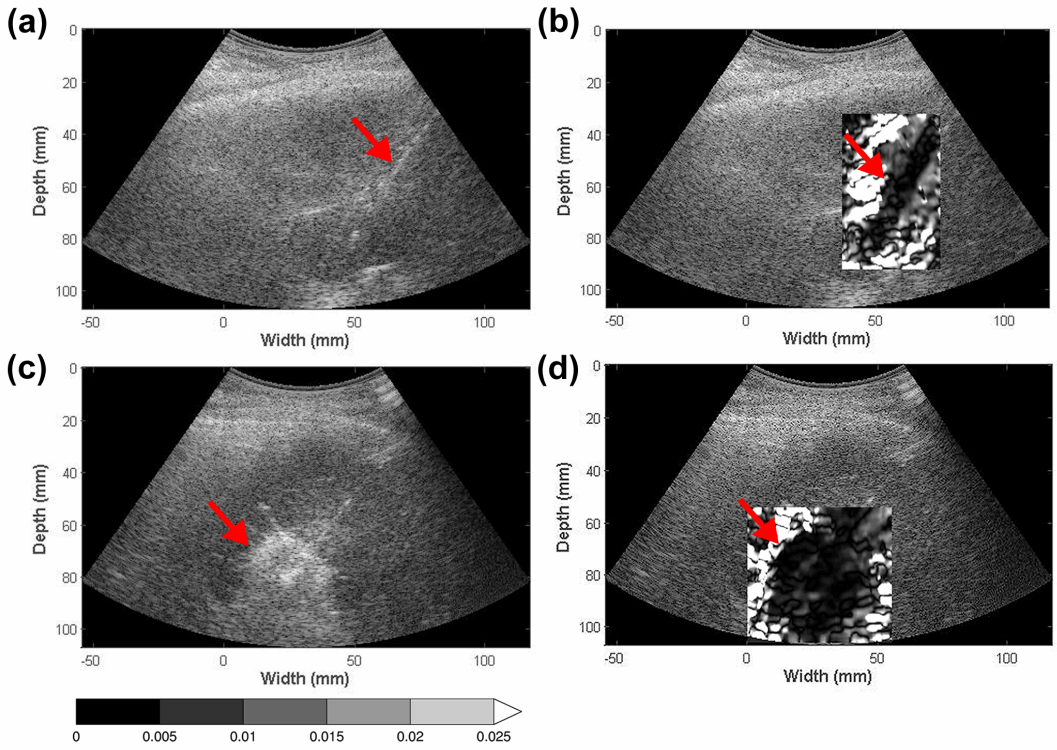

Fig. 3.1. Pre- and post- ablation regions depicted on EDE strain and corresponding B mode images for a patient diagnosed with a 2.0 cm HCC tumor. The targeted tumor region on B-mode (a) and EDE (b) are shown in the top row, while the ablated region on B-mode (c) and corresponding EDE strain (d) are shown in the bottom row. The ablation needle on the pre-treatment image (a) is identified by the echogenic line on the B mode image. EDE strain images were generated with a 3.5 wavelength × 7 A line cross-correlation kernel. The upper limit of the strain value was 2.5% and all values beyond were saturated as indicated by the colorbar.

Table 3.1. Statistics of HCC patients reported in this study.

Patient features	**Value**
Age	64.4 ± 9.3 years
Gender (M/F)	34/10
Tumor size	2.2 ± 0.8 cm
Cirrhosis (Y/N)	37/7
Fatty Liver (Y/N)	1/43
Prior Treatment (Y/N)	10/34

Forty-four patients who underwent MWA for their HCC tumors were involved in this study. Informed consent to participate in this study was obtained prior to the ablation procedure under a protocol approved by the institutional review board (IRB) at the University of Wisconsin-Madison. Patients received MWA treatments under general anesthesia. Ultrasound radiofrequency data for EDE were acquired following antenna insertion, prior to onset of ablation, and immediately after the ablation procedure prior to the ablation antenna being removed from the insertion site.

MWA was delivered using a Neuwave Medical Certus 140 (Madison, WI, USA) operating at 2.45 GHz. Ablation duration and power were adjusted for each patient depending on the tumor size and location, with typical values of 5 min and 65 W, respectively. The MWA antenna was inserted under conventional ultrasound B mode

imaging guidance in a CT imaging suite. In several patients multiple MWA antennae (maximum of 3, typically 2) were inserted at the same ablation site. MWA antenna position and placement within the ablation region were also confirmed using CT scans prior to the ablation procedure in cases where ultrasound B-mode imaging was not definitive. B-mode and EDE strain images were obtained after completion of the active ablation procedure, but prior to the complete dissipation of the gas bubbles to evaluate the post-treatment appearance.

3.2.2 EDE techniques and Strain image processing

The mechanical stimulus for EDE was induced by a physician by manually perturbing the ablation antenna. A small displacement (typically around 1 mm) was applied to the ablated region through the perturbation. No side effects such as additional bleeding or patient discomfort were noted as a result of the EDE procedure.

Loops of ultrasound radiofrequency data were recorded during the perturbation of the antenna. Data were acquired using a Siemens ACUSON S2000 system equipped with a curvilinear array transducer (6C1 HD) operating at a 4 MHz center frequency. Two frames of radiofrequency data were selected as “pre” and “post” deformation frames after reviewing the entire loop of images generated from the radiofrequency data. These data were then processed to estimate local tissue displacements. We selected frames such that the correlation coefficient between kernels did not drop below 0.75 at all depths to ensure that local displacements estimated are accurate [4]. A two dimensional (2D) cross-correlation based tracking algorithm [5] was applied, where the cross-correlation kernel dimensions used were 3.5 wavelengths × 7 A lines. Assuming a sound speed of 1540 m/s

and at a depth of 8 cm, the physical dimensions of the kernel were 1.35 mm × 3.29 mm along the axial and lateral direction, respectively. The kernel dimensions used are larger than those applied in breast elastography, where high frequency linear array transducers are used and kernel sizes of 0.385 mm (axial) × 0.507 mm (lateral) are applied [6]. The larger kernel size was required in this study due to increased attenuation at deeper imaging locations, reducing the echo data signal-to-noise ratio (SNR), lower center frequency, and because of the smaller deformations introduced with EDE. The ultrasound RF data with relatively low SNR require a larger tracking kernel to improve the tracking results with 2D cross-correlation. Adjacent cross correlation kernels overlapped by 75% along the beam direction and one A-line in the lateral direction. Local displacement estimates were fit with a 15-point (0.375 μs, or 0.29 mm) linear, least squares fit, and the local strain values were computed as the linear regression of the local displacements with a 15-point linear least square fit. EDE based strain images were generated offline on an Intel Core 2 Duo computer, with the tracking algorithm implemented using MATLAB (MathWorks, Inc. Natick, MA).

To account for the fan shaped geometry of data acquired using the curvilinear transducer, scan conversion was applied after displacement and strain estimations along the direction of the A-lines. A bi-linear interpolation was then applied to the strain values to calculate pixel values at scan converted positions on a rectangular grid.

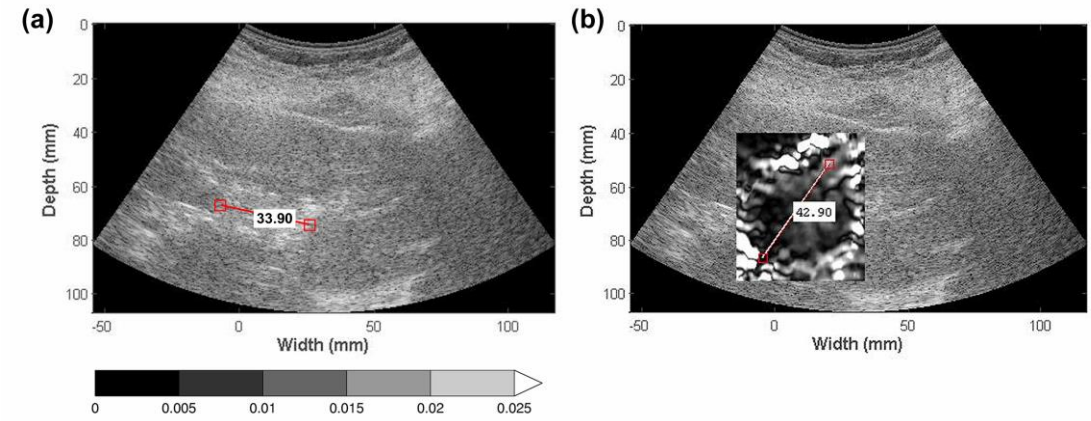

Fig. 3.2. Ablation region dimension measurement on EDE and B mode images. The maximum ablation region dimension on B mode (a) and EDE strain images (b) was measured. The gas bubble cloud on B mode images may be distorted leading to the maximum dimension being measured along different axes when compared to the EDE strain image as shown in (a) and (b).

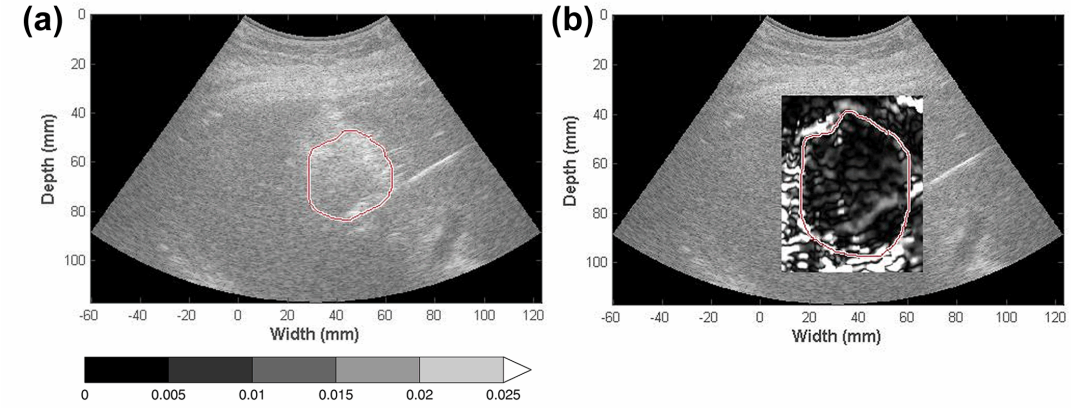

Fig. 3.3. Ablation area measurement on EDE and B mode images. The ablation region on B mode (a) and EDE images (b) was segmented manually with the segmented area calculated using Equation (3.1). The gas bubble cloud depicted as the hyperechoic region on B mode images (a) tended to accumulate at variable locations.

3.2.3 Evaluation metrics for EDE vs. conventional B mode imaging

Area of the ablation region: Ablated zones are recognized in EDE because they exhibit lower strain than surrounding, untreated tissue. The estimated area of the ablation region was used as a feature to compare the 2D distribution of the low-strain zone on EDE and the hyperechoic region on B mode images. The ablation region was segmented manually on both sets of images. The area of the ablation region, S was calculated using:

$$S = \Delta \times N \tag{3.1}$$

where Δ is the image pixel size and N is the number of pixels inside the segmented region.

Ablation region contrast: The contrast of the ablation region is defined as:

$$C = \left| \frac{I_o - I_b}{I_o + I_b} \right| \tag{3.2}$$

where C represents the contrast, I_o is the mean image pixel value of a rectangular region of interest (ROI) positioned within the ablated region, and I_b is the mean pixel value of a similar sized rectangular ROI adjacent to the ablated region.

For EDE, the ROI of the ablated region was defined within the dark ellipse (see Fig 3.1 in Results, for example), which is the region with increased tissue stiffness. The background ROI was defined outside the bright halo around the ablated region. The upper limit of the strain values on the EDE images was set to a maximum of 0.025 or 2.5%, which was the approximate upper limit of the strain value introduced by the small needle perturbation. For B mode images, the ROI of the ablated region was defined within the

bright gas bubble region, and the background ROI was selected from a region adjacent to the bubbles.

CNR of the ablation region: CNR, the contrast-to-noise ratio takes into consideration the noise level of the ablation region and background and is used to describe the detectability of the ablated region with the EDE strain image [7]. The CNR of the ablation region was calculated using:

$$CNR = 20log_{10}(\frac{|I_o - I_b|}{\sqrt{\sigma_o^2 + \sigma_b^2}}) \quad (3.3)$$

where σ_o^2 and σ_b^2 represent the variance of the strain estimates within the ROI defined in the ablation region and background, respectively.

3.2.4 Measurement methods

Visualization and comparison of ablated regions on EDE strain and B mode images in this chapter was not designed as a blinded study. A single observer with experience in *ex-vivo* and *in-vivo* MWA experiments delineated the ablated region area and selected the ROI for estimation of the contrast and CNR for both B mode and EDE strain images. B-mode images were analyzed before EDE strain images.

3.2.5 Statistical analysis

The area, contrast and CNR of the ablated region on EDE strain and B-mode images were compared pairwise for each patient studied. These were presented in the form of a scatter plot. Box and whisker plots were then used to perform a clustered comparison for the 40 patients, with the median value being the center bar within the box, the first and

second quartile values denoted as the upper and lower borders of the box, and the 10^{th} and 90^{th} percentage values denoted by the top and bottom bar. The p value using a single sided t-test for the hypothesis that the values generated with EDE are higher than those with B mode images were calculated and represented with number of stars above the box and whisker plots.

3.3 Results

Table 3.2. Details on HCC tumor depths and EDE imaging success on 44 patients.

HCC Depth	**HCC Number**	**EDE Success**	**EDE Success Rate**
< 5 cm	9	8/9	88.9%
> 5 cm < 8 cm	22	20/22	90.9%
> 8 cm < 10 cm	5	5/5	100%
> 10 cm < 15 cm	8	7/8	87.5%
Total	44	40/44	90.9%

The high modulus contrast between the ablated region and the surrounding healthy tissue leads to a “saturated halo” appearance around the ablation zone on the EDE strain image, as shown in Fig. 3.1. Previous studies on TM phantoms and *in-vivo* porcine models have shown that the ablation zone on EDE matches histopathological ablation contours

well in terms of target area and dimensions [3, 8, 9]. EDE images that exhibited clearly distinguishable ablation regions were obtained on 40 of the 44 patients.

Figure 3.1, presents both the pre and post-ablation EDE strain and B-mode images for a patient with a 2 cm HCC diagnosed using pre-ablation magnetic resonance imaging. The liver was cirrhotic and the patient had not undergone any prior treatment for this tumor. HCC tumors are softer than normal liver tissue, and thus would be significantly softer than cirrhotic liver tissue [10]. Note the clear visualization of two MWA antennae in the B-mode image obtained prior to the ablation, as two antennae were placed for this patient. The pre-ablation EDE strain image indicates the presence of a small stiffer region surrounding the ablation needle, due to the cyro-lock feature utilized to prevent needle movement following antenna placement, and an area of increased decorrelation at the location of the second antenna. MWA ablation was performed for 5 minutes at a 65 Watt power level in this patient. The post-ablation EDE image indicates the ablated region as an ellipsoidal region of increased stiffness [11, 12] that incorporates the ablation region produced from both antennae. The needle track in the post-ablation images indicates the antenna that was perturbed to generate the EDE strain image in Figs. 3.1-3.3.

Ablation zones viewed on EDE were compared to those seen on conventional ultrasound B mode images in terms of ablation region area, contrast and CNR. The maximum dimension of the ablated region is outlined on Figs. 3.2 and 3.3, for both EDE and B-mode images, corresponding to the length of major axis of the low-strain region and the gas bubble cloud formed immediately after the ablation procedure. Note from Fig. 3.2, that the location of segment with the largest dimension in both images does not coincide, and this was the case with most of the ablations. Therefore, a more representative metric

such as the ablation area and strain contrast was utilized in our analysis. Also observe in Fig. 3.3 that the gas bubble region does not coincide with the ablated region.

Figures 3.4-3.7, summarize the different features utilized to compare the performance of EDE based strain imaging versus conventional B-mode imaging for evaluating the ablation zone following completion of the procedure. Scatter plots present measurements from all 40 patients, with a horizontal line denoting the mean of the EDE and B-mode measurements respectively. For the box-and-whisker plots the dashed long horizontal bar in each data sets represents the median value, with the first and third quartiles defined by the box while the error bar represents the 10% and 90% values of the distribution of the measured feature values.

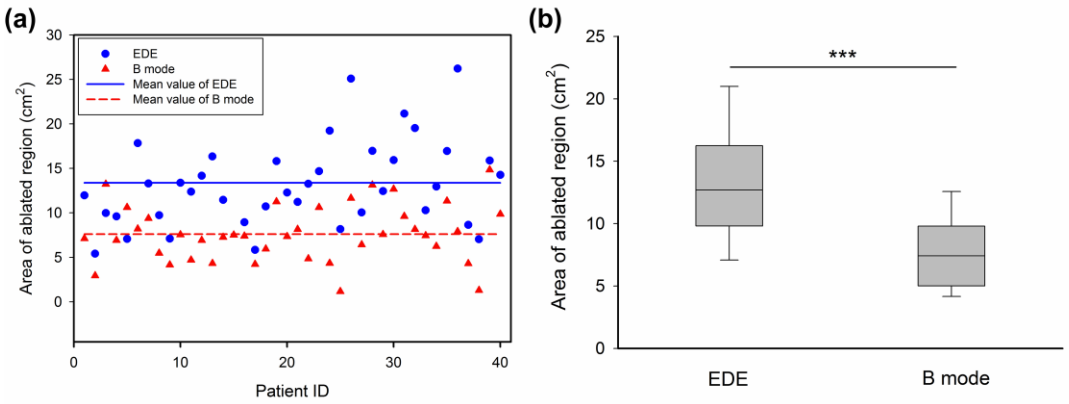

Fig. 3.4. Comparison of the ablation area measurements from B-mode (triangle) and EDE strain (circle) images, using scatter (a) and box and whisker plots (b). The mean value of the measurements is shown as the horizontal line in the scatter plot. For the box-and-whisker plot in (b), the dashed long horizontal bar in each data sets denotes the median value. The p value was <0.001 when comparing the mean values of EDE and corresponding B mode images, denoted by the three stars at the top.

3.3.1 Ablation region area on EDE and B mode images:

Figure 3.4(a), presents scatter plots comparing ablation areas estimated with EDE with areas of the hyperechoic regions on B-mode images. Each vertical pair of filled circles and triangles denotes values for EDE strain and B-mode respectively for the same patient. The average area of the ablation zone on EDE was 13.38 ± 4.99 (standard deviation) cm^2. As a comparison, the average area on B mode images for the same patient data set was 7.61 ± 3.21 (standard deviation) cm^2. A statistical comparison of the ablation area visualized on EDE strain with the area on B-mode imaging is illustrated in Fig. 3.4 (b).

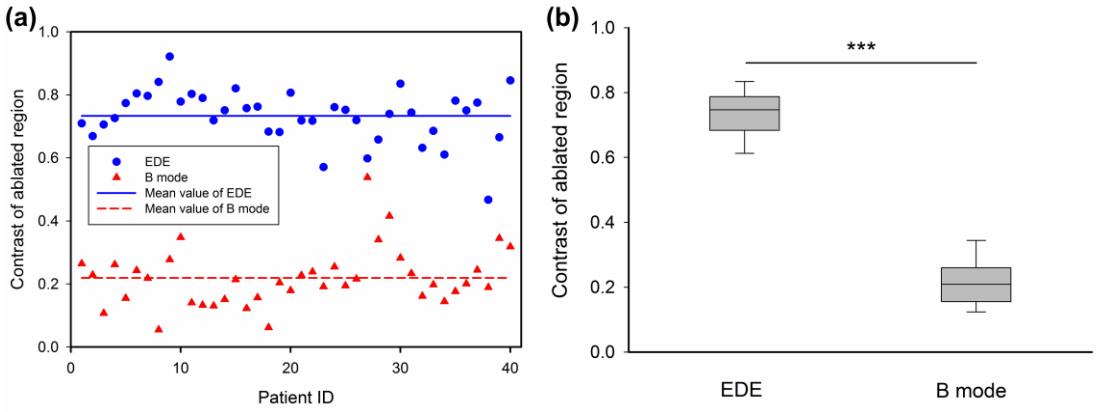

Fig. 3.5. Comparison of the ablation contrast measurements on B-mode (triangle) and EDE strain (circle) images, using scatter (a) and box and whisker plots (b).

3.3.2 Contrast of ablation region on EDE and B mode

In a similar manner, the distribution of the contrast obtained on the 40 patients is shown in Fig. 3.5(a). The mean value of the ablation zone contrast with EDE strain images was 0.73 ± 0.08 (standard deviation) while, the mean value of contrast on B mode images for the same patient data set was 0.22 ± 0.08 (standard deviation) as indicated by the

horizontal lines in Fig. 3.5(a). The scatter plot for the contrast indicates a significant separation between the contrast estimated for EDE and the B-mode contrast of the ablated region. The distribution of contrast between the ablation area and background is shown in Fig. 3.5 (b). Strain imaging appears to provide a significant improvement in ablation region delineation based on the contrast ($p < 0.001$).

3.3.3 CNR of the ablated region on EDE and B mode images

Finally, the CNR distribution for both EDE strain and B-mode imaging is illustrated in Fig. 3.6(a). The average CNR of the ablation zone on EDE was 10.94 ± 2.45 dB (standard deviation), while the average CNR on B mode images was 5.52 ± 3.37 dB (standard deviation). Observe that the CNR is always positive with EDE, while the CNR obtained with B-mode imaging shows a few cases with extremely poor CNR leading to reduced detectability of the ablated region. The box-and-whisker plots for the CNR for EDE strain and B-mode imaging is shown in Fig. 3.6 (b).

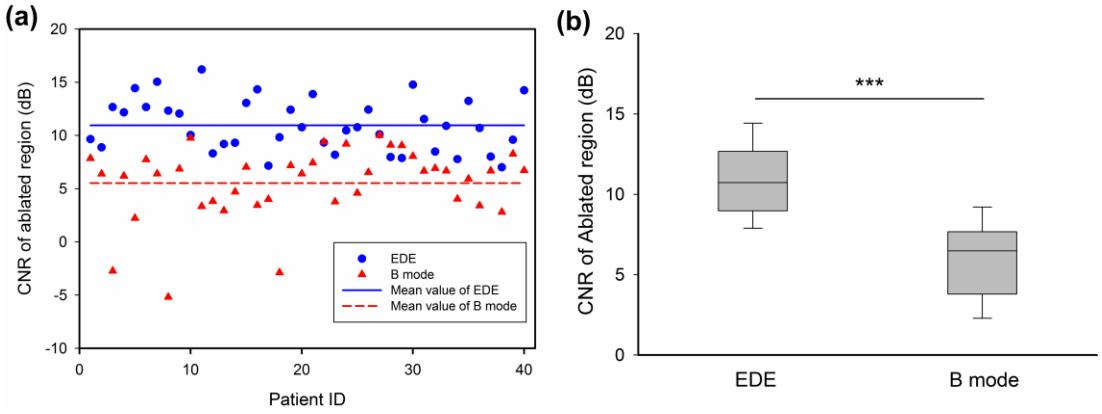

Fig. 3.6. Comparison of the CNR measurements on B-mode (triangle) and EDE strain (circle) images, using scatter (a) and box and whisker plots (b).

A two-dimensional scatter plot depicting contrast versus the ablation area for each patient is shown in Fig. 3.7. Observe the separation between the B-mode estimates for the 40 patients from the EDE estimates, which exhibit a higher contrast and larger ablation areas.

3.4 Discussion

EDE was applied on patients undergoing MWA therapy as a potential modality to define the post-procedure zone of ablation in this study. Strain images obtained using EDE demonstrated improved ablation region delineation when compared to conventional B mode images in terms of ablation area, image contrast and CNR as shown in Figs. 3.4-3.7. In addition, an approach that vibrates the ablation needle to generate and image shear waves, termed electrode vibration elastography has also been developed [13-16].

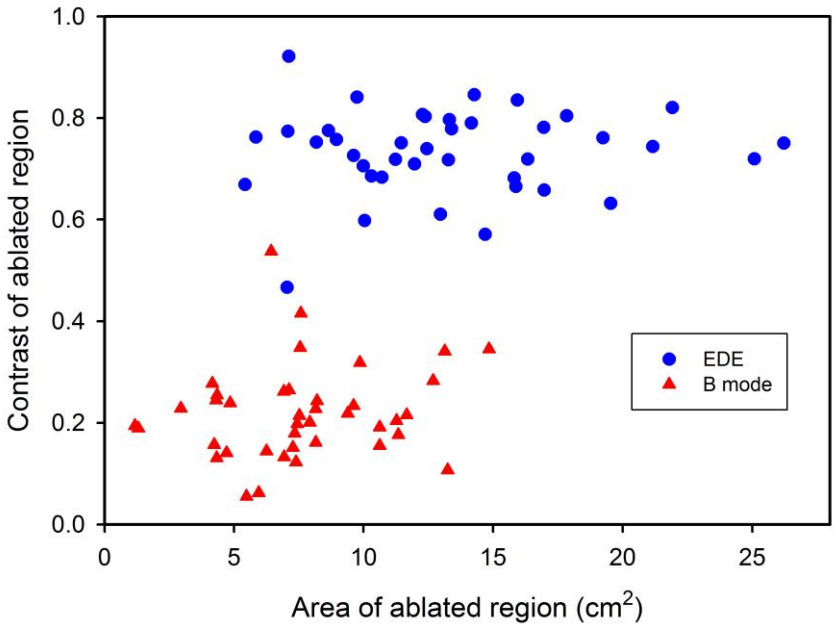

Fig. 3.7. Two-dimensional scatter plot showing ablation area versus contrast estimates for the ablated HCC tumors for B-mode (triangle) and EDE strain (circle). Observe the clustering of the B-mode and EDE data sets.

In conjunction with EDE, ultrasound could become an effective modality for complete monitoring of the ablation zone during MWA treatments. Although conventional B mode imaging is used routinely in the clinic for guidance in the ablation antenna/electrode placement and for monitoring outgassing, it does not clearly define the ablation zone at the completion of the procedure [17]. Currently the most common method to monitor the ablation margin at the completion of the procedure is X-ray computed tomography (CT). Contrast CT, the current clinical standard for confirmation of the success of the procedure, provides ablation zone volume estimation and margin definition. However, CT may not be available during the procedure in many centers. This may

necessitate a repeated ablation procedure and reinsertion of an antenna in the liver if the ablation zone does not adequately cover the targeted tumor and tissue margins. Ultrasound EDE is nonionizing, and thus can be performed without radiation exposure to either the patient or physician. The demographics of the patients involved in this study was 10 female and 34 male, ranging in age from 33 to 83, which is summarized in Table 3.1.

It is important when treating with RFA to limit variations in thermal dose within the ablation volume and to avoid delivery of an incomplete dose to tumors, including those that are adjacent to large vessels [18]. This limits the application of RFA to smaller tumors and ones away from large vessels (unless other precautions are taken). Large tumors and ones near large vessels show a decrease of up to 50% in terms of complete tumor necrosis [18]. An adequate ablation margin around the tumor region is a key factor for the success of percutaneous ablation treatments [18-20]. Various studies suggest that the margin should extend between 0.5 – 1.0 cm into the tumor free region [18-20]. Thus, an effective thermal ablation margin monitoring method is crucial to guarantee a successful clinical outcome. Immediately following ablation therapy, a hyperechoic area is observed on ultrasound B-mode images due to out-gassing of water vapor, which resolves within about 10 minutes after the procedure. The ablated region with MWA is slightly hyperechoic centrally and around the periphery and hypoechoic elsewhere [21, 22]. Contrast-enhanced ultrasound imaging has also been useful in delineating HCC tumors pre-ablation [23] and the coagulated region post-ablation [24]

Even in cases where ablation area estimations on B mode images were relatively close to those obtained on EDE strain, estimations of ablated areas on B mode images was always smaller due to a shadowing effect, as seen in Fig. 3.3. In Fig. 3.3 (b) the gas bubbles

tended to accumulate towards the top of the ablation zone and thus the lower boundary of the ablation zone was blurred due to the shadowing effect caused by increased attenuation from the gas bubbles. Thus, it was difficult to visualize the thermal dose distribution on the bottom half of the ablated region on B mode images, and this increases the uncertainty for physicians to judge if an adequate ablation margin has been applied uniformly around the ablation zone. On the other hand, as shown in Fig. 3.3 (a), the ablation zone could be clearly identified on EDE strain. Thus, the thermal dose distribution along any direction can be easily observed.

Based on the estimated ablation areas, EDE strain images were not significantly affected by tumor depth as illustrated in Table 3.2. EDE provides delineation of the ablated region for treated HCC regions both at shallow depths and for deeper ablated tumor regions. This result is unlike that reported for elastographic imaging using acoustic radiation force, which is generally limited by ultrasonic attenuation to depths lower than 8 cm [25, 26]

The major limitation of this study was the lack of real-time EDE imaging feedback to the physicians. Image processing was performed offline on an Intel Core 2 desktop computer. The average processing time for each EDE strain image was approximately one minute. In order to obtain real time feedback, a higher performance system or more efficient programming techniques would be necessary. This lack of real-time feedback also potentially affected the success rate of EDE strain imaging. We performed EDE on 44 patients and obtained successful strain imaging results in terms of distinguishable ablation zones on 40 of the 44 patients. Four patients were excluded from analysis as the ablation zone could not be clearly delineated due to insufficient compression or excessive signal decorrelation artifacts. The success rate was 90.9%, which would have been considerably

improved by the immediate feedback that real-time imaging would have provided to the physician [27]. Real-time feedback would allow physicians to more easily standardize the applied deformation using the ablation antenna. Several vendors currently do provide such feedback on their commercial elastography software, and this aspect can be easily addressed for this clinical application [27].

A second limitation of the study is the lack of ultrasound or EDE based volume information on the ablated region. We have previously demonstrated that three-dimensional volume reconstruction of ablated regions using EDE can be obtained [2], however a viable method of obtaining three-dimensional imaging information clinically in patients is essential. This can be done either with two-dimensional ultrasound arrays or more efficient scanning approaches [16].

The magnitude of the perturbation applied to the ablation antenna is within 1-2 mm. During the deformation of surrounding tissue and the ablated region, no relative slip between the surrounding tissue and ablation antenna was observed with EDE prior to or after the MWA procedure. There were no obvious side effects with EDE since the positioning of the ablation antenna was not affected after data acquisition. Because of the small range of displacements introduced by the antenna, the ablation procedure is not adversely affected [11, 28, 29].

3.5 Conclusion

In this chapter, we demonstrate that EDE is feasible during MWA procedures of HCC tumors regardless of tumor depth. EDE strain images provide improved ablation region delineation compared to conventional B mode imaging. Further work needs to be

performed to assess the accuracy of the ablation margin delineated by EDE and whether the entire tumor with sufficient surrounding normal tissue has been treated. Comparison of EDE results to a clinical gold standard such as contrast enhanced CT is therefore essential.

3.6 References

1. Varghese, T., J.A. Zagzebski, and F.T. Lee, Jr., *Elastographic imaging of thermal lesions in the liver in vivo following radiofrequency ablation: preliminary results.* Ultrasound Med Biol, 2002. **28**(11-12): p. 1467-73.

2. Bharat, S., et al., *Three-dimensional electrode displacement elastography using the Siemens C7F2 fourSight four-dimensional ultrasound transducer.* Ultrasound Med Biol, 2008. **34**(8): p. 1307-16.

3. Rubert, N., et al., *Electrode displacement strain imaging of thermally-ablated liver tissue in an in vivo animal model.* Med Phys, 2010. **37**(3): p. 1075-82.

4. Chen, H. and T. Varghese, *Multilevel hybrid 2D strain imaging algorithm for ultrasound sector/phased arrays.* Med Phys, 2009. **36**(6): p. 2098-106.

5. Chen, L., et al., *A quality-guided displacement tracking algorithm for ultrasonic elasticity imaging.* Med Image Anal, 2009. **13**(2): p. 286-96.

6. Xu, H., et al., *In vivo classification of breast masses using features derived from axial-strain and axial-shear images.* Ultrason Imaging, 2012. **34**(4): p. 222-36.

7. Varghese, T. and J. Ophir, *An analysis of elastographic contrast-to-noise ratio.* Ultrasound Med Biol, 1998. **24**(6): p. 915-24.

8. Bharat, S., et al., *Radio-frequency ablation electrode displacement elastography: a phantom study.* Med Phys, 2008. **35**(6): p. 2432-42.

9. Jiang, J., et al., *Ultrasound-based relative elastic modulus imaging for visualizing thermal ablation zones in a porcine model.* Phys Med Biol, 2010. **55**(8): p. 2281-306.

10. DeWall, R.J., et al., *Characterizing the compression-dependent viscoelastic properties of human hepatic pathologies using dynamic compression testing.* Phys Med Biol, 2012. **57**(8): p. 2273-86.

11. Kiss, M.Z., M.J. Daniels, and T. Varghese, *Investigation of temperature-dependent viscoelastic properties of thermal lesions in ex vivo animal liver tissue.* J Biomech, 2009. **42**(8): p. 959-66.

12. Bharat, S., et al., *Monitoring stiffness changes in lesions after radiofrequency ablation at different temperatures and durations of ablation.* Ultrasound Med Biol, 2005. **31**(3): p. 415-22.

13. Bharat, S. and T. Varghese, *Radiofrequency electrode vibration-induced shear wave imaging for tissue modulus estimation: A simulation study.* The Journal of the Acoustical Society of America, 2010. **128**(4): p. 1582-1585.

14. DeWall, R.J. and T. Varghese, *Improving thermal ablation delineation with electrode vibration elastography using a bidirectional wave propagation assumption.* IEEE Trans Ultrason Ferroelectr Freq Control, 2012. **59**(1): p. 168-73.

15. Dewall, R.J., T. Varghese, and C.L. Brace, *Visualizing ex vivo radiofrequency and microwave ablation zones using electrode vibration elastography.* Med Phys, 2012. **39**(11): p. 6692-700.

16. Ingle, A. and T. Varghese, *Three-dimensional sheaf of ultrasound planes reconstruction (SOUPR) of ablated volumes.* IEEE Trans Med Imaging, 2014. **33**(8): p. 1677-88.

17. Malone, D.E., et al., *Hepatic interstitial laser photocoagulation: demonstration and possible clinical importance of intravascular gas.* Radiology, 1994. **193**(1): p. 233-7.

18. Lencioni, R. and L. Crocetti, *Local-regional treatment of hepatocellular carcinoma.* Radiology, 2012. **262**(1): p. 43-58.

19. Lencioni, R. and L. Crocetti, *Radiofrequency ablation of liver cancer.* Tech Vasc Interv Radiol, 2007. **10**(1): p. 38-46.

20. Maluccio, M. and A. Covey, *Recent progress in understanding, diagnosing, and treating hepatocellular carcinoma.* CA Cancer J Clin, 2012. **62**(6): p. 394-9.

21. Wells, S.A., et al., *Liver Ablation: Best Practice.* Radiol Clin North Am, 2015. **53**(5): p. 933-71.

22. Ziemlewicz, T.J., et al., *Hepatic Tumor Ablation.* Surg Clin North Am, 2016. **96**(2): p. 315-39.

23. Minami, Y. and M. Kudo, *Review of dynamic contrast-enhanced ultrasound guidance in ablation therapy for hepatocellular carcinoma.* World J Gastroenterol, 2011. **17**(45): p. 4952-9.

24. Clevert, D.A., et al., *Image fusion in the management of thermal tumor ablation of the liver.* Clin Hemorheol Microcirc, 2012. **52**(2-4): p. 205-16.

25. Deng, Y., et al., *Analyzing the Impact of Increasing Mechanical Index and Energy Deposition on Shear Wave Speed Reconstruction in Human Liver.* Ultrasound in medicine & biology, 2015.

26. Zhao, H., et al., *Bias observed in time-of-flight shear wave speed measurements using radiation force of a focused ultrasound beam.* Ultrasound in medicine & biology, 2011. **37**(11): p. 1884-1892.

27. Hall, T.J., Y. Zhu, and C.S. Spalding, *In vivo real-time freehand palpation imaging.* Ultrasound Med Biol, 2003. **29**(3): p. 427-35.

28. Kolokythas, O., et al., *Ultrasound-based elastography: a novel approach to assess radio frequency ablation of liver masses performed with expandable ablation probes: a feasibility study.* J Ultrasound Med, 2008. **27**(6): p. 935-46.

29. Varghese, T., *Quasi-Static Ultrasound Elastography.* Ultrasound Clin, 2009. **4**(3): p. 323-338.

Chapter 4: Comparison of EDE and ARFI on patients with HCC and liver metastases

4.1 Introduction

In this chapter[1], we compare the MWA monitoring performance of EDE with a commercially implemented ultrasound elastography technique, referred to as Acoustic Radiation Force Impulse imaging (ARFI) [1]. ARFI produces stiffness images of local tissue by applying ultrasound push beams with acoustic intensities and durations significantly larger than diagnostic imaging to deform the local tissue, and then using beams with diagnostic intensity to analyze the local tissue displacement along the direction of the push beams. With the advantage of local compression using the push beams and decreased inter-operator variability, ARFI has been used for breast cancer detection [1] and RFA monitoring [2]. However, there lacks literature reports to the best of our knowledge on MWA monitoring using ARFI on liver neoplasms on a significant number of clinical cases.

[1]This chapter is adapted from **Yang W**, Varghese T, Ziemlewicz TJ, Alexander ML, Lubner MG, Hinshaw JL, Wells SA, Lee FT Jr. Delineation of post-procedure ablated region with electrode displacement elastography and acoustic radiation force impulse imaging. Ultrasound Med Biol. (Accepted April 20th, 2017)

We have previously reported that the ablated region is close to an ellipsoidal shape in EDE images with an enhanced signal, and contrast to noise ratios (SNR_e and CNR_e) when compared to conventional B-mode images [3]. In this study, we compare the delineation performance of EDE and ARFI on both tissue mimicking (TM) phantoms and a clinical application for monitoring MWA ablation procedures. Phantom inclusion dimensions, image contrast and CNR_e were compared for the phantom study, followed by a binary evaluation of the delineation of the ablated region for forty-nine patients with liver cancer in a clinical study.

4.2 Materials and Methods

4.2.1 TM phantom

Two TM phantoms previously constructed using an oil-in-gelatin matrix with a stiffer partially ablated inclusion (mimicking a partially ablated tumor) [4] were scanned using both ARFI and EDE. The centers of the inclusions in the two phantoms were located at depths of 3.5 and 5.5 cm, respectively. The Young's modulus contrast of the stiff ellipsoidal inclusion (mimicking the ablated region), irregular shaped target (mimicking tumor), and the background was 1.9:1.2:1, measured using a Supersonic Imagine (Supersonic, Aix-en-Provence, France) system. The three distinct regions can be distinguished on B mode images due to the different and distinct backscatter levels that were incorporated into the TM phantom manufacture as shown in Fig. 4.1(a) and (d). A stainless steel needle was bonded to the inclusion to mimic the MWA antenna.

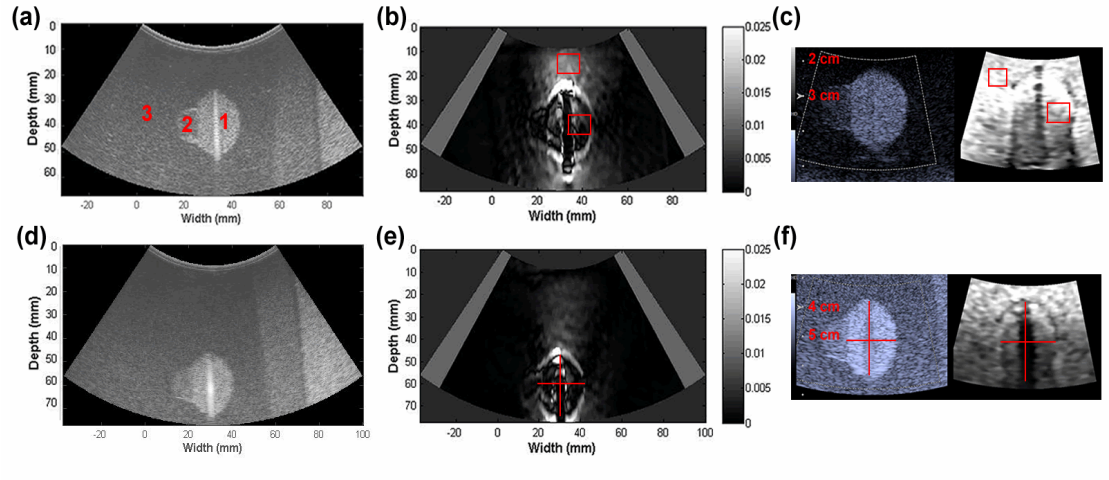

Fig. 4.1. B mode, EDE, and ARFI images of the corresponding TM phantoms. The first row (a-c) denotes the phantom with an inclusion at a 3.5 cm depth. The second row (d-f) denotes the phantom with a deeper inclusion at 5.5 cm. The three columns present B mode (reconstructed from RF data), EDE, and ARFI images for the two phantoms, respectively. The bright regions in the right side of (a) and (d) are caused by the phantom container due to the wide field of view of the curvilinear transducer. The gray area at the boarder of the sector images in (b) and (e) are dummy A-lines to preserve the original physical dimension. The numbers 1-3 in (a) denote the inclusion, irregular shaped target, and background, respectively. All images were acquired with a Siemens Acuson S2000 system and 6C1 HD transducer operating at a center frequency of 4 MHz. The colorbar of the EDE images indicates the strain caused by a manual deformation. (i.e. 0.01 corresponds to a 1% strain).

EDE and ARFI images of the TM phantom are shown in Fig. 4.1(b), (e), and (c), (f) respectively. Image contrast and contrast to noise ratio (CNR_e) were used to quantify the visibility of the inclusion on EDE and ARFI images. Two rectangular regions of interest

(ROI) with dimensions of 10×10 mm were placed inside and above the inclusion to calculate the image contrast and CNR_e using the following equations.

$$\text{Image contrast} = \left| \frac{I_b - I_o}{I_o + I_b} \right| \tag{4.1}$$

where I_b and I_o denote the mean pixel value of the ROI placed in the background and object (inclusion), respectively. For EDE images as shown in Fig. 4.1(b), one ROI was placed in the inclusion slightly off-center to reduce strain artifacts caused by the needle, and the other ROI was placed as close as possible to the inclusion above the saturated halo to avoid decorrelation tracking noise [5]. For ARFI images as shown in Fig. 4.1(c), the ROI inside the inclusion was placed similarly off-center of the inclusion, while the other ROI was placed in the upper background which was above the irregular shaped region. CNR_e was calculated using the following equation:

$$CNR_e = \frac{\left| I_o - I_b \right|}{\sqrt{\sigma_o^2 + \sigma_b^2}} \tag{4.2}$$

where I_b and I_o are the mean values as defined above, while σ_b and σ_o are the standard deviation of the ROI placed in background and object (inclusion), respectively. CNR_e denotes the detectability of the inclusion taking into account of the effect of noise.

Dimensions of the inclusion on EDE and ARFI images were used to compare the delineation accuracy between these two modalities. As shown in Fig. 4.1(e) and (f), the long and short axes of the inclusion were measured on EDE and ARFI images, respectively. For EDE images, these dimensions were measured on strain images as shown in Fig. 4.1(e),

while for ARFI and B mode images, they were measured using the built-in distance measurement function on the ultrasound system. The short axis of the inclusion was measured without the irregular shaped region because this region cannot be visualized on ARFI images as shown in Fig. 4.1(f). The contrast, CNR_e, and inclusion dimensions were all determined from ten independent experiments with EDE and ARFI, respectively.

4.2.2 Patients and MWA procedure

Forty-nine patients diagnosed with HCC, adenoma, or liver metastases, and treated with a MWA procedure were recruited into our study, with both EDE and ARFI imaging performed for each patient. This study was conducted under a protocol approved by the institutional review board (IRB) of the University of Wisconsin-Madison, with informed consent obtained for each patient. Patient demographics included 35 males and 14 female subjects, who ranged in age from 33 to 87. Detailed demographics of the patients recruited to this study are shown in Table 4.1.

Table 4.1. Patient statistics

Patient Demographics	**Value**
Age	33 -87 years (62.0 ± 11.9)
Gender (M/F)	35/14
Tumor type (HCC/adenoma/metastases)	37/2/10
Mean Tumor size	2.3 ± 0.9 cm
Cirrhosis (Y/N)	33/16
Fatty Liver (Y/N)	1/49
Prior Treatment (Y/N)	12/37

MWA was performed for patients under general anesthesia, with patients placed in a supine, lateral, or prone position on a CT imaging table, depending on the location of the liver tumors. MWA was performed using a Certus 140 system (Neuwave Medical Inc. Madison, WI). Single or multiple antennas were inserted based on the tumor dimensions and location, under ultrasound B-mode imaging guidance. Typical ablation power and duration was 65 W and 5 minutes, respectively.

4.2.3 EDE and ARFI data acquisition

Both ARFI and EDE studies were performed using a Siemens Acuson S2000 system (Siemens Medical Solutions Inc., Mountain View, CA USA) with a 6C1 HD curvilinear transducer. For the phantom study, EDE and ARFI images were acquired at an imaging depth of 6 and 7 cm, with a focus set at 3.5 or 5.5 cm, respectively for the two phantoms, using a center frequency of 4 MHz. ARFI images were obtained using "Virtual Touch" software and images were generated in real time. EDE strain images were obtained from a continuous loop of in-phase/ quadrature data acquired during manual perturbation of the ablation antenna, with the amplitude of 1 - 2 mm. EDE strain images were computed between 2 in-phase/ quadrature frames within the loop using a 2D cross-correlation algorithm [6]. These two frames of in-phase/ quadrature data were selected manually by observing the movement of the ablation region in the B-mode images. The cross-correlation kernel dimension was selected as 0.45 × 1.41 mm to generate strain images with high SNR [7, 8]. Since the A lines with curvilinear transducers are sparser towards the bottom of image the tracking and processing kernel width expands accordingly with depth [3].

For the clinical study, EDE and ARFI images were sequentially acquired immediately following the MWA procedure. Imaging depth was selected to span the entire ablated region, with the focus selected to lie slightly below the ablation zone to reduce shadowing from gas bubbles generated during the ablation procedure. ARFI and EDE image acquisition protocols were similar to that utilized for the phantom study and manual perturbation of the ablation needle was performed by a physician. The displacement of the MWA antenna was performed in a sinusoidal manner along the axis of the antenna by the clinician manually. Out of plane displacement of the antenna was minimized. For patients where multiple antennas were placed, only the central antenna was perturbed to obtain the EDE strain image. For patients with multiple tumors, only the first treated tumor was analyzed in this chapter to avoid artifacts caused by repositioning of the antennas. The 2D cross-correlation kernel dimension used for the clinical study was 1.35 × 3.29 mm which was larger than that used for the phantom study in order to include more echo signal to improve deformation tracking due to the increased attenuation present in clinical data sets [3, 7, 8]. The monitoring ability of EDE and ARFI was assessed based on whether a visible boundary could be delineated to differentiate the ablated zone from the surrounding untreated tissue. In some ARFI images, the location of ablated region could be reasonably recognized with reference of the B-mode images, even though they were depicted without a clear boundary. For these cases, the monitoring ability of ARFI is defined as recognizable, which is inferior to the definition of delineable. Image analysis and reporting of the success rate for monitoring MWA using EDE and ARFI was performed by two observers based on the criteria described above. The observers include a graduate student (observer 1) with

over four years of experience in the processing, visualization and analysis of strain images, and a physician (observer 2) with more than ten years of experience with MWA procedures.

4.3 Results

EDE and ARFI images of the TM phantoms are shown in Fig. 4.1 (b-c) and (e-f). The inclusion in the EDE images of the TM phantom was identified from the background by a saturated bright halo surrounding a low strain or darker region. In the ARFI images, the inclusions can be reasonably differentiated from the background by a dark boundary with a relatively increased noise level. The irregular shaped target marked by the number 2 as shown in Fig. 4.1 (a) could be identified in EDE images as shown in Fig. 4.1 (b) and (e), while it is not visible in ARFI images as shown in Figs. 4.1 (c) and (f).

Ten independent EDE and ARFI images were acquired for both TM phantoms. The image contrast and CNR_e of the phantom with the inclusion at 3.5 cm was 3.45 ± 0.68 and 2.82 ± 0.81, respectively, while the same quantities measured on ARFI images for the same phantom was 1.03 ± 0.13 and 0.62 ± 0.32, respectively. The image contrast and CNR_e for this phantom was 2 – 3 times higher with EDE when compared with ARFI images as shown in Fig. 4.2 (Phantom 1). For the phantom with the deeper inclusion at 5.5 cm, image contrast and CNR_e in EDE images was 3.91 ± 1.63 and 2.45 ± 1.02, respectively, while in ARFI images these two quantities were 1.00 ± 0.05 and 0.18 ± 0.11, respectively. The detectability of the inclusion with EDE is about 4 – 10 times higher than ARFI in the second phantom with a deeper inclusion, as shown in Fig. 4.2 (Phantom 2).

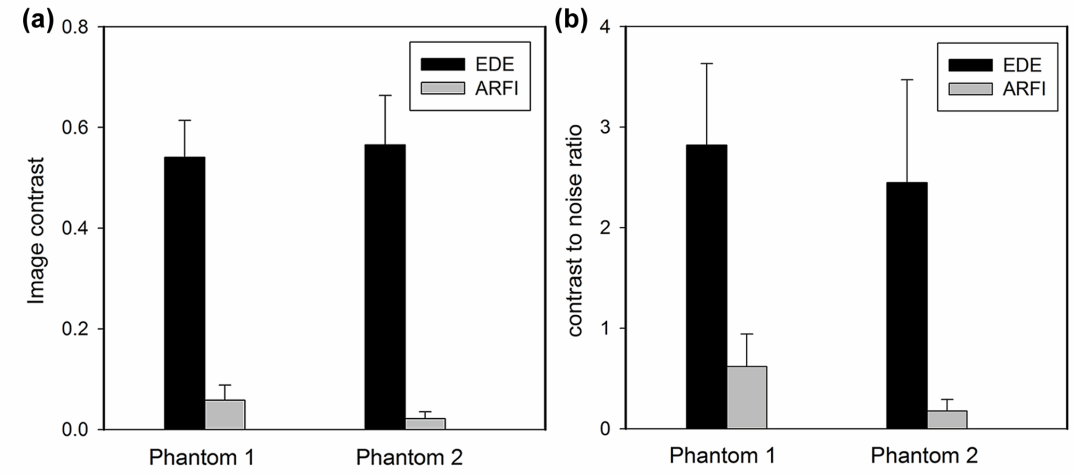

Fig. 4.2. Image contrast and CNR_e comparison obtained on EDE and ARFI images of TM phantoms. (a) Image contrast comparison of EDE and ARFI performed on the phantom with inclusion at a 3.5 cm depth (Phantom 1), and at a 5.5 cm depth (Phantom2) (b) Comparison of CNR_e on the same two phantoms. The height of the bars represents the mean value of 10 independent experiments and the error bar denotes the standard deviation of the measurements.

The delineation precision in terms of inclusion dimensions for 10 independent realizations for both EDE and ARFI images is shown in Fig. 4.3. The long axis (height) of the inclusion of Phantom 1 was 25.67 ± 0.49, 26.21 ± 0.92, and 27.86 ± 0.92 mm measured with B mode, EDE, and ARFI images, respectively, while the short axis (width) of this inclusion measured with these imaging modalities was 18.33 ± 0.26, 19.85 ± 0.20, and 19.83 ± 0.70 mm. For Phantom 2, the long axis of the inclusion measured with B mode, EDE, and ARFI was 25.86 ± 0.26, 26.41 ± 0.40, and 27.38 ± 0.39 mm, respectively, and the short axis measured with these three modalities was 19.43 ± 0.28, 20.70 ± 0.79, and

21.55 ± 0.35 mm, respectively. Differences in the inclusion dimensions measured with these three modalities were within 8% (2.2/25.67 ≈ 8%).

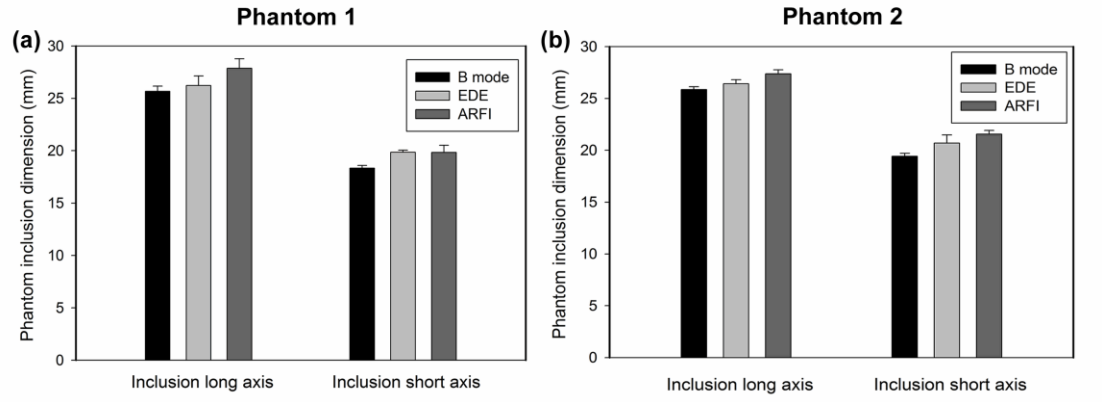

Fig. 4.3. Dimensions of phantom inclusion comparison among B mode, EDE, and ARFI images. (a) The long and short axes length of the phantom with inclusion at 3.5 cm (Phantom 1) measured in B mode, EDE, and ARFI images, (b) The same comparison conducted for phantom with inclusion at 5.5 cm (Phantom 2). The height of the bars represents the mean value of the 10 independent imaging experiments and the error bars denote the standard deviation.

For the clinical study, results from observer 1 indicate that the liver neoplasm targeted with the MWA procedure was successfully delineated with EDE for 45 out of the 49 patients. The ablated region could be delineated on 2 ARFI images, both presenting with tumors at depths of around 4 cm. The ablation zone with EDE was delineated by the dark region surrounded by a bright halo as illustrated in the TM phantom study. The boundary of the ablated region was relatively blurred in the ARFI images, as illustrated in Figs. 4.4 (a) and (c). The number of delineable ablation zone using ARFI images from

observer 2 was 6 out of 49 patients, with 4 of the tumors at a depth lower than 5 cm, 1 tumor was located between 5 and 10 cm, and 1 tumor with a depth of more than 10 cm. The number of delineated ablation zone from observer 2 was 34 with EDE.

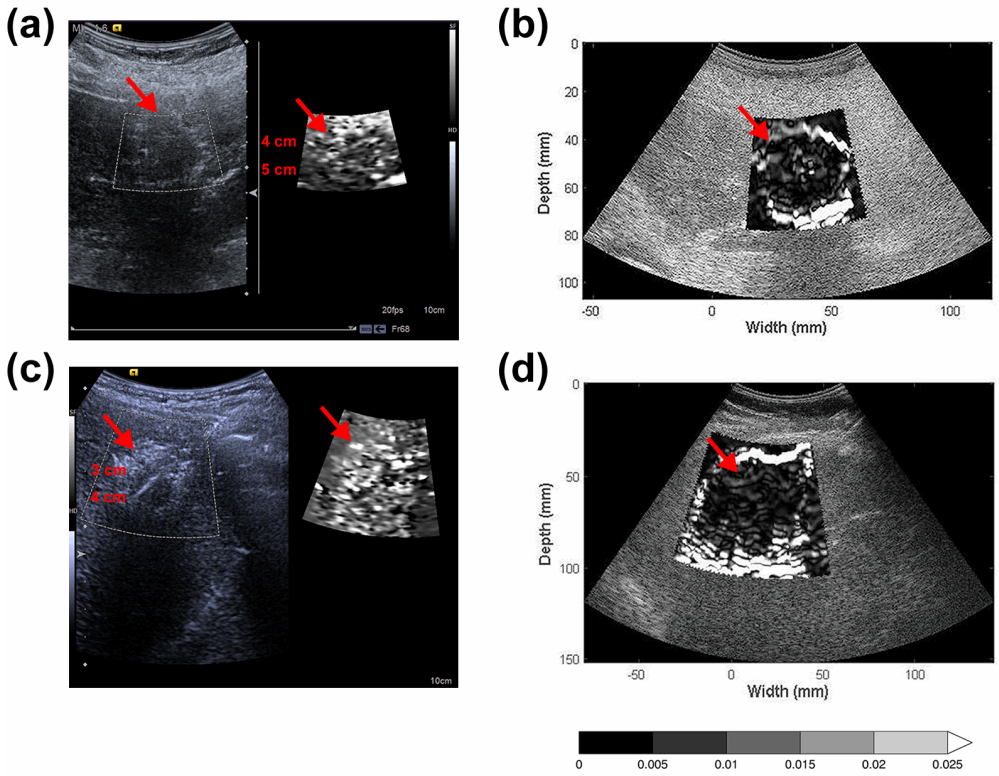

Fig. 4.4. Comparison of ARFI and EDE images immediately following MWA. The first column shows the B-mode and ARFI images of the ablated region. The second column shows EDE images generated from RF data. The ablated region is somewhat delineable in ARFI images (a) and (c).

For most of the 49 patients, the ablated region was not clearly delineable with a visible boundary as shown in Fig. 4.5 (a) and (c) for ARFI imaging. However, with reference to B-mode images the location of the ablated region could be recognized on 13 patients with the ARFI images as shown in Fig. 4.5 (d), from observer 1. The delineation

success rate of EDE and ARFI is summarized in Table 4.2. It was shown that the success rate decreased from 40% to 11.1% as the imaging depth increased from shallower, i.e. 5 cm to deeper than 10 cm. Partially visualized ablation regions were identified on 27 patients, by observer 2. The imaging depth dependence was similar to the results obtained by observer 1, dropping from 80% to 22.2% when the imaging depth increased from less than 5 cm to more than 10 cm as shown in Table 4.3.

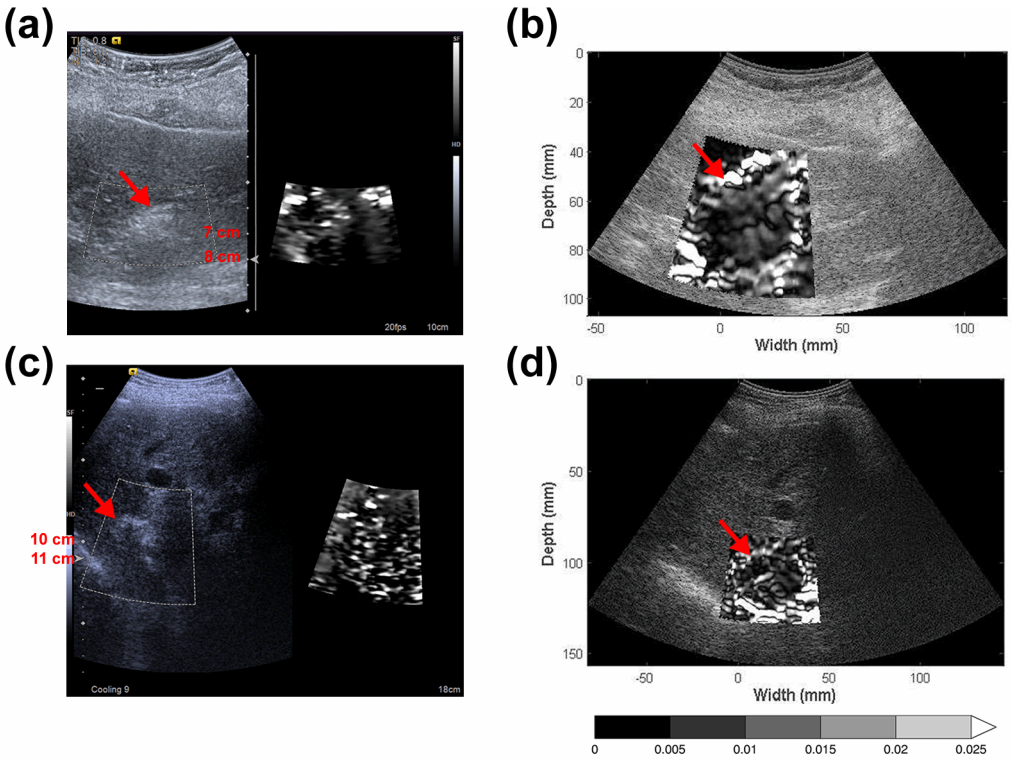

Fig. 4.5. Comparison of ARFI and EDE images immediately following MWA. The first column shows the B-mode and ARFI images of the ablated region. The second column shows the EDE images generated from RF data. The ablated region was not delineable in ARFI images (a) and (c), although with the reference of B mode image, the location of the ablated region is recognizable with a distorted shape in (c).

The total success rate with EDE for boundary delineation on the 49 patients was 91.8% and 69.4%, while that with ARFI was 4.1% and 12.2%, respectively for the two observers. EDE showed less imaging depth dependence with a relatively stable success rate for each depth range. The success rate with ARFI improved to 26.5% and 55.1%, respectively for the two observers, for partial visualization of the ablated region in conjunction with B-mode imaging. However, as the tumor depth increases the entire ablated region especially towards the bottom of the tumor was blurred. The number of delineable and partially visualized ablation regions from the two observers is shown in Fig. 4.6.

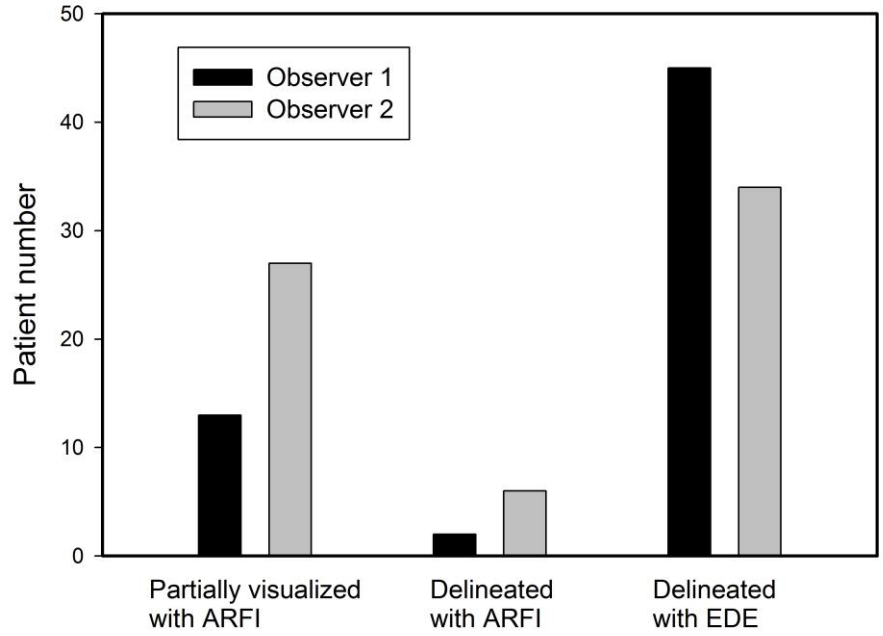

Fig. 4.6. Summary of the number of patient ablated regions delineated with ARFI and EDE respectively along with the number of ablated regions partially visualized in conjunction with B-mode and ARFI imaging. Partially visualized and delineable ablated regions with ARFI imaging were 13 and 2, respectively, from observer 1. The corresponding results from observer 2 were 27 and 6, respectively. The number of delineable ablation regions with EDE images was 45 and 34, respectively from observer 1 and 2.

Table 4.2. Summary of Patient Imaging results with both EDE and ARFI by the first observer

Tumor Depth	**Number of Patients**	**Partially Visualized on ARFI**	**Ablated Region Delineated with ARFI**	**Ablated Region Delineated with EDE**
< 5 cm	15	6/15 (40%)	2/15 (13.3%)	15/15 (100%)
> 5 cm < 10 cm	25	6/25 (24%)	0/25	21/25 (84%)
> 10 cm	9	1/9 (11.1%)	0/9	9/9 (100%)
Total	49	13/49 (26.5%)	2/49 (4.1%)	45/49 (91.8%)

Table 4.3. Summary of Patient Imaging results with both EDE and ARFI by the second observer

Tumor Depth	**Number of Patients**	**Partially Visualized with ARFI**	**Ablated Region Delineated with ARFI**	**Ablated Region Delineated with EDE**
< 5 cm	15	12/15 (80%)	4/15 (26.7%)	9/15 (60%)
> 5 cm < 10 cm	25	13/25 (52%)	1/25 (4%)	19/25 (76%)
> 10 cm	9	2/9 (22.2%)	1/9 (11.1%)	6/9 (66.7%)
Total	49	27/49 (55.1%)	6/49 (12.2%)	34/49 (69.4%)

4.4 Discussion and Conclusions

In this chapter, we compared the performance of EDE and ARFI for monitoring minimally invasive MWA treatments for liver neoplasms in human patients along with a

TM phantom study. The ARFI relative stiffness map reported in this chapter is based on the commercial software available on the Siemens Acuson S2000 system.

The TM phantom study showed that both ARFI and EDE reasonably delineate a stiffer inclusion embedded in a homogeneous background. The dimensions of the inclusion in the EDE and ARFI images were in a similar range within 8% difference, although the long and short axes appeared slightly larger on ARFI images. The detectability of the inclusion was enhanced in EDE images with a 2 – 3 times higher image contrast and CNR_e, and with less imaging depth dependence between the two phantoms evaluated. As shown in Fig. 4.3, the image contrast and CNR_e are similar in EDE images between the two phantoms, while the image contrast and CNR_e was lower in the ARFI images of the phantom with a deeper inclusion (Phantom2). Stiffness contrast [9], which denotes the ratio of the strain between the background and the target, is widely used as a metric to evaluate the contrast achieved with ultrasound elastography. However, for the analysis in this chapter we only have access to the final ARFI relative stiffness map without actual data values from the Siemens Acuson S2000 system. We therefore used the image contrast as defined in Equation (4.1), to avoid the denominator becoming too small and introducing numerical instability. Image processing to enhance the image contrast for the EDE strain images was not performed in this study.

The delineation rate obtained with EDE was significantly higher in the clinical studies when compared to ARFI. An important factor is that the displacement of local tissue perturbed with EDE occurs with larger amplitudes in the millimeter range, when compared to the amplitude of ARFI deformation in the range of sub-millimeters [1]. Insufficient displacement of local tissue with ARFI is mainly due to the increased attenuation incurred

by the push beams for larger depths [10]. The relatively deep location of the ablation zone, presence of cirrhotic livers, and gas bubbles generated by the ablation procedure contribute to the high attenuation incurred by the push beams [11]. The delineable ablated regions in ARFI images in this study were within 5 cm, which is consistent with previous *ex-vivo* [1, 12] and *in-vivo* studies [13] For ARFI monitoring of MWA procedures in the chapter, the ablation zone is stabilized by the antenna. Since the displacement of local tissue is caused by external pushing beams with ARFI, the amplitude of the displacement may have been further suppressed. Although the numbers of delineable cases from the two observers were different for EDE and ARFI, note that both observers indicate that a significant number of delineable cases are obtained with EDE.

The ARFI technique reported in this chapter was based on utilization of the commercial software, 'Virtual Touch', on the Siemens Acuson S2000 system. Although ARFI was initially developed for superficial and small masses such as breast cancer at early stages [1], methods to improve the monitoring ability of thermal ablation for larger masses and deeper locations have been reported [2]. In Fahey's study, ARFI was processed off-line with sophisticated tracking algorithms and filters for monitoring RFA procedures. Time-gain control was also applied to compensate for the varying radiation force magnitude due to attenuation and focal effects [2]. The tumor depth for the six patients in Fahey's study was mostly in the 5 – 6 cm range. Delineable boundaries were achieved for most of the six patients. Performance of ARFI with improved techniques at deeper locations and application to MWA requires further investigation.

In addition to the ARFI processing techniques discussed above, techniques enhancing the perturbation amplitude might also be helpful to improve the performance of

ARFI for monitoring thermal ablation. In Sarvazyan's study, an optimized waveform for the push beams was simulated to form a saw tooth wave in the focal zone to enhance the spatial energy density delivered to the local tissue [14]. The generation of this optimal wave form is depth dependent and varies for each patient. FDA standards for clinical ultrasound output is another limiting factor for the intensity of the push beam with ARFI, although the standards might be conservative for the short bursts of push beams utilized [1].

The delineation rate of ablation regions with EDE showed less dependence on imaging depth, due to the fact that the deformation of local tissue is delivered to the center of the ablation zone by the ablation needle. With less limitation on the perturbation amplitude, processing for EDE could be performed using a relatively compact two-dimensional cross correlation based algorithm. The processing time for EDE was about two minutes on an Intel Core 2 desktop using MATLAB (MathWorks, Natick, MA, USA), with the pre and post compression frames selected by an experienced operator. An algorithm for automatic selection of the pre and post compression frames will be implemented as part of future work. For clinical monitoring, real-time feedback to the clinician is essential and could significantly improve strain image quality. Since there are no specific parameter optimizations needed for different patients with EDE, the computational time could be significantly improved with faster software implementation on commercial systems for real-time imaging.

Based on the TM phantom and patient studies reported in this chapter, the imaging performance for monitoring MWA with EDE and ARFI were compared. Due to the limited number of delineable ablation regions in ARFI images, the patient study was designed as a binary evaluation. A quantitative analysis of EDE and B-mode image assessments was

performed in our previous chapter [3] The performance of commercial ARFI software, 'Virtual Touch' imaging, could be improved with more advanced processing techniques or advanced push beam profile design as discussed above. However, the overall monitoring ability for MWA with ARFI is limited due to the relatively small perturbation amplitudes produced with radiation force, increased attenuation in cirrhotic livers and the larger depth range needed for ablation procedures. EDE with its advantage of not being significantly dependent on the tumor depth, stable perturbation amplitudes at all depths and relatively straightforward real-time implementation for commercial systems, could be an alternative technique to monitor minimally invasive MWA during ablation procedures.

4.5 References

1. Nightingale, K.R., et al., *On the feasibility of remote palpation using acoustic radiation force.* J Acoust Soc Am, 2001. **110**(1): p. 625-34.

2. Fahey, B.J., et al., *In vivo guidance and assessment of liver radio-frequency ablation with acoustic radiation force elastography.* Ultrasound Med Biol, 2008. **34**(10): p. 1590-603.

3. Yang, W., et al., *Post-procedure Evaluation of Microwave Ablations of Hepatocellular Carcinomas Using Electrode Displacement Elastography.* Ultrasound in Medicine & Biology, 2016.

4. Ingle, A. and T. Varghese, *Three-dimensional sheaf of ultrasound planes reconstruction (SOUPR) of ablated volumes.* IEEE Trans Med Imaging, 2014. **33**(8): p. 1677-88.

5. Bharat, S., et al., *Radio-frequency ablation electrode displacement elastography: a phantom study.* Med Phys, 2008. **35**(6): p. 2432-42.

6. Chen, L., et al., *A quality-guided displacement tracking algorithm for ultrasonic elasticity imaging.* Med Image Anal, 2009. **13**(2): p. 286-96.

7. Varghese, T. and J. Ophir, *A theoretical framework for performance characterization of elastography: the strain filter.* IEEE Trans Ultrason Ferroelectr Freq Control, 1997. **44**(1): p. 164-72.

8. Varghese, T., *Quasi-Static Ultrasound Elastography.* Ultrasound Clin, 2009. **4**(3): p. 323-338.

9. Varghese, T. and J. Ophir, *A theoretical framework for performance characterization of elastography: The strain filter.* IEEE Transactions on Ultrasonics, Ferroelectrics, and Frequency Control, 1997. **44**(1): p. 164-172.

10. Correa-Gallego, C., et al., *Intraoperative ultrasound and tissue elastography measurements do not predict the size of hepatic microwave ablations.* Academic radiology, 2014. **21**(1): p. 72-78.

11. Varghese, T., et al., *Impact of gas bubbles generated during interstitial ablation on elastographic depiction of in vitro thermal lesions.* J Ultrasound Med, 2004. **23**(4): p. 535-44; quiz 545-6.

12. Bing, K.F., et al., *Combined ultrasonic thermal ablation with interleaved ARFI image monitoring using a single diagnostic curvilinear array: a feasibility study.* Ultrason Imaging, 2011. **33**(4): p. 217-32.

13. Mariani, A., et al., *Real time shear waves elastography monitoring of thermal ablation: in vivo evaluation in pig livers.* J Surg Res, 2014. **188**(1): p. 37-43.

14. Sarvazyan, A.P., et al., *Shear wave elasticity imaging: a new ultrasonic technology of medical diagnostics.* Ultrasound Med Biol, 1998. **24**(9): p. 1419-35.

Chapter 5: Three-dimensional reconstruction of ultrasound elastography[1]

5.1 Introduction

Ultrasound elastography is based on analyzing sequential ultrasound radiofrequency echo-signal frames in response to an internal [1-4] or external [5-7] mechanical stimulus. Local tissue strain [5], shear wave velocity [8] or wavelength [9] are commonly used as parameters to estimate the Young's modulus of the local tissue. In this study, we focus on evaluating three-dimensional (3D) strain imaging for ablation monitoring to overcome limitations of current 2D ultrasound elastography. Due to the 1D nature of most ultrasound transducers, almost all of current ultrasound elastographic imaging in use is confined to 2D imaging planes. The lack of out of plane tissue stiffness limits information on tumor volumes and reduces ablation region monitoring to a single slice intersecting the 3D treated volume. It could result in an inaccurate estimate of the tumor size or thermal dose delivered because the tumor or ablated region may have a different shape on other intersecting imaging planes.

[1]This chapter is adapted from **Yang W**, Ingle A, Varghese T. Comparison of three dimensional strain volume reconstructions using SOUPR and wobbler based acquisitions: A phantom study. Med Phys. 2016;43(4):1615-26. doi: 10.1118/1.4942814. PubMed PMID: 27036561; PubMed Central PMCID: PMC4788604.

To obtain the entire 3D distribution of tissue stiffness, 3D elastography has been utilized including its application with free-hand 1D transducer scans [10, 11] or wobbler transducer [12, 13] based acquisitions. 3D reconstruction using free-hand transducer scanning is based on transducer position tracking and 3D coordinate interpolation [10, 11]. With a 1D transducer placed on the surface of a patient, laser/optical/acoustic tracking systems are used to record the relative position of the transducer. After a series of scans, 2D strain, modulus or shear wave elastograms and their position information are input into the 3D coordinate system and an interpolated 3D elastogram is generated. The advantage of this type of 3D elastography is the flexible positioning of the transducer. Nevertheless, position tracking always introduces errors and it is relatively difficult to record the tilt angle of each imaging plane, and the final interpolation results may be biased by imprecise 2D imaging plane coordinates.

An alternative 3D ultrasound elastography approach is based on using a mechanically driven 'wobbler' transducer [12, 14]. The wobbler transducer is an encapsulated 1D transducer whose translational movement can be controlled by a mechanical driver. It provides more accurate imaging position information than free-hand 1D transducer acquisitions. 3D elastographic imaging with wobbler transducers can be categorized into two types: in one, the target 3D volume image is interpolated from the discrete 2D imaging planes, and a volume before and after the tissue deformation is recorded with local displacement and strain values calculated based on the volumetric data acquired. However, the computational complexity of volume-based algorithms is relatively steep, and thus the local tissue displacement search range is usually confined in a small range [14]. The other type is based on the interpolation of 2D strain images obtained at each mechanical position of the transducer in a step and shoot mode [12, 13]. A series of quasi-parallel 2D strain images are generated at each position of the wobbler transducer, and are then interpolated

to generate a 3D volume based on their position. The reconstruction algorithm is similar to that used for free-hand 1D transducer based acquisitions, except that the imaging planes are better controlled.

In spite of the relatively accurate position information obtained with a wobbler transducer, there may be mismatches between the quasi-parallel imaging planes and a spherical or ellipsoidal region mimicking a tumor or ablated region. These quasi-parallel 2D imaging planes may intersect with the ellipsoidal regions enclosing only a small area near the target boundaries. Thus, the effective information in each 2D plane decreases as the imaging planes move from the center to target edges. The lack of effective strain information on these imaging planes towards the edges and the resulting interpolation may lead to distortion of the target shape and inaccurate estimation of the target volume. In order to overcome the mismatch of the imaging planes and the ellipsoid target shape, we introduced a rotational acquisition method for 3D US elastography in a previous study, referred to as Sheaf of Ultrasound Planes Reconstruction (SOUPR) [15]. Instead of linearly translating the US transducer along the target surface, the acquisition planes are positioned rotationally with a specified angular increment. The sheaf of imaging planes is rotated along the central axis of the spherical or ellipsoid target. As a result, the strain information is maximized in each of the 2D imaging planes.

In this chapter, we experimentally evaluate and compare SOUPR-based acquisitions and 3D volume reconstruction to that obtained using a wobbler transducer on a tissue mimicking (TM) phantom with an ellipsoidal inclusion mimicking a tumor or ablated region. 2D strain images generated with 8 different cross-correlation kernel sizes at each SOUPR and wobbler imaging plane were utilized for 3D volume reconstruction. The reconstructed inclusion dimensions, volume, signal to noise ratio (SNRe), and contrast to noise ratio (CNRe) of the SOUPR and wobbler

acquisitions were compared. 3D reconstruction was further tested on a thermal ablation created in *ex-vivo* bovine liver tissue.

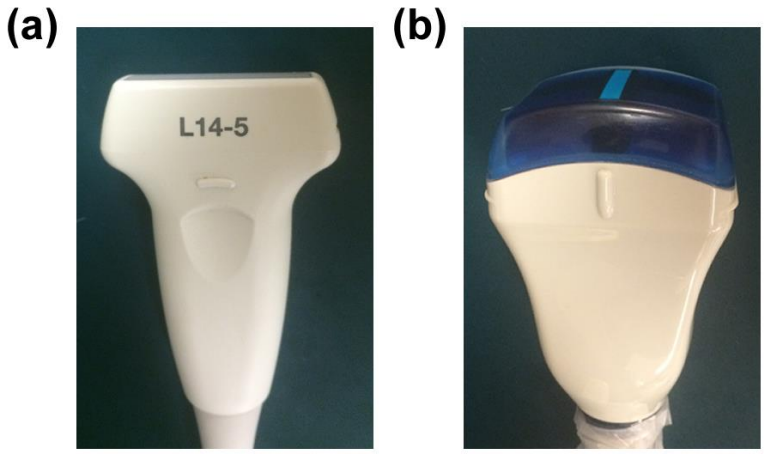

Fig. 5.1. Ultrasound transducers used for SOUPR and Wobbler 3D reconstruction. (a) The L14-5/38 linear transducer used for SOUPR. (b) The 4DL14-5/38 transducer used for Wobbler transducer reconstruction. The linear array transducer inside the Wobbler transducer is identical to the linear transducer used for SOUPR.

5.2 Materials and Methods

5.2.1 Experimental setup

3D strain image reconstructions using SOUPR and wobbler were performed on ultrasound radiofrequency (RF) data acquired on a cubical TM phantom with an ellipsoidal inclusion placed at a depth of 3.5 cm. RF data for SOUPR was acquired using the research mode in the Ultrasonix SonicTOUCH system. In a similar manner RF data using the wobbler transducer were acquired using driver software developed using the software development kit (SDK) on the Ultrasonix system. The dimension of the TM phantom was 80×80×80 mm. The major axis of the embedded

ellipsoid was 19 mm and the other two minor axes were both 14 mm. The shear modulus ratio of the inclusion to background was 2.9, measured using an Aixplorer system (Supersonic Imagine Corporation, France), with a similar sized region at the same depth.

An Ultrasonix SonixTOUCH system (Analogic Corporation, MA, USA) was used to acquire US RF echo signals. The transducer utilized for SOUPR was a L14-5/38 linear array transducer, as shown in Fig. 5.1(a), and a 4D L14-5/38 transducer was used for the wobbler based acquisition as shown in Fig. 5.1(b). The linear array transducer encapsulated in the wobbler was identical to the L14-5/38 transducer used for SOUPR. The imaging planes for SOUPR were perpendicular to the phantom surface and rotated around the central axis of the inclusion at a 30° angle as illustrated in Fig. 5.2(a). Mechanical translation of the linear transducer inside the wobbler was approximated by a series of quasi-parallel planes with 2.02 mm intervals, which were calculated from the stepping angle and the source to target distance as shown in Fig. 5.2(b). There was a 1° divergence between these imaging planes because of the small angular rotation of the linear array wobbler transducer, which was approximated by the translation. This divergence correction is discussed in section 5.2.C. Ten independent data acquisition experiments were performed on the TM phantom for the two 3D reconstruction methods. A total of 6 imaging planes were used for each 3D SOUPR reconstruction, while the number of imaging planes for the wobbler transducer that intersect the inclusion was between 7 to 8 planes for the 10 independent acquisitions. For both SOUPR and wobbler acquisitions, the transducers were operated at a 6.7 MHz center frequency, using an image depth of 6 cm with a single focal zone located at 4 cm. The imaging width of both SOUPR and the wobbler transducer was both 38 mm. RF echo signals were acquired at a 40 MHz sampling frequency. The L14-5/38 and 4D L14-5/38 transducers were inserted into a 10×10 cm plexiglass plate to apply a uniform mechanical deformation as shown in

Fig. 5.2(c). A 1.6 mm compression [16] was applied along the vertical direction, which is 2% of the phantom height of 80 mm. The compression ratio is within the linear stress-strain range of the material due to the small compression.

5.2.2 2D Strain image generation and segmentation

A 2D cross-correlation based tracking algorithm[17] was implemented to estimate the local displacement in the TM phantom caused by the external compression for both SOUPR and wobbler acquisition methods. Eight different window dimensions based on a combination of 4 different axial lengths and 2 lateral widths were used to compare the reconstruction results in terms of the inclusion volume, SNRe, CNRe and ellipsoidal axis lengths. Axial dimensions of the tracking kernels were 3.4, 4.8, 6.1 and 7.5 wavelengths and the lateral widths were 3 and 7 A-lines, respectively. The two adjacent cross correlation kernels overlap 80% along the beam direction and an A-line in the lateral direction.

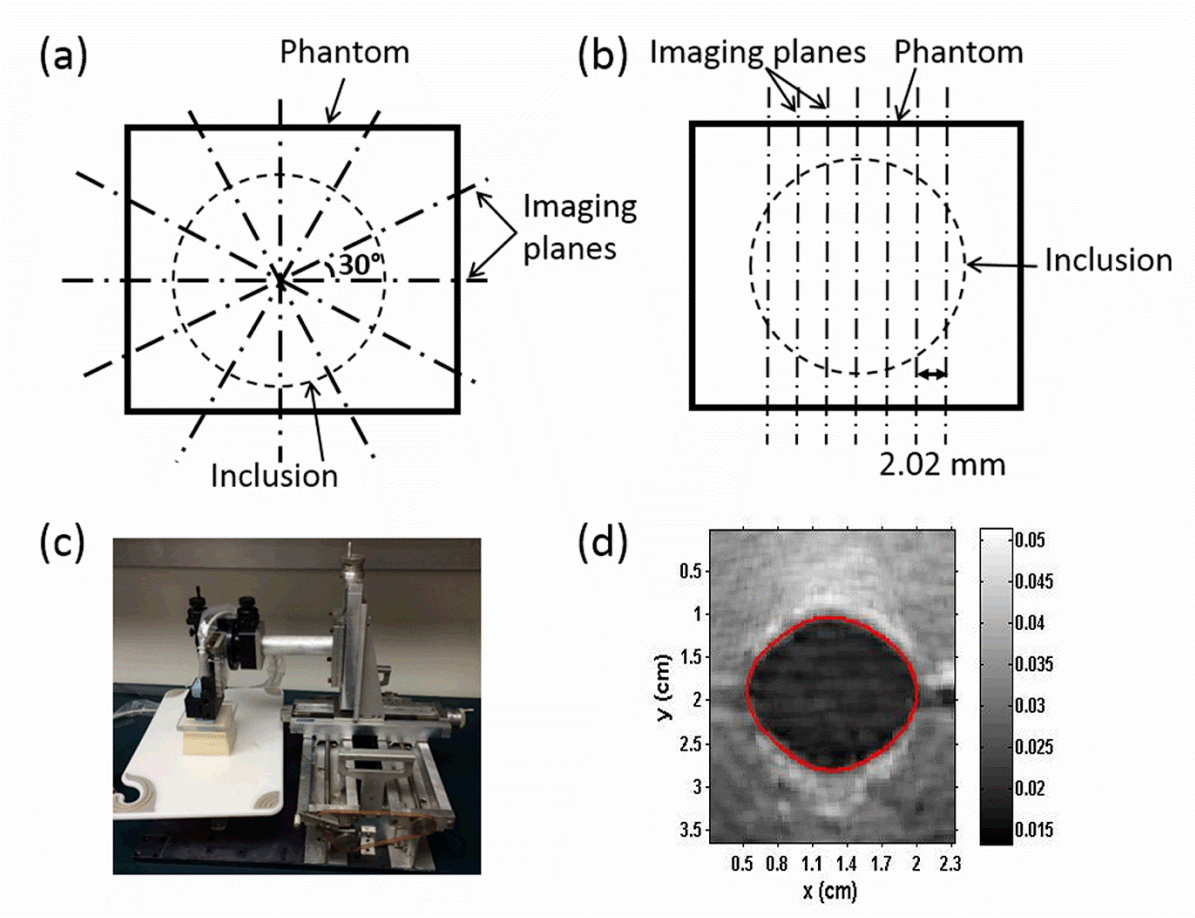

Fig. 5.2. Experimental setup and 2D ultrasound imaging plane geometry. Top view of 2D US scan plane geometry for (a) SOUPR and (b) wobbler based reconstruction. (c) The compression apparatus and TM phantom. (d) 2D strain image generated with cross-correlation kernel size of 4.8 wavelength × 7 A-lines. The red contour denotes segmentation results using an active contour algorithm.

Strain values were calculated as the gradient of local displacement. A 15-point linear least square fit was applied to reduce noise artifacts caused by the gradient calculation. Stiffer regions experience less strain and thus appear as dark regions in the strain image as shown in Fig. 5.2(d).

Only the axial component of the strain was estimated because the deformation was applied uniformly along the axial or beam direction.

In order to define the boundary of the inclusion, segmentation was applied to the 2D strain images. An ‘active contour’ algorithm [18] was used for segmentation with the results shown in Fig. 5.2(d). An initial circular contour was placed at the center of the inclusion. It was found that 600 iterations were sufficient to converge to a reasonable solution. The final contours were expanded with a disk kernel of 7 pixels in diameter to close the gaps of segmented contours caused by noise in strain images and then shrunk by the same kernel to delineate a sharp edge. The segmentation algorithm was applied to the strain images generated with the 8 different windows for both SOUPR and wobbler based acquisitions. 2D binary masks were generated based on these segmentation results with a value of 1 inside the inclusion and a value of 0 in the background. Volume estimation of the 3D reconstructed inclusion was based on these binary masks as discussed in the following section.

5.2.3 3D strain volume and binary mask reconstruction

3D strain volume estimation of the inclusion was divided into 2 parts: the first stage was the reconstruction of a 3D strain image from the 2D imaging planes, while the second stage was the generation of a 3D binary mask. The purpose of the binary mask was for the semi-automated estimation of the inclusion volume to eliminate any observer errors in delineating inclusion boundaries on the 3D strain image. On the other hand, SNRe and CNRe were measured on the 3D strain image to compare the detectability of the reconstructed inclusion using the SOUPR and wobbler acquisition methods.

For SOUPR, a 3D binary mask of the inclusion was reconstructed with the 2D segmented binary masks as discussed in 2. B. using a reconstruction algorithm developed by our group[15], which is described in Equation (5.1).

$$\min_{x} \left\| Ax - b \right\|^2 + \eta \left\| Bx \right\|^2 \tag{5.1}$$

where x denotes the 3D volume to be estimated; A is the grid sampling matrix; b is the observed value located in the sheaf of planes; $\eta > 0$ is a regularization parameter that controls the amount of smoothing; and B represents the Laplacian operator calculating the second derivative of the 3D volume as an indicator of the smoothness.

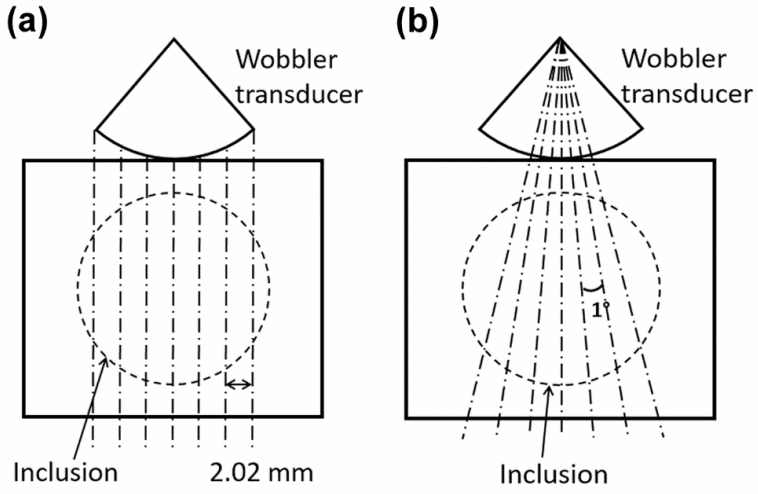

Fig. 5.3. Wobbler transducer imaging plane step angle correction. (a) Lateral view of the imaging plane of the wobbler transducer assuming that they are parallel. (b) Lateral view of imaging plane after angle correction with the 2D projective transform applied to the lateral slices.

The reconstruction was formulated as an optimization problem on a user defined 3D coordinate system with known data sampled at specific planes as shown in Fig. 5.2(a). The interpolation was subject to an optimization process with an objective function shown in Equation (5.1) consisting of preserving data consistency with the known data at those 2D imaging planes and a data smoothness constraint. Data consistency is aimed at keeping the reconstructed 3D strain or binary mask to be within a small variation from the known data measured at those 2D planes, and the data smoothness constraint was based on the assumption that the inclusion possessed a smooth ellipsoidal shape, which is common for thermal lesion [15]. The solution to this optimization problem and tuning of the regularization parameter η was described in detail in the paper by Ingle and Varghese [15]. A reconstructed 3D binary mask was used for inclusion volume estimation which is discussed in 2. D. The 3D strain images were reconstructed with the same algorithm except that they were reconstructed directly from the 2D strain images without segmentation. The SNRe and CNRe were calculated on these 3D strain images, as discussed in the following section.

For the reconstruction with the wobbler transducer, 3D binary masks and strain images were reconstructed with a conventional bicubic interpolation to assemble the 2D binary masks and strain images to create a 3D volume. The 2D images were first interpolated with an assumption that the imaging planes were parallel, as shown in Fig. 5.2(b) and Fig. 5.3(a). Then a projective transformation [19] was applied to the 3D coordinate system to project the reconstructed 3D cube into a trapezoid to account for the 1° divergence of the imaging planes which was induced by the step angle of the wobbler transducer as shown in Fig. 5.3(b). The projective transformation was applied to each lateral plane of the 3D interpolated volume. Thus, the original square plane was

transformed to a trapezoid with a shrunken top and an expanded bottom region. The projection transform is formulated in Equation (5.2):

$$P_s = M_{ds} P_d \tag{5.2}$$

where $P_s = \begin{pmatrix} u \\ v \\ q \end{pmatrix}$ is the coordinate of points before transformation and $P_d = \begin{pmatrix} x \\ y \\ w \end{pmatrix}$ is the coordinate of points after transformation. The effective coordinate of the points is the first 2 dimensions and the third dimension is added to account for scaling. $M_{ds} = \begin{pmatrix} a & b & c \\ d & e & f \\ g & h & i \end{pmatrix}$ is the projection matrix, and without loss of generality, i = 1 since a scalar product yields the same projection. Thus, there are 8 parameters to be determined for this matrix. The coordinate of the 4 vertexes of the projection plane before and after projection was used to calculate the matrix elements as shown in Equation (5.3):

$$M_{ds} = \begin{pmatrix} u_0 & v_0 & 1 & 0 & 0 & 0 & -u_0x_0 & -v_0x_0 \\ u_1 & v_1 & 1 & 0 & 0 & 0 & -u_1x_1 & -v_1x_1 \\ u_2 & v_2 & 1 & 0 & 0 & 0 & -u_2x_2 & -v_2x_2 \\ u_3 & v_3 & 1 & 0 & 0 & 0 & -u_3x_3 & -v_3x_3 \\ 0 & 0 & 0 & u_0 & v_0 & 1 & -u_0y_0 & -v_0y_0 \\ 0 & 0 & 0 & u_1 & v_1 & 1 & -u_1y_1 & -v_1y_1 \\ 0 & 0 & 0 & u_2 & v_2 & 1 & -u_2y_2 & -v_2y_2 \\ 0 & 0 & 0 & u_3 & v_3 & 1 & -u_3y_3 & -v_3y_3 \end{pmatrix} \begin{pmatrix} a \\ b \\ c \\ d \\ e \\ f \\ g \\ h \end{pmatrix} = \begin{pmatrix} x_0 \\ x_1 \\ x_2 \\ x_3 \\ y_0 \\ y_1 \\ y_2 \\ y_3 \end{pmatrix} \tag{5.3}$$

where u_k and v_k are the coordinate of the kth vertex on the source plane, and x_k and y_k are the coordinate of the kth vertex on the destination plane.

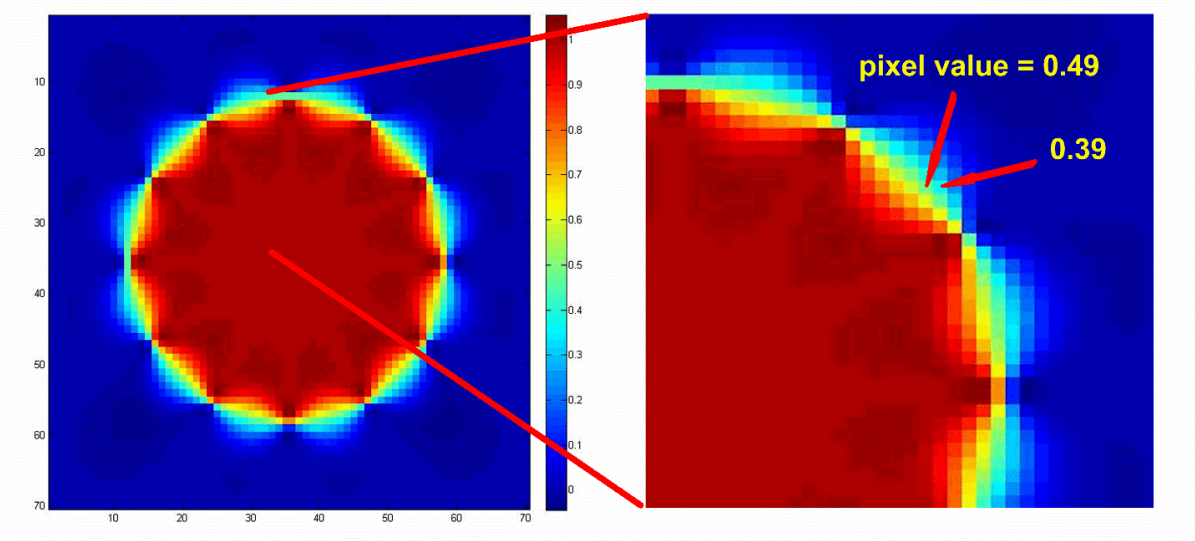

Fig. 5.4. Threshold value for the 3D binary masks. A C-plane denoting a horizontal slice of the reconstructed 3D mask using SOUPR is shown. Pixel values decrease from 1 around the center to 0 towards the background. A threshold value of 0.45 was selected between the two values shown in the expanded figure. A threshold value outside this range would result in a distorted surface.

The final interpolated 3D grid resolution was similar to that used for SOUPR, which was around 0.25×0.25×0.25 mm.

5.2.4 Volume, SNRe and CNRe calculation

Inclusion volume comparisons were conducted using the 3D binary masks. Nevertheless, due to the interpolative nature of the 3D reconstruction algorithms, these 3D binary masks did not preserve a sharp boundary. There was a transition gradient from the inclusion to background with the value varying from 1 to 0. A threshold value between 0 and 1 was selected to define the

boundary of these binary 3D masks. In this study, a threshold of 0.45 was applied to preserve a smooth and reasonably segmented boundary of the reconstructed volume, as shown in Fig. 5.4. For all the 3D binary masks generated from the 8 displacement tracking kernels, all voxels greater than 0.45 were set to be 1 while the others were set to be 0.

With the boundary defined by the threshold value, the volume of the inclusion was estimated as shown in Equation (5.4):

$$V = N \times \Delta v \tag{5.4}$$

where V is the volume of the inclusion, N is the number of voxels inside the inclusion and Δv is the voxel volume defined by the resolution of the 3D coordinate grid. Spatial resolution of the 2D strain images generated with different displacement tracking kernels were registered with the same B mode image to keep the voxel size estimation robust through those 8 tracking kernels.

In this study, SNRe was defined as in Equation (5.5) [20].

$$SNR_e = \frac{\mu}{\sigma} \tag{5.5}$$

where μ is the mean value within the region of interest (ROI) which is a cubical region defined inside the reconstructed inclusion with a volume of around 0.25 cm^3 (approximately 0.8×0.8×0.4 cm); σ is the standard deviation within the ROI.

The CNRe was used to evaluate lesion detectability on strain images. The CNRe takes into consideration the contrast of the target and background and their contribution to the noise level as defined in Equation (5.6).

$$CNR_e = \frac{|\mu_i - \mu_b|}{\sqrt{\sigma_i^2 + \sigma_b^2}} \tag{5.6}$$

where μ_i is the mean value of the ROI, which is a cubical region defined inside the inclusion, and also used for SNRe calculations; μ_b is the mean value within a similar sized cubical ROI defined in the background. σ_i and σ_b denote the standard deviation of the estimates within the inclusion and background ROI, respectively.

5.2.5 Sensitivity analysis of center bias

A simulated spherical phantom was used to study the volume and shape preservation of the 3D reconstruction when the center of the SOUPR planes do not coincide with the center of the inclusion. The radius of the simulated spherical phantom was 0.6, and the maximum distance the center of SOUPR was shifted was 0.2, which corresponds to 33.3% of the radius. At each shifted SOUPR center, a series of 2D imaging planes was calculated theoretically based on the sphere geometry, using the same 30° rotation angle. The simulation was performed for two distinct conditions; the first where information on the inclusion center or axes was known and the second with an unknown inclusion center. For the first condition with a known target center, each 2D image slice was placed at the corresponding position intersecting the spherical phantom shown in Fig. 5.7(a). Both the volume and Jaccard index of the reconstructed phantom was calculated based on the SOUPR algorithm described in Equation (5.1). The Jaccard index denotes a parameter that is used to measure the similarity between two data sets, which is formulated in Equation (5.7):

$$Jaccard\ \ index = \frac{A \cap B}{A \cup B} \tag{5.7}$$

where *A* denotes the reconstructed 3D volume, while *B* represents the volume of the simulated phantom.

In a similar manner, for the second condition tested, we assumed that the position of target was not available, and SOUPR center was set as the default central axis. Each 2D image slice was aligned with this central axis and the 3D volume was reconstructed with this default coordinate system. The volume and Jaccard index obtained was compared between these two conditions. The simulation was performed using the MatLab software (Mathworks Inc. MA, US).

5.2.6 Feasibility on *ex-vivo* tissue

3D reconstructions using SOUPR and wobbler were also validated on *ex-vivo* bovine liver tissue with an ablated region created using a Neuwave Medical Certus 140 (Madison, WI, USA) system. Fresh bovine liver tissue was obtained from a local slaughter house. The ablated region was created using a general clinical setting using a 55 W power level for 3 min ablation duration and a single antenna. The 2D imaging planes were positioned using the same geometry as that utilized for the TM phantom scans as shown in Fig. 5.2(a) and 5.2(b). 2D strain images were generated with a 2% compression corresponding to the tissue height. The volume of the ablated region was calculated using a 3D binary mask previously described and shown in Equation (5.4).

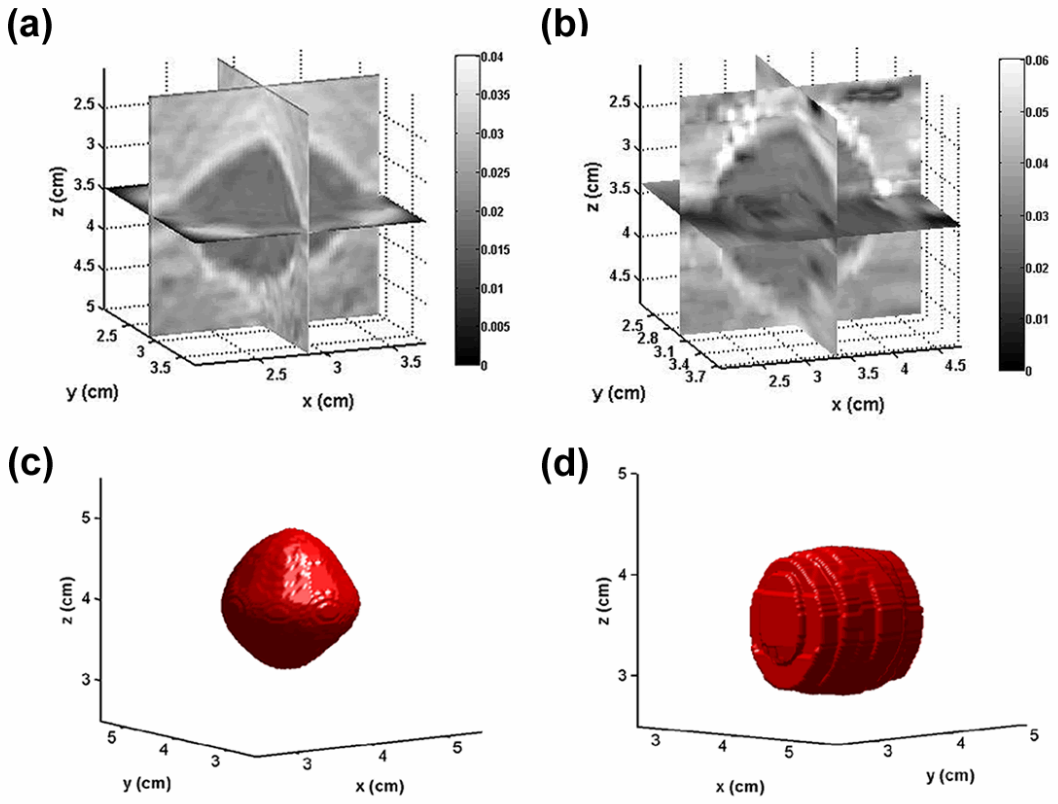

Fig. 5.5. 3D reconstruction of strain images and corresponding segmented regions obtained using the binary mask. 3D strain volume distribution (a) and segmented region (c) for SOUPR. Similarly, the 3D strain image (b) and inclusion segmented (d) using a Wobbler transducer. These images were reconstructed based on 2D strain images generated with a cross-correlation kernel size of 4.8 wavelength × 7 A-lines.

5.3 Results

Due to the data smoothness constraint associated with SOUPR based reconstructions, the noise level within the inclusion and background was lower when compared to the wobbler based reconstructions as shown in Fig. 5.5(a) and 5.5(b). The 3D reconstructed strain volume with

SOUPR was visibly closer to the ellipsoidal shape of the phantom inclusion while the shape reconstructed with the wobbler transducer was more cylindrical as illustrated in Fig. 5.5(c) and 5.5(d).

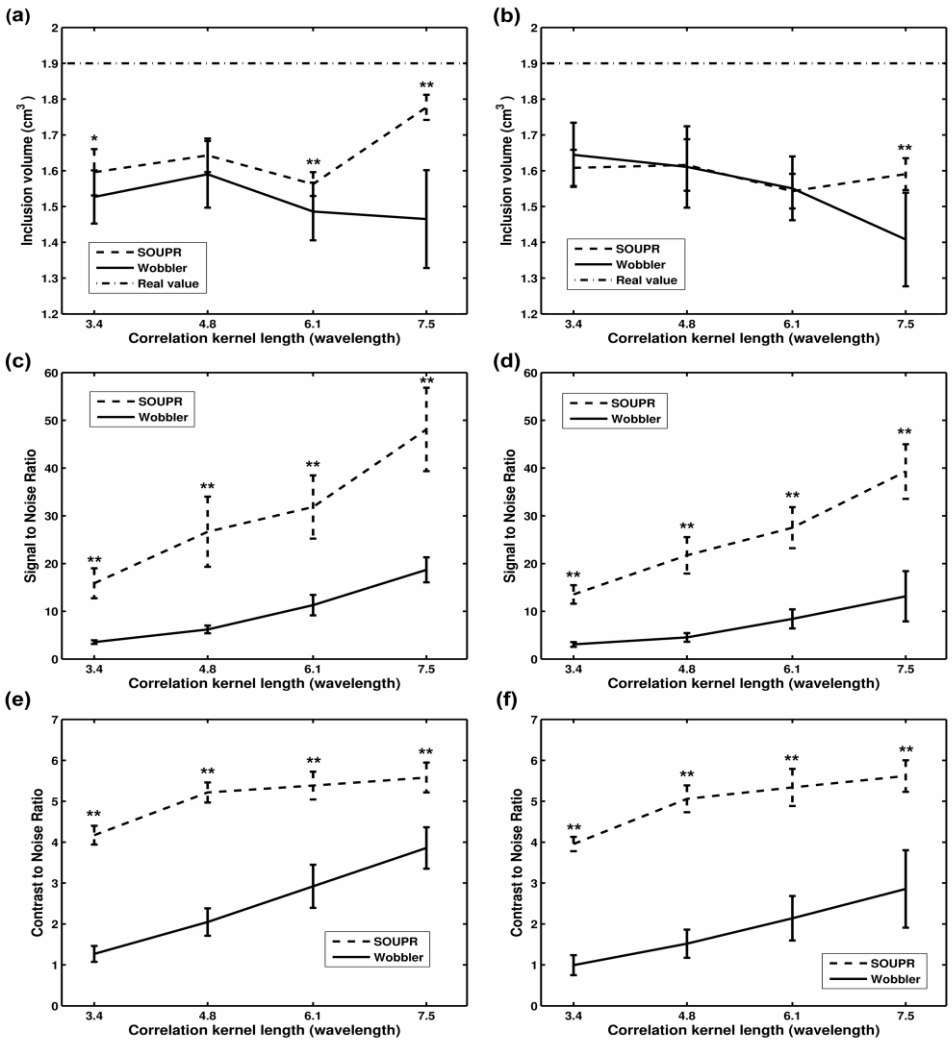

Fig. 5.6. Comparisons of reconstructed inclusion volume, SNRe and CNRe metrics. Figures (a), (c) and (e) are based on the 2D strain images generated with cross-correlation kernels width of 7 A-lines, while Figs. (b), (d) and (f) are based on a cross-correlation kernel width of 3-A lines. The kernel lengths on the horizontal axis were 3.4, 4.8, 6.1 and 7.5 wavelengths. Figures (a) and (b) present a comparison of the inclusion volume estimates between SOUPR and Wobbler. The dotted line on top denotes the actual inclusion volume. Figures (c) and (d) are the SNRe comparisons for the same series of kernel sizes, while Figs. (e) and (f) present the CNRe comparisons. The error bar for each kernel size denotes the standard deviation of 10 independent measurements. The star notation represents the p-value of a single sided t-test for the hypothesis that SOUPR estimates are equal to these obtained using the wobbler transducer. A single star notation denotes that $0.01 < p < 0.05$, while 2 stars denotes $p < 0.01$.

Comparisons of the reconstructed inclusion volume, SNRe and CNRe obtained with a cross-correlation kernel width of 7 A-lines, are shown in Fig. 5.6(a), 5.6(c) and 5.6(e). The average inclusion volume obtained using SOUPR over the 4 kernel lengths was 1.64 cm^3, which was 7.7% larger than the volume of 1.53 cm^3 obtained with the wobbler transducer shown in Fig. 5.6(a). The average SNRe obtained with SOUPR over the 4 kernel lengths was 30.6, which was 208.5% higher than the SNRe value of 9.9 estimated with the wobbler transducer, as shown in Fig. 5.6(c). An improved CNRe with SOUPR was also obtained with a mean value of 5.1, which was 101.6% higher than the mean of 2.5 obtained with the wobbler transducer, as shown in Fig. 5.6(e). The $p < 0.05$ held for all comparisons except $p = 0.06$ for the volume comparison with the kernel length of 4.8 wavelengths as shown in Fig. 5.6(a).

Comparison results using a kernel width of 3 A-lines are shown in Fig. 5.6(b), 5.6(d) and 5.6(f). The average inclusion volume over the 4 kernel lengths was similar for both SOUPR and wobbler approaches, around 1.57 cm^3. However, improved SNRe and CNRe were observed with SOUPR, which was similar to the results with 7 A-lines kernels. The average SNRe with SOUPR was 25.5, which was 250.3% higher than the average value of 7.3 obtained with the wobbler transducer, while the CNRe of SOUPR was 5.0, which was 166.0% higher than the CNRe value of 1.9. The $p < 0.01$ held for all the SNRe and CNRe comparisons.

Comparisons of the reconstructed ellipsoidal inclusion axis lengths are shown in Table I and Table II, which were computed from the 3D reconstructed binary masks as illustrated in Fig. 5.5(c) and 5.5(d). The axes length in Table I was measured from the 3D binary masks reconstructed from 2D strain images generated with 7 A-line cross-correlation kernels as in Fig. 5.5(a), 5.5(c) and 5.5(e). The axis length in Table II was measured from the 3D binary masks based on 3 A-line

kernels as in Fig. 5.5(b), 5.5(d) and 5.5(f). The mold of the inclusion in the phantom used in this study was constructed with a size of 14×14×19 mm (X, Y and Z axis, respectively).

Table 5.1. Inclusion axis estimates with SOUPR and wobbler reconstruction using 7 A-line kernels

	Axis length of the 3D inclusion reconstructed with SOUPR (mm)			**Axis length of the 3D inclusion reconstructed with wobbler (mm)**		
Window length (wavelengths)	**X**	**Y**	**Z**	**X**	**Y**	**Z**
3.4	14.7±0.5	14.6±0.5	16.2±0.9	14.1±0.8	13.5±1.0	13.8±0.8
4.8	14.3±0.6	14.3±0.6	16.9±1.0	14.2±0.3	13.5±1.0	14.2±0.4
6.1	13.4±0.4	13.4±0.4	17.5±1.0	11.3±0.2	13.5±1.0	17.0±0.2
7.5	14.0±0.6	13.8±0.6	18.2±1.1	11.1±0.3	13.5±1.0	16.6±1.0

Table 5.2. Inclusion axis estimates with SOUPR and wobbler reconstruction using 3 A-line kernels

	Axis length of the 3D inclusion reconstructed with SOUPR (mm)			**Axis length of the 3D inclusion reconstructed with wobbler (mm)**		
Window length (wavelengths)	**X**	**Y**	**Z**	**X**	**Y**	**Z**
3.4	14.5±0.4	14.4±0.6	16.2±0.9	16.5±0.6	13.5±1.0	12.3±0.3
4.8	14.1±0.4	14.0±0.5	16.7±0.9	16.4±0.4	13.5±1.0	12.6±0.2
6.1	13.4±0.4	13.4±0.3	17.1±1.0	13.9±0.9	13.5±1.0	15.1±.03
7.5	13.4±0.4	13.3±0.4	17.6±1.1	13.1±1.2	13.5±1.0	13.9±0.9

For the comparisons with kernels of 7 A-lines' width shown in Table I, the mean error between the measured axes length and the dimensions of the inclusion mold with SOUPR was 2.6%, 2.8% and 9.6% for the X, Y and Z axes, respectively. The mean error of the 3 axes using the wobbler method was 10.4%, 3.5% and 19.0%, respectively. The comparison with kernel width

of 3 A-lines is shown in Table II. The mean error with SOUPR for the 3 axes was 3.3%, 3.1% and 11.0%, respectively, while the mean error with the wobbler transducer was 10.7%, 3.5% and 30.2%.

Sensitivity analysis on the misalignment between the SOUPR and inclusion center is shown in Fig. 5.7. Figure 5.7(a), presents a schematic diagram of the misalignment between the SOUPR and target center, with the corresponding C-plane of the inclusion illustrated in Fig. 5.7 (b). When the location of the shift in SOUPR center with respect to the inclusion center is known, the volume measurement of the reconstructed phantom remains stable and corresponds to the zero-shift case indicated by the solid curve shown in Fig. 5.7(c). On the other hand, when the location of the target center is not known and the SOUPR center is considered to be the target center, the volume of the reconstructed phantom decreases slightly with an increase in the shift. For a shift of 33.3% of the radius, the volume measured dropped to 93% of the value at zero-shift indicated as the dotted curve shown in Fig 5.7(c). A similar trend is also observed for the Jaccard index as shown in Fig. 5.7(d). The similarity between the reconstructed phantom using SOUPR and the original simulated phantom remains around 0.9 even as the center of SOUPR is shifted to 33.3%

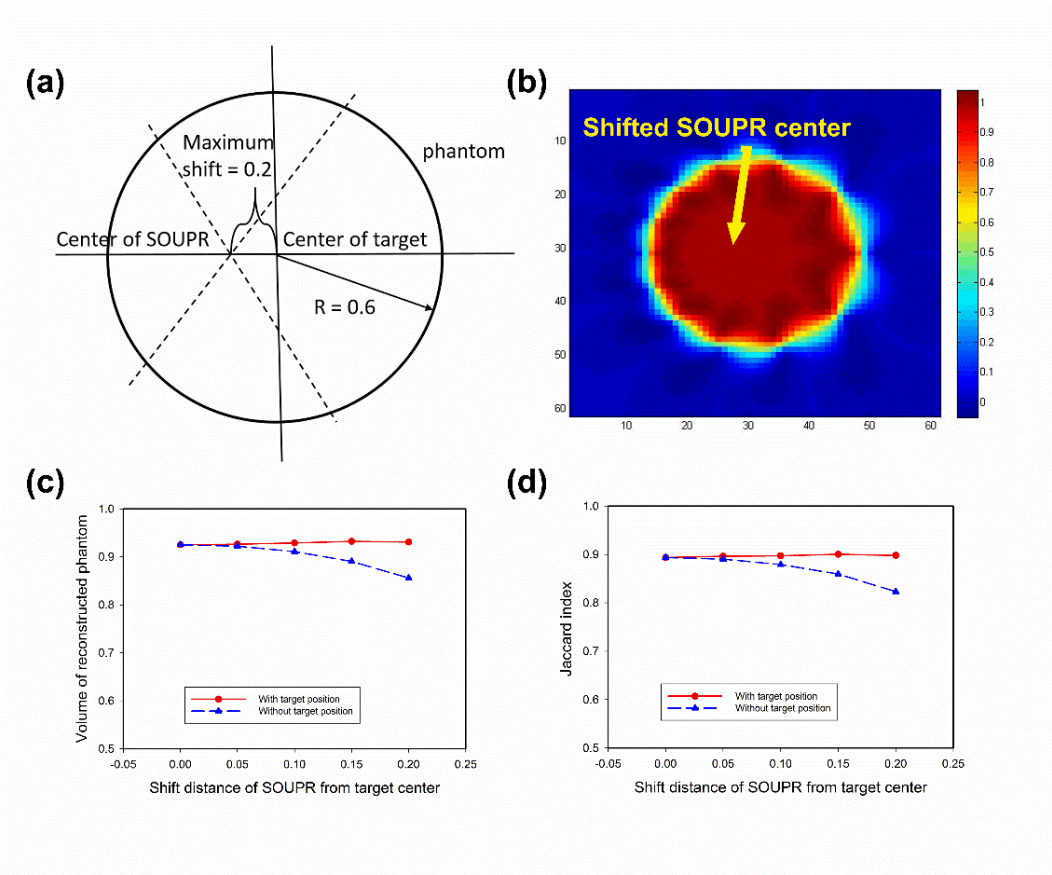

Fig. 5.7. Simulation of the sensitivity of volume estimations for a shift in the SOUPR center with respect to the inclusion center. (a) Schematic diagram of the geometry of the simulated phantom and the shifted SOUPR center. (b) C-plane image of the reconstructed phantom using a shifted SOUPR center, with the known target position. (c) Volume of the reconstructed phantom estimated at different shift. The red (solid) curve was obtained when the target center is known, while the blue curve (dashed) was obtained for the unknown target center case. The center of SOUPR planes was assumed to be the target center when the target position is unknown. (d) The Jaccard index measured at the same shifted distance as (c).

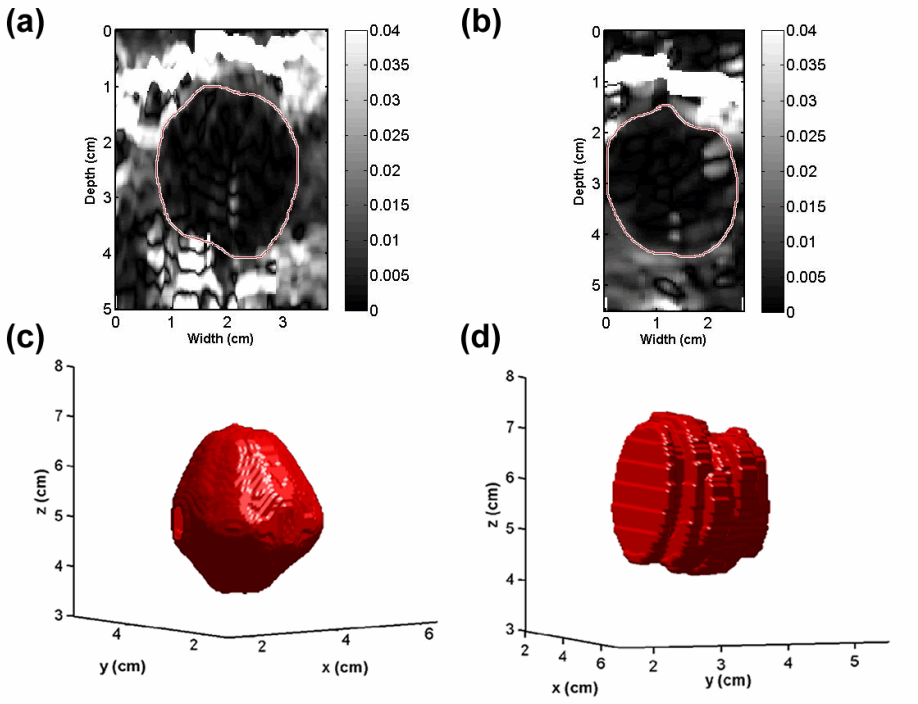

Fig. 5.8. SOUPR and wobbler 3D strain reconstruction of an ablated region created in *ex-vivo* bovine liver tissue. (a) Strain image of the thermal lesion using SOUPR, generated with 6.1 wavelengths × 7 A-lines tracking kernel. (b) Strain image of the thermal lesion for the Wobbler, generated with the same parameters as that for SOUPR. (c) The reconstructed inclusion using SOUPR. (d) The reconstructed inclusion using the wobbler transducer.

of the radius with the known target position. In the absence of target center information, the Jaccard index drops to 92% of the value measured with zero-shift.

A qualitative comparison of the SOUPR and wobbler reconstruction approaches on a microwave ablation procedure performed in *ex-vivo* bovine tissue is shown in Fig. 5.8. 2D strain images are illustrated in Fig. 5.8(a) and 5.8(b), while the corresponding 3D volume reconstructions are shown in Fig. 5.8(c) and 5.8 (d), respectively. The shape of the ablated region reconstructed

with SOUPR was visibly closer to an ellipsoid, which is the most commonly observed shape for thermally coagulated regions, as shown in Fig. 5.8(c) and 5.8(d).

5.4 Discussion and Conclusions

In this study, we compared our previously developed 3D strain reconstruction algorithm, SOUPR, to a conventional method based on RF data acquired using a wobbler transducer, in terms of TM phantom inclusion dimensions, volume, SNRe, and CNRe. Reconstruction results were also compared based on the accuracy of the reconstructed inclusion shape in terms of ellipsoidal axis lengths. The reliability of SOUPR based reconstructions was further validated with a feasibility study using an *ex-vivo* ablation procedure performed on bovine liver tissue.

The dependence of reconstructed inclusion volume on the displacement tracking kernel is illustrated in Fig. 5.6(a) and 5.6(b). For the tracking kernels with a width of 7 A-lines shown in Fig. 5.6(a), SOUPR provides a closer volume estimation to the actual value when compared to wobbler based estimations for almost all kernel lengths (with $p < 0.05$ or $p < 0.01$). When the kernel width is reduced to 3 A-lines, volume estimation with SOUPR displays a similar trend to that obtained using 7 A-lines. The only deviation occurs for volumes estimated with a kernel length of 7.5 wavelengths, which decreases significantly. However, the volume estimation with wobbler transducer provides a closer value to SOUPR with this smaller displacement tracking kernel, as illustrated in Fig. 5.6(b). This comparison indicates that the volume estimation with SOUPR is less sensitive to the size of the displacement tracking kernels than the wobbler and provides overall more stable volume estimation. In addition to the relatively stable estimation at various tracking kernel sizes (for each specific kernel) the standard deviation of the volume estimation with SOUPR

is smaller than that with a wobbler, which is indicated by the length of the error-bar in Fig. 5.6(a) and 5.6(b).

Estimation of inclusion volumes with SOUPR and wobbler were both below the actual value of 1.9 cm^3 as shown in Fig. 5.6(a) and 5.6(b). Underestimation with wobbler transducer might be due to the fact the wobbler transducer will miss the outer boundary of the spherical target which falls between the gaps between slices. The ellipsoidal volume outside the outermost imaging planes was not accounted as shown in Fig. 5.5(d) and Fig. 5.7(b). Visualization and improved volume estimation results can be obtained by using smaller step-and-shoot angles, and consequently a larger number of 2D imaging planes, to reconstruct the 3D volume using the wobbler transducer. In this study we attempted to have similar number of imaging planes for both SOUPR and wobbler based reconstructions. On the other hand, the underestimation of inclusion volume with SOUPR may be caused by the fact that the intersecting imaging plane may not perfectly align with the central axis of the inclusion. The imaging plane passing through the central axis of the inclusion would provide the largest intersection area of the inclusion. The current reconstruction algorithm with SOUPR assumes that every imaging plane would align with the central axis of the inclusion and thus, if the imaging plane failed to pass, a smaller intersection area would be input to SOUPR and an underestimation of the inclusion volume could have been resulted. This situation can be mitigated by using 2D matrix array transducers, where the SOUPR intersecting planes would be better aligned[22]. Another probable reason for the underestimated volume of SOUPR might be caused by the threshold value selected for the binary masks. The boundary of the 3D binary masks decreases from value of 1 to 0 as shown in Fig 5.4. A too large or too small threshold value would result in a distorted volume surface. To keep a smooth surface of the 3D volume, threshold values between 0.37 and 0.47 can be utilized. We used a threshold

value of 0.45 in our study to reduce the volume increase caused by the interpolation as much as possible, while keeping a smooth surface of the 3D volume. This threshold has been validated from the 3D masks shown in Fig 5.4. A robust 3D segmentation method applied directly to the 3D strain volume might be helpful as a further study to replace the 2D thresholded binary masks.

The detectability of the reconstructed inclusion is evaluated in terms of the SNRe and CNRe metrics for SOUPR and wobbler based reconstructions as shown in Fig. 5.6(c)-5.6(f). The SNRe and CNRe of the reconstructed inclusion with SOUPR was higher than that of wobbler with statistical significance ($p < 0.01$). This improvement in the SNRe and CNRe for SOUPR when compared to the wobbler may result from the factor that would contribute to SNRe and CNRe enhancement is the different reconstruction algorithms applied for SOUPR and wobbler 3D reconstruction respectively. The 3D reconstruction for SOUPR is modeled as an optimization problem with an objective function consisting of data consistency and smoothness constraints[15]. The data smoothness constraints utilized, may result in the 3D volume reconstructed with SOUPR having lower data variance when compared to wobbler based data acquisition where the reconstruction is accomplished with a 3D cubical interpolation. The standard deviation of the SNRe metric for each displacement tracking kernel size is larger for SOUPR when compared with wobbler based reconstructions as illustrated in Fig. 5.6(c) and 5.6(d). However, the standard deviation for CNRe estimates shows an inverse relationship as shown in Fig. 5.6(e) and 5.6(f), where it is larger for wobbler than SOUPR based reconstructions.

Besides the quantitative metrics including inclusion volume, SNRe and CNRe, one important goal of 3D strain reconstruction is to visualize the reconstructed volume, in our case the thermally coagulated region in the liver. Thus, a full characterization of the target shape is critical to judge the thermal dose distribution in the ablated region. From Fig. 5.8(c) and 5.8(d), it is shown

that the reconstructed inclusion obtained with SOUPR is more consistent with the ellipsoid shape anticipated while the results with wobbler are more cylindrical which is caused by the quasi-linear interpolation among the 2D imaging planes. Although an angle correction has been applied to the reconstruction, and the fact that the overall translation angle was only 6-7 degree which does not differ significantly from a parallel approximation. In order to quantify the shape preservation, the three axes of the ellipsoidal inclusion were compared between SOUPR and wobbler reconstructions. From Table I and Table II, it is shown that except for the Y axis, the error along the X and Z axis is quite large with the wobbler. In other words, the wobbler reconstruction preserves the Y axis length reasonably well while a large distortion occurs for the other two axes. The comparison was further validated on an *ex-vivo* bovine model with a thermal lesion created by microwave ablation as shown in Fig. 5.8. The volume estimation was similar between SOUPR and wobbler with a small increase of 0.7 cm^3 which was with the same trend as observed on phantom.

One limitation of SOUPR is that it assumes that the rotated imaging planes are along the central axis of the target. For liver ablation monitoring, the microwave antenna can serve as a marker for the central axis due to the homogeneous ablation volume anticipated around the antenna. Under other circumstances that the target position is impractical to measure, from the numerical simulation, a 7% underestimation of the target volume will occur with a 33.3% shift from the target center when the target location is unknown. For most imaging situations due to the local nature of ultrasound scanning, we do not anticipate a significant shift from the center of the SOUPR imaging planes to the inclusion center. Another limitation of SOUPR is that the target shape is assumed to be smooth. If the ablated region is surrounded by large vessels, this assumption might not hold since the large heat sink caused by vessels might cause a large distortion of the inclusion shape.

Thus, the reconstruction of an irregular shaped target would require additional 2D SOUPR imaging planes passing through the irregular region and iterative reconstruction approaches [22], which is a topic for study in the future.

The 3D reconstruction applied on TM phantoms with SOUPR provided superior results when compared to the method based on a wobbler transducer in terms of inclusion volume, SNRe, CNRe and shape preservation. The *ex-vivo* experiment demonstrates the ability to use this approach for thermal ablation monitoring. A statistical comparison of these 3D reconstruction algorithms on *ex-vivo* tissue will be the next step to validate our reconstruction algorithm.

5.5 References

1. Varghese, T., et al., *Ultrasonic imaging of myocardial strain using cardiac elastography.* Ultrason Imaging, 2003. **25**(1): p. 1-16.

2. Konofagou, E.E., J. D'Hooge, and J. Ophir, *Myocardial elastography--a feasibility study in vivo.* Ultrasound Med Biol, 2002. **28**(4): p. 475-82.

3. Bae, U., et al., *Ultrasound thyroid elastography using carotid artery pulsation: preliminary study.* J Ultrasound Med, 2007. **26**(6): p. 797-805.

4. Fahey, B.J., et al., *In vivo guidance and assessment of liver radio-frequency ablation with acoustic radiation force elastography.* Ultrasound Med Biol, 2008. **34**(10): p. 1590-603.

5. Ophir, J., et al., *Elastography: a quantitative method for imaging the elasticity of biological tissues.* Ultrason Imaging, 1991. **13**(2): p. 111-34.

6. Sarvazyan, A.P., et al., *Shear wave elasticity imaging: a new ultrasonic technology of medical diagnostics.* Ultrasound Med Biol, 1998. **24**(9): p. 1419-35.

7. Nightingale, K.R., et al., *On the feasibility of remote palpation using acoustic radiation force.* J Acoust Soc Am, 2001. **110**(1): p. 625-34.

8. Catheline, S., F. Wu, and M. Fink, *A solution to diffraction biases in sonoelasticity: the acoustic impulse technique.* J Acoust Soc Am, 1999. **105**(5): p. 2941-50.

9. Manduca, A., et al., *Magnetic resonance elastography: non-invasive mapping of tissue elasticity.* Med Image Anal, 2001. **5**(4): p. 237-54.

10. Lindop, J.E., et al., *3D elastography using freehand ultrasound.* Ultrasound Med Biol, 2006. **32**(4): p. 529-45.

11. Gee, A., et al., *Processing and visualizing three-dimensional ultrasound data.* Br J Radiol, 2004. **77 Spec No 2**: p. S186-93.

12. Treece, G.M., et al., *Freehand ultrasound elastography with a 3-D probe.* Ultrasound Med Biol, 2008. **34**(3): p. 463-74.

13. Bharat, S., et al., *Three-dimensional electrode displacement elastography using the Siemens C7F2 fourSight four-dimensional ultrasound transducer.* Ultrasound Med Biol, 2008. **34**(8): p. 1307-16.

14. Rivaz, H., et al., *Ultrasound elastography: a dynamic programming approach.* IEEE Trans Med Imaging, 2008. **27**(10): p. 1373-7.

15. Ingle, A. and T. Varghese, *Three-dimensional sheaf of ultrasound planes reconstruction (SOUPR) of ablated volumes.* IEEE Trans Med Imaging, 2014. **33**(8): p. 1677-88.

16. Chen, H. and T. Varghese, *Multilevel hybrid 2D strain imaging algorithm for ultrasound sector/phased arrays.* Med Phys, 2009. **36**(6): p. 2098-106.

17. Chen, L., et al., *A quality-guided displacement tracking algorithm for ultrasonic elasticity imaging.* Med Image Anal, 2009. **13**(2): p. 286-96.

18. Chan, T.F. and L.A. Vese, *Active contours without edges.* IEEE Trans Image Process, 2001. **10**(2): p. 266-77.

19. Faugeras, O., *Three-dimensional computer vision: a geometric approach.* Cambridge, Mass: MIT Press, 1993. **10**: p. 817-844.

20. Varghese, T. and J. Ophir, *A theoretical framework for performance characterization of elastography: the strain filter.* IEEE Trans Ultrason Ferroelectr Freq Control, 1997. **44**(1): p. 164-72.

21. Rose, A., *Vision: Human and Electronic*. 1973: Plenum Press.

22. Varghese, T. and A.N. Ingle, *Method and Apparatus for Rapid Acquisition of Elasticity Data in Three Dimensions*, U.p. Office, Editor 2015, Wisconsin Alumni Research Foundation.

Chapter 6: Image fusion of EDE and CT

6.1 Introduction:

Computed Tomography (CT) is the current gold standard for evaluating MWA procedure success for liver tumors. Specifically, abdominal CT scans are performed before and after the MWA procedures to compare the size of tumor and the ablation region in each axial plane to determine whether the margin of the ablation zone is greater than 0.5 – 1 cm [1-3]. CT has also been utilized for monitoring during the ablation procedure, to ensure if the MWA antenna is placed in the exact location specified during treatment planning. In this chapter, we propose EDE [4-6], as a possible alternative modality to monitor the ablation margin in real time to avoid the prolonged treatment time and ionizing radiation exposure both to clinicians and patients. Since the size of tumor is challenging to determine from ultrasound B-mode images, a comparison between EDE and diagnostic CT is necessary to measure the ablation margin. However, the imaging plane for guidance ultrasound B-mode imaging and thereby EDE, is usually selected to encompass the entire ablation antenna, and this imaging plane is usually between the axial and sagittal planes of the 3D CT scans.

Most current imaging fusion techniques are based on utilizing position sensors [7-9] attached to an ultrasound transducer, with the location then fit to a 3D CT coordinate system. Image registration is then applied to align critical anatomy as markers [10-12]. In this chapter, we introduce image fusion techniques to register the ultrasound imaging plane with the corresponding CT image. An in-house virtual slicing tool is compared to commercial software, OsiriX (Pixmeo SARL, Geneva area, Swiss) for the virtual slicing task.

6.2 Materials and Methods

6.2.1 Geometric model for EDE and CT registration

The geometric model of the imaging planes with ultrasound and CT imaging is shown in Fig. 6.1. Under the assumption of a square patient body with a flat surface as shown in Fig. 6.1 (a), the MWA antenna is inserted into the patient body at an angle to the axial plane. If the surface of patient is assumed to be flat, the ultrasound imaging plane would be always perpendicular to the surface of the patient body. Thus, the ultrasound plane, which we are trying to extract from the 3D CT volume, could be determined by rotating the axial image with the rotated axis perpendicular to the patient surface, to a position that would encompass the entire needle track. The geometry of the rotated imaging plane is shown in Fig. 6.2. The ultrasound imaging plane is defined by the vector of the ablation needle and the rotation axis as shown in Fig. 6.1 (a).

In reality, however, there is a curvature associated with abdominal ultrasound imaging. Usually a curvilinear transducer is used for an enlarged field of view. As a result, the handle of the transducer is not necessarily perpendicular to the surface of the patient body as shown in Fig. 6.1 (b). In this case, the ultrasound imaging plane is defined by the vector of the ablation needle and the tilted vector along the handle of the transducer as shown in Fig. 6.1 (b). In this chapter, we considered two cases as shown in Fig. 6.1 (a) and (b), separately using commercial software OsiriX (Pixmeo SARL, Geneva area, Swiss) and an in-house developed virtual slicing tool.

6.2.2 Image fusion strategy

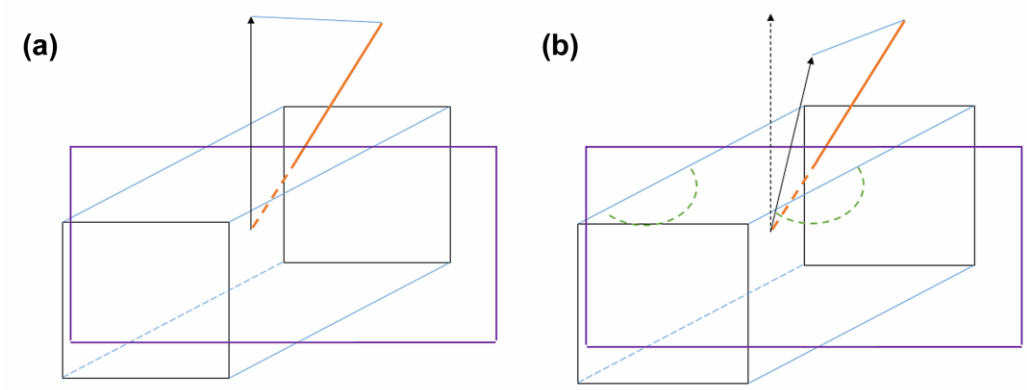

Fig. 6.1. Geometry of image fusion with ultrasound and CT. (a) With the assumption of a flat patient surface, the virtual slice is fixed by the needle vector (orange) and the perpendicular vector (black). (b) With a curvature associated with patient body, the vector for the transducer handle is tilted (black). The resulting virtual slice is defined by this tilted transducer vector and the vector denoting the ablation needle. The norm vector of the virtual slice is given by the cross product of the two vectors.

The image fusion strategy proposed in this chapter is summarized in two steps. The first step is to perform a virtual slicing on the 3D CT volume to extract the corresponding 2D CT image with the same geometrical plane as the ultrasound image. As introduced in section 6.2.1, this corresponding CT slice could be located using the ablation needle as a landmark. With the assumption of a flat patient surface as shown in Fig. 6.1 (a), this corresponding imaging plane is fixed, which is defined by the vector of ablation needle and the perpendicular vector to the patient surface. The norm vector of this imaging plane is defined by Equation 6.1:

$$\vec{N} = \vec{V} \times \vec{I} \qquad (6.1)$$

where $\vec{N}$ is the norm vector of the plane to be extracted from the CT volume, which is defined as the cross product of the vector of ablation needle, $\vec{V}$, and the perpendicular vector to the patient surface, $\vec{I}$.

Considering a curvature for the patient's body with abdominal ultrasound imaging, the handle of the transducer now has more freedom of motion to be tilted as shown in Fig. 6.1 (b). The norm vector of the imaging plane is defined as Equation 6.2:

$$\vec{N} = \vec{V} \times \vec{I'} \quad (6.2)$$

where $\vec{N}$ is the norm vector of the corresponding imaging plane, $\vec{V}$ is the vector of the ablation needle, while $\vec{I'}$ is the tilted vector of the transducer. However, the tilt angle could be reasonably assumed to be small when applied on a patient. Moreover, although the tilt vector of the transducer has two degrees of freedom of rotation: within the axial and sagittal axes of the patient, only the rotation along the sagittal axis is considered because the rotation along the axial axis does not change the imaging plane.

The second step of image fusion is the registration of the ultrasound image with the corresponding 2D CT image extracted with the virtual slicing method. In this chapter, an affine transform based image registration is applied with characteristic markers being the ablation needle and liver surface.

6.2.3 Virtual slicing using OsiriX

We compare an in-house developed virtual slicing method with commercial software OsiriX (Pixmeo SARL, Geneva area, Swiss). The OsiriX software can rotate axial, sagittal, and

coronal imaging planes with the corresponding axis. Thus, with the assumption of a flat patient surface, the virtual slice can be extracted with OsiriX by rotating the axial plane to encompass the entire needle as shown in Fig. 6.2.

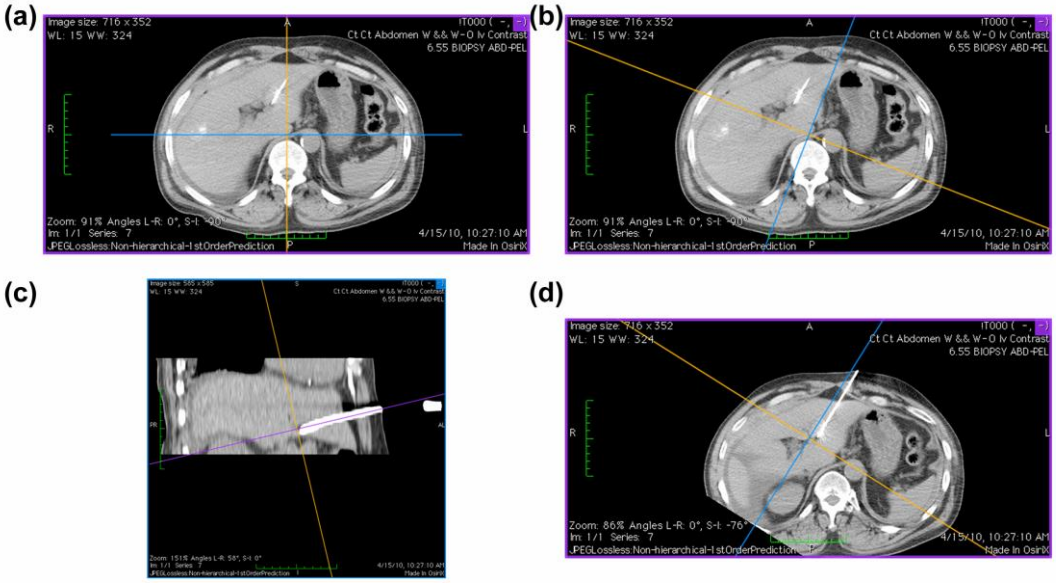

Fig. 6.2. Virtual slicing using OsiriX. (a) Original axial image with part of the intersection with the ablation needle. (b) Rotated coronal plane geometry as indicated by the blue line, which is the position of the original coronal plane. (c) Rotated coronal plane with the entire needle. The purple line indicates the axial plane rotated along the needle. (d) The virtual slice of the rotated axial plane as indicated by the purple line in (c). This virtual slice includes the entire needle, which is the land mark used to register with the 2D ultrasound imaging plane.

The protocol utilized using OsiriX is as follows:

(1) Turn on the '3D MPR' function to enter the axial, coronal, and sagittal imaging mode. Select an axial CT image that includes a section of the intersection of the ablation needle as shown

in Fig. 6.2 (a). The position of these planes can be adjusted using the color lines, which indicate where the planes are located from other angular views.

(2) Rotate the coronal plane as indicated by the blue line in the axial view. Align the blue line with the part of the intersection with the ablation needle. Then translate the coronal plane to overlap with the ablation needle as shown in Fig. 6.2 (b).

(3) In the corresponding coronal plane, the entire ablation needle should be observed. Rotate the axial plane as indicated by the purple line in this coronal view to overlap with the needle as shown in Fig. 6.2 (c).

(4) The axial view should then depict the result shown in Fig. 6.2 (d). This is a rotated axial imaging plane between the axial and sagittal planes, encompassing the entire needle. With the assumption of a flat patient surface, this is the unique imaging plane which overlaps with the 2D ultrasound scan plane.

(5) Record the relative rotation of these planes, and apply the same rotations to the post ablation CT scans to extract the virtual slice, which is the same imaging plane as that used for EDE. The final results are shown in Fig. 6.3.

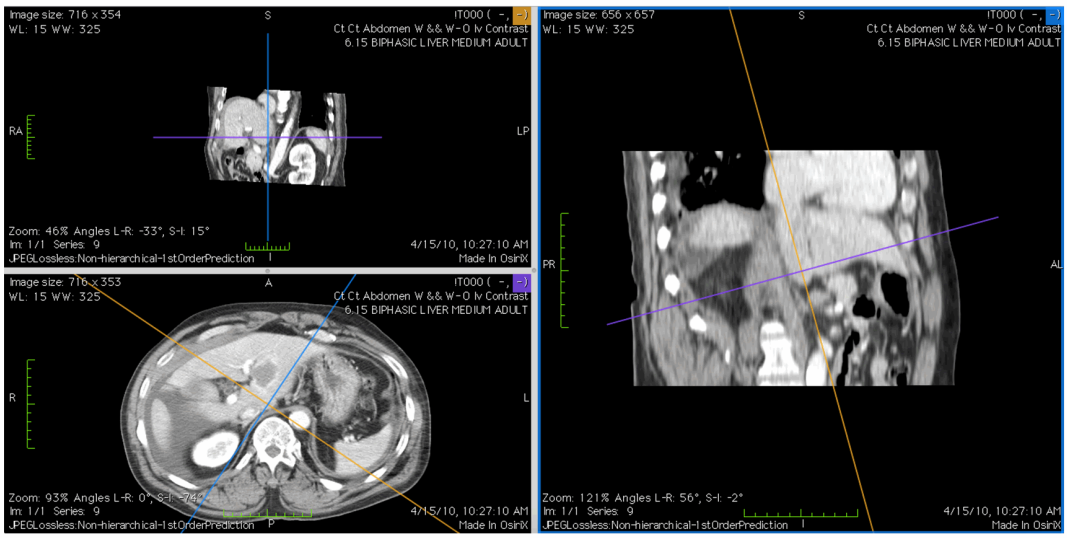

Fig. 6.3. Post ablation CT image extracted with the same rotation recorded from the pre-ablation registration results with ablation needle inserted, as shown in Fig. 6.2

6.2.4 Virtual slicing using an in-house developed tool

The image rotation axes obtained with OsiriX is perpendicular to the surface of the patient. Thus, the tilt of the transducer with respect to the patient abdominal surface is not realized using OsiriX. We developed an in-house virtual slicing tool using Matlab to provide the handle of the transducer more freedom enabling it to be positioned as shown in Fig. 6.1 (b). The work flow of our method is to first extract the ablation needle with thresholding to determine the line vector of the needle within the 3D CT image coordinate system. The threshold Hounsfield value selected in this chapter is 2000 in the DICOM images. At the tip of the needle, the norm vector of the virtual slice is determined using Equation 6.2. Since the tilt vector for the transducer is arbitrarily defined, any position of the ultrasound transducer could be modeled. As discussed in section 6.2.2, only a

small rotation angle with the sagittal axis is considered. With the point of needle tip and the norm vector, virtual slicing is performed through the 3D CT volume.

The virtual slicing tool is tested with a digital phantom and a patient data collected for our research under the IRB protocol described previously. The digital phantom is a spherical phantom, which is sliced along the central plane as shown in Fig. 6.4. A nearest neighbor and bilinear interpolation algorithm are compared for the virtual slicing tool using the digital phantom. The CT volume of the patient data is shown in Fig. 6.5 with different gray level values.

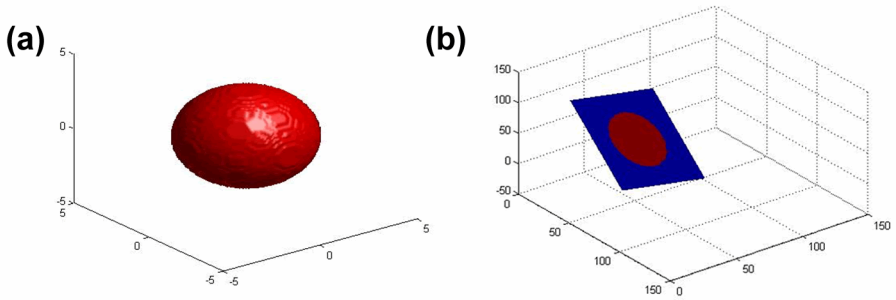

Fig. 6.4. The digital phantom used to test our in-house virtual slicing tool. (a) The 3D digital phantom. (b) The position of the virtual slice in the coordinate system. This virtual plane is positioned through the center of the spherical phantom.

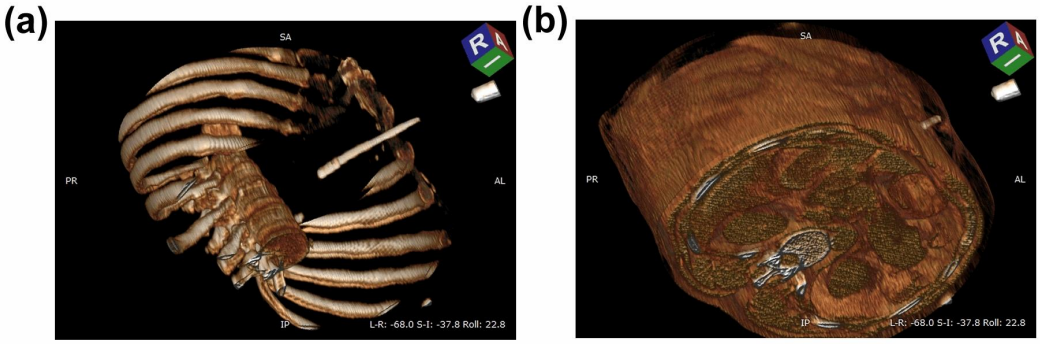

Fig. 6.5. 3D CT volume for a patient recruited to our research study. (a) The CT volume displayed with a high window value, only showing high-density material. (b) The same data set from an identical viewing angle with (a) with a low threshold value, showing soft tissues.

6.3 Results

6.3.1 Virtual slicing results using OsiriX

The post ablation virtual slice from a 3D CT scan is compared to the corresponding ARFI and EDE images, as shown in Fig. 6.6. A qualitative comparison shows that the ablated targets present with a similar shape as that depicted with EDE.

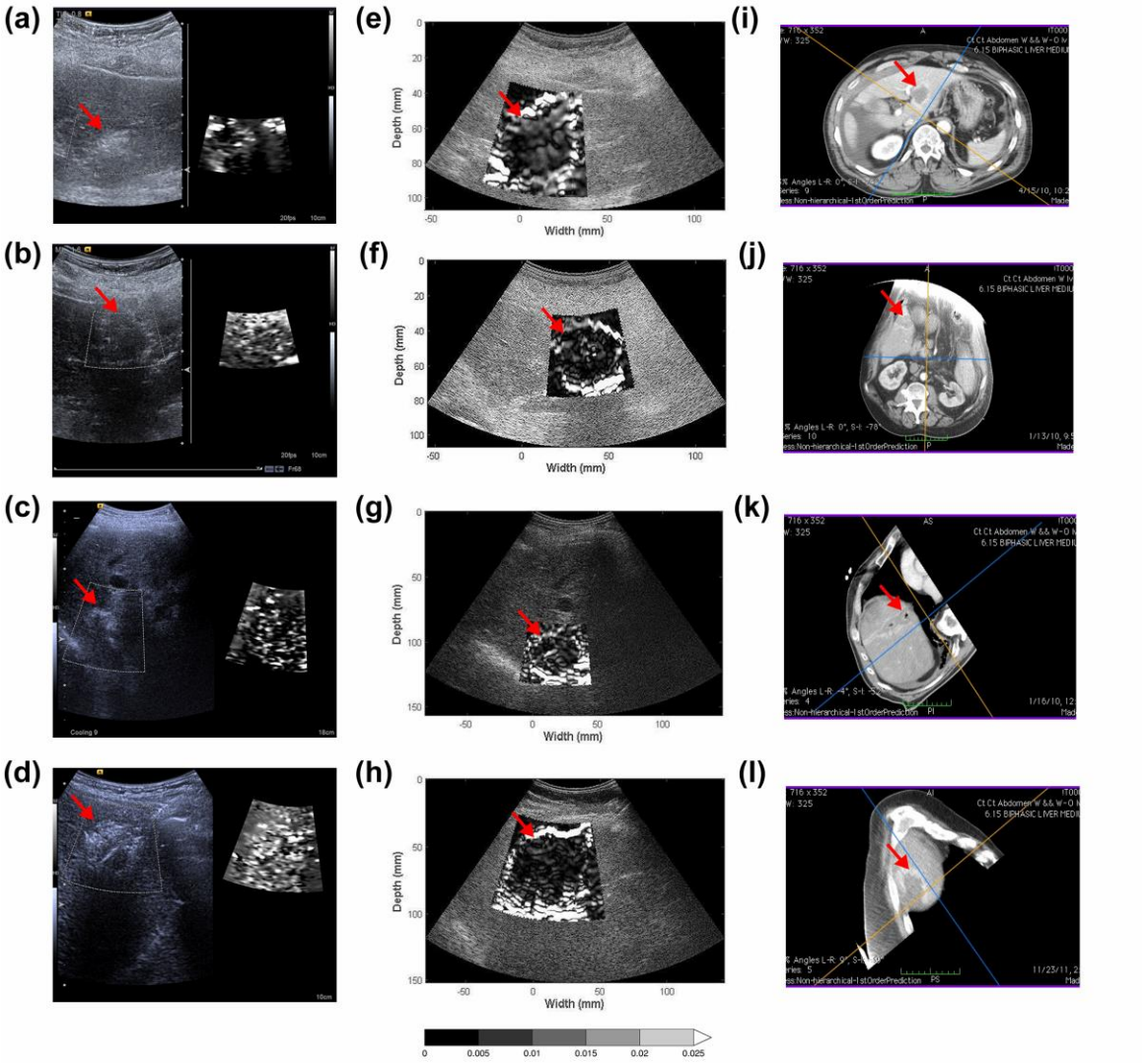

Fig. 6.6. Comparison of the virtual slices generated with OsiriX. The first column (a)-(d) is the ultrasound B-mode and ARFI images for different patients. The second column (e)-(h) is the EDE images for the same patients. The third column (i)-(l) is the 2D virtual slice extracted from the 3D CT volume using OsiriX. The ablation targets are marked with red arrows.

6.3.2 Digital phantoms virtual slicing results using the in-house developed tool

A nearest neighbor and bi-linear interpolation algorithms are compared using the digital phantom to test the virtual slicing results. As shown in Fig. 6.7 (a), the virtual slice with the nearest neighbor interpolation shows a fuzzy boundary. On the other hand, the bilinear interpolation results in a smoother boundary with values interpolated between the binary values. To maintain a smooth boundary, the bilinear interpolation algorithm is used in this chapter.

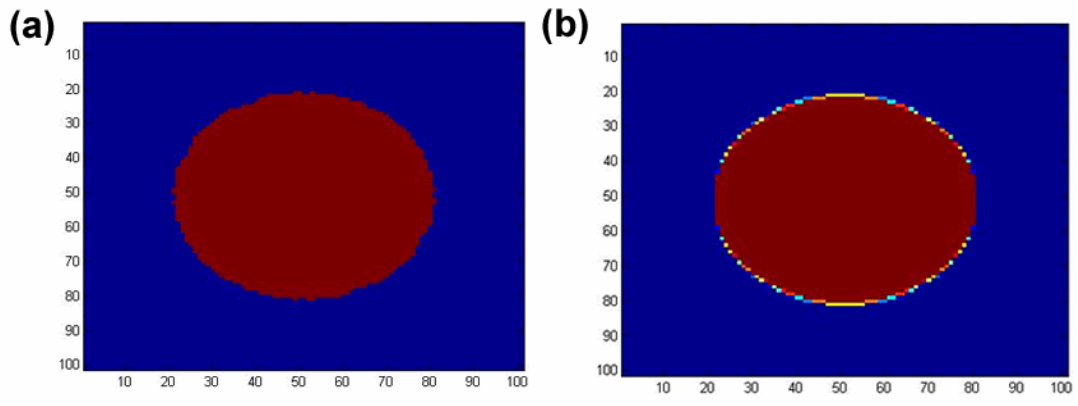

Fig. 6.7. The virtual slice of the spherical digital phantom using the in-house virtual slicing tool. (a) The virtual slice generated using a nearest neighbor interpolation algorithm. (b) The virtual slice obtained with a bilinear interpolation method. Both images show correct diameters of the spherical inclusion while the boundaries have different characteristics.

6.3.3 Needle extraction with thresholding

The ablation needle is extracted using a threshold to segment it from the 3D CT image data set. A binary mask of the thresholded needle is shown in Fig. 6.8 (a). The positions of the ablation needle are plotted in Fig. 6.8 (b). Thus, the vector of the ablation needle is calculated with the plot.

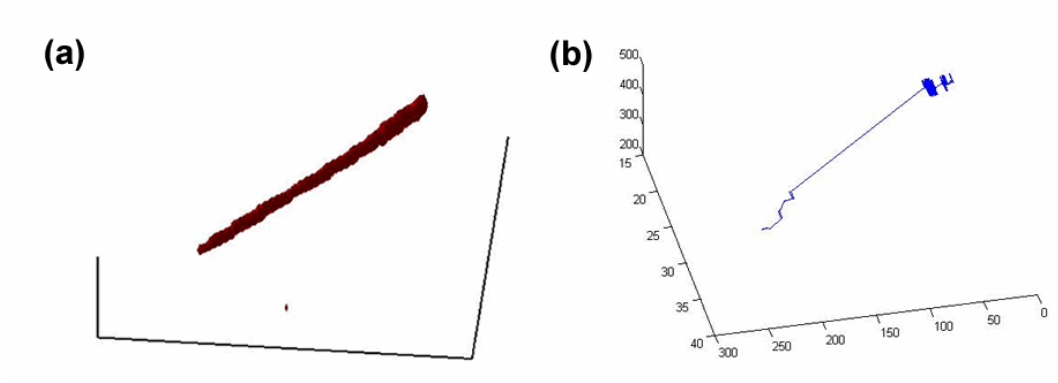

Fig. 6.8. Ablation needle extracted using thresholding. (a) A binary mask of the ablation needle (b) Plot of the positions of the needle in the 3D CT coordinate system. The threshold Hounsfield value used in this chapter is 2000 for the needle.

6.3.4 Virtual slice extracted with the in-house tool

Based on the needle tip and the ablation needle vector, the virtual slice is defined from Equation 6.2. The virtual slice of the pre- and post- ablation CT scans for the patient from Fig. 6.5 is shown in Fig. 6.9. The number of imaging planes for the post-ablation scan is larger than the pre-ablation scan. Thus, the field of view in Fig. 6.9 (b) is larger than Fig. 6.9 (a).

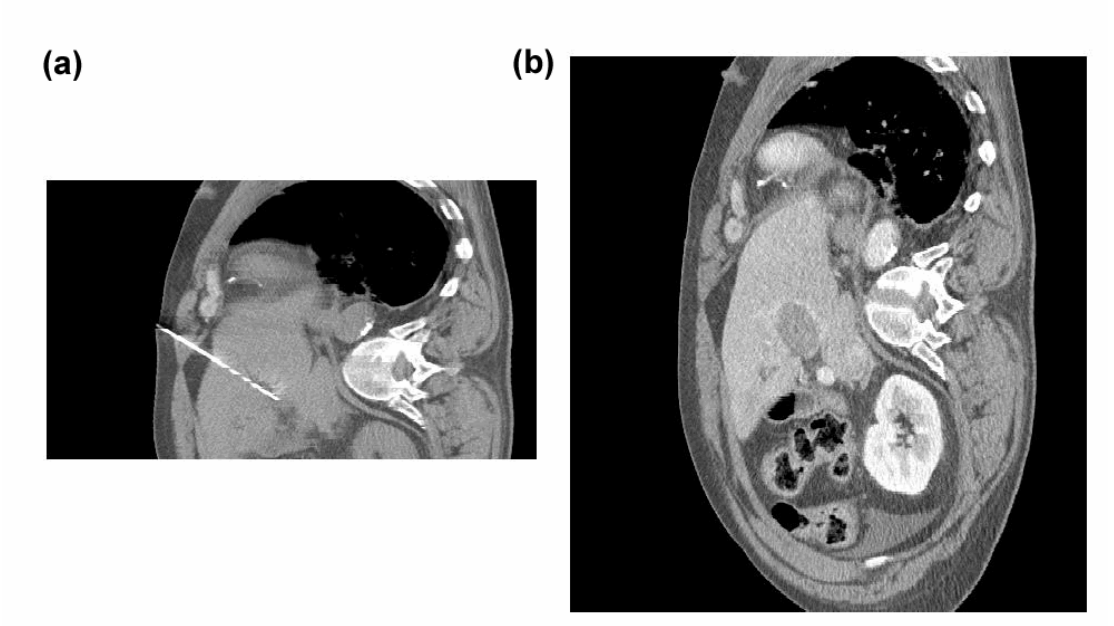

Fig. 6.9. The virtual slice generated with our in-house virtual slicing tool. (a) The virtual slice of the pre-ablation CT scan. The entire needle can be observed. (b) The post-ablation CT scan with the same geometrical transform as that used in (a). The enlarged field of view in (b) is obtained due to the increased scanning range for the post-ablation CT.

6.3.5 Image registration using affine transform

Using the characteristic markers of the ablation needle and liver surface, the registered ultrasound and CT virtual slice obtained is shown in Fig. 6.10.

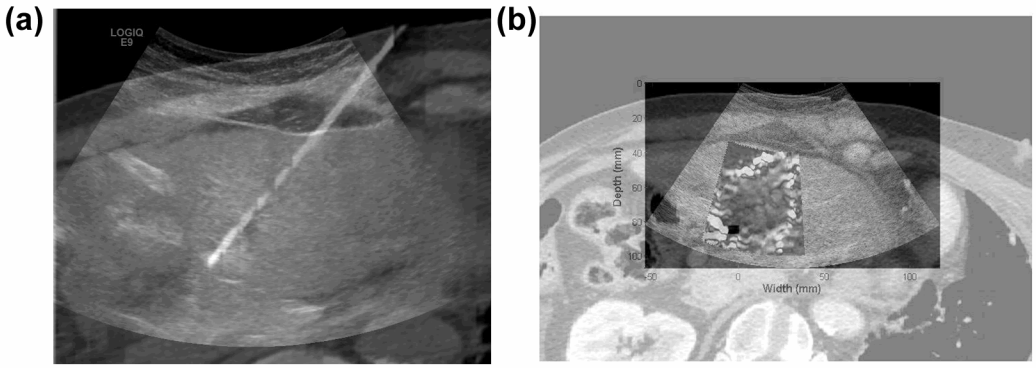

Fig. 6.10. Registered ultrasound and CT virtual slice extracted using the in-house virtual slicing tool. The liver surface and ablation needle is used as the landmark for registration. (a) Image fusion of pre-ablation ultrasound and CT. (b) Image fusion of post-ablation EDE and CT using the same image transform defined in (a).

6.4 Discussion and Conclusions

In this chapter, we performed image fusion of ultrasound and CT images. Commercial software is compared with our in-house developed virtual slicing tool. With the digital phantom and patient data, the feasibility of image fusion is justified in this study.

The most challenging aspect with our in-house virtual slicing tool is the accuracy of needle tracking and segmentation. A simple thresholding process is applied in this study. However, as shown in Fig. 6.8, noise artifacts are unavoidable when using a single threshold. Since the location of the virtual slice is determined by the vector determined by the ablation needle, the final result is very sensitive to the accuracy of the needle segmentation. A more advanced needle tracking algorithm will be a future direction of this research.

With our in-house virtual slicing tool, the position of the ultrasound transducer can be arbitrarily defined. A metric to evaluate the accuracy of the final registration result will be necessary to compare the registration result with commercial software, OsiriX. The advantage of providing more freedom of the transducer will be determined by a quantitative comparison with the condition of a flat patient surface utilized with the commercial software.

In addition to spatial registration, temporal registration is also important and has to be studied. As shown in Fig. 6.9, arteries and veins in the pre and post ablation CT scans are at different stages in their cardiac and respiratory cycles. The effect of physiological motion on the registration result will be studied in the future.

6.5 References

1. Lencioni, R. and L. Crocetti, *Local-regional treatment of hepatocellular carcinoma.* Radiology, 2012. **262**(1): p. 43-58.
2. Lencioni, R. and L. Crocetti, *Radiofrequency ablation of liver cancer.* Tech Vasc Interv Radiol, 2007. **10**(1): p. 38-46.
3. Ziemlewicz, T.J., et al., *Percutaneous microwave ablation of hepatocellular carcinoma with a gas-cooled system: initial clinical results with 107 tumors.* J Vasc Interv Radiol, 2015. **26**(1): p. 62-8.
4. Bharat, S., et al., *Radio-frequency ablation electrode displacement elastography: a phantom study.* Med Phys, 2008. **35**(6): p. 2432-42.
5. Rubert, N., et al., *Electrode displacement strain imaging of thermally-ablated liver tissue in an in vivo animal model.* Med Phys, 2010. **37**(3): p. 1075-82.
6. Yang, W., et al., *Post-procedure Evaluation of Microwave Ablations of Hepatocellular Carcinomas Using Electrode Displacement Elastography.* Ultrasound in Medicine & Biology, 2016.
7. Huang, X., et al., *Dynamic 2D ultrasound and 3D CT image registration of the beating heart.* IEEE transactions on medical imaging, 2009. **28**(8): p. 1179-1189.

8. Kaspersen, J., et al., *Three-dimensional ultrasound-based navigation combined with preoperative CT during abdominal interventions: a feasibility study.* Cardiovascular and interventional radiology, 2003. **26**(4): p. 347-356.

9. Hakime, A., et al., *Clinical evaluation of spatial accuracy of a fusion imaging technique combining previously acquired computed tomography and real-time ultrasound for imaging of liver metastases.* Cardiovascular and interventional radiology, 2011. **34**(2): p. 338-344.

10. Kim, A.Y., et al., *Automatic Registration between Real-Time Ultrasonography and Pre-Procedural Magnetic Resonance Images: A Prospective Comparison between Two Registration Methods by Liver Surface and Vessel and by Liver Surface Only.* Ultrasound in medicine & biology, 2016. **42**(7): p. 1627-1636.

11. Lee, D., et al., *Non-rigid registration between 3D ultrasound and CT images of the liver based on intensity and gradient information.* Physics in medicine and biology, 2010. **56**(1): p. 117.

12. Wein, W., et al., *Automatic CT-ultrasound registration for diagnostic imaging and image-guided intervention.* Medical image analysis, 2008. **12**(5): p. 577-585.

Chapter 7: Contributions and Future Direction

7.1 Summary

Electrode displacement elastography (EDE) is potentially an alternative non-ionizing imaging modality for monitoring microwave ablation (MWA) procedures for liver tumors. With the local displacement induced by the ablation needle, EDE combines the advantage of adequate deformation amplitude with the processing used for conventional quasi-static ultrasound elastography [1]. The independence from external compression apparatus with conventional quasi-static ultrasound elastography [1], provides significant ease of use for clinical studies. In addition, the adequate deformation obtained with EDE provides stiffness images with a significantly higher signal to noise ratio (SNR) and contrast to noise ratio (CNR) when compared to acoustic radiation force impulse imaging (ARFI) based elastography [2]. The clinical application with EDE has been demonstrated with the patient study. For metastatic tumors, the liver tissue is usually normal, with a relatively high modulus contrast between the tumor and background liver tissue [3]. Promising delineation results were obtained from the patients with metastatic tumors. For hepatocellular carcinoma (HCC), liver fibrosis often occurs concomitantly in the liver. The modulus contrast between the tumor and background tissue is relatively lower for HCC patients [3], which is more challenging for pre-ablation elastography to delineate the HCC tumor from surrounding tissue. On the other hand, after the ablation of the HCC, the ablated region is stiffer than the cirrhotic or fibrous background liver which enables better delineation of the ablated region. The stiffness contrast however is not as large as that obtained for metastatic tumors. With our study with 44

patients with HCC, over 90% of successful rate was observed using EDE, as discussed in chapter 3.

In chapter 4, a comparison of EDE and ARFI was performed on tissue mimicking (TM) phantoms and patients with HCC and metastatic tumors. The dimensions of the inclusion embedded in the TM phantom delineated on B-mode, ARFI, and EDE images were within an 8% difference, while the image contrast and CNR were significantly higher in EDE images when compared to those in ARFI images. For the clinical study, the delineation rate of the ablation zone performed by two observers was significantly higher with EDE when compared to ARFI. The difference of EDE and ARFI is significantly reproduced between the two observers and the results for the same modality between the observers are caused by subjective judgement. Less tumor imaging depth dependence with EDE was observed for both TM phantom and clinical studies.

Three-dimensional reconstruction from discrete two-dimensional imaging slices was discussed in chapter 5. Our previously proposed three-dimensional reconstruction method, SOUPR [4], was applied on TM phantoms to compare with a conventional wobbler transducer. For 10 independent measurements, the dimension and volume of the inclusion obtained using SOUPR was closer to the ideal volume of the inclusion. Moreover, a more realistic shape close to an ellipsoid was obtained using SOUPR. Similar results were realized on ablations performed in *ex-vivo* tissue. With the constraint of smoothness in the objective function, image noise was suppressed with SOUPR when compared to the linear interpolation used with wobbler transducer.

In chapter 6, we developed an in-house virtual slicing tool to register EDE images with corresponding CT slices. The virtual slicing tool was based on the vector of the ablation needle and transducer. Since the vector of transducer can be defined arbitrarily, more degrees of freedom

in the position of the virtual slice can be achieved than using commercial software, OsiriX. Image registration was applied based on three characteristic points using the pre-ablation ultrasound B-mode and CT images. The same transform was transferred to the post ablation EDE and CT images for registration.

7.2 Contributions

The contributions of this dissertation are summarized as follows:

A pilot clinical study was performed using EDE for monitoring MWA procedures. We demonstrated that the monitoring results are significantly better than that obtained with conventional B-mode imaging.

We are the first group to compare EDE with ARFI on TM phantoms and \a clinical study to the best of our knowledge. The literature has very limited results reported on the use of ARFI for monitoring thermal ablation procedures in the liver. We discuss the underlying principles and imaging dependence especially with depth for both modalities.

A step and shoot algorithm and software was developed using the SDK for the Ultrasonix system to control a wobbler transducer for elastographic imaging. A variety of parameters can be controlled through the graphical user interface.

Our previously proposed three-dimensional reconstruction algorithm, SOUPR, was tested on TM phantoms and *ex-vivo* ablations. The dimension, volume, SNR, and CNR of SOUPR were superior to those of wobbler transducer.

Use of an in-house virtual slicing tool was introduced in this dissertation. Based on the vectors of ablation needle and transducer, more degrees of freedom of the virtual slice can be obtained when compared to commercial software, OsiriX.

7.3 Future direction

The future direction of the studies reported in this dissertation could be categorized into the following areas. The processing algorithm for EDE is intensive to generate a single frame pair from a continuous loop of ultrasound raw data. Optimization and development using a more efficient processing language would be necessary to be performed in real-time. Currently the pre and post compression frames are selected based on the experience of operator. A selection algorithm would be useful to generate the strain image automatically, which is also necessary for real-time application. Strain noise is another limiting factor with EDE performed in this dissertation. Due to the gradient operation utilized for strain imaging, image noise is unavoidable, although the boundary of ablation zone could be delineated effectively even in the presence of these noise artifacts. A noise suppression algorithm would be beneficial to improve the image quality with EDE.

For the three-dimensional reconstruction study in this dissertation, the strain images of the TM phantom were generated using external uniform compression. Application of SOUPR using EDE would be interesting to visualize the 3D ablation volume. Determination of the rotational center would be a challenging aspect with EDE, and a position sensor would be useful based on the shift analysis discussed in chapter 5.

For the virtual slicing tool discussed in chapter 6, the needle tracking algorithm is crucial to match the ultrasound and CT imaging slice. The current threshold method is based on similar

pixel values for ablation needle and bone. The resulting vector for ablation needle might be biased and positioned inaccurately. An improved needle tracking algorithm would be useful to enhance the accuracy of the virtual slice. The image registration method used in this chapter is based on an affine transform. A projective transform might be useful to match the ultrasound and CT images since the field of view with ultrasound is in sector shape. Moreover, image registration was performed using three similar characteristic points in the ultrasound and CT images. A physical coordinate system based registration might improve the precision of the image registration.

7.4 References

1. Ophir, J., et al., *Elastography: a quantitative method for imaging the elasticity of biological tissues.* Ultrason Imaging, 1991. **13**(2): p. 111-34.

2. Nightingale, K.R., et al., *On the feasibility of remote palpation using acoustic radiation force.* J Acoust Soc Am, 2001. **110**(1): p. 625-34.

3. DeWall, R.J., et al., *Characterizing the compression-dependent viscoelastic properties of human hepatic pathologies using dynamic compression testing.* Physics in medicine and biology, 2012. **57**(8): p. 2273.

4. Ingle, A. and T. Varghese, *Three-dimensional sheaf of ultrasound planes reconstruction (SOUPR) of ablated volumes.* IEEE transactions on medical imaging, 2014. **33**(8): p. 1677-1688.